UNIVERSITÀ
degli STUDI
di CATANIA

Dipartimento
di Fisica
e Astronomia
"Ettore Majorana"

PHD PROGRAMME IN PHYSICS

NOEMI PINO

CHARACTERIZATION OF ELECTROLUMINESCENCE SIGNALS FROM NUCLEAR RECOIL EVENTS IN THE DUAL-PHASE ARGON TIME PROJECTION CHAMBER OF THE REED EXPERIMENT WITH CONVOLUTIONAL AUTOENCODERS

PHD THESIS

SUPERVISORS:
DR. L. PANDOLA
PROF. SSA S. M. R. PUGLIA

ACADEMIC YEAR 2023/2024

Contents

List of Figures

List of Tables

To my sisters, Sara and Rebecca.
Facing adulthood isn't easy, but we'll always find strength in one another.

Introduction

The nature of dark matter, which constitutes 26% of the mass-energy content of the Universe, remains one of the most profound open questions in astroparticle physics. Unraveling the characteristics of this elusive, non-luminous matter is a primary focus of ongoing research. Among the proposed dark matter candidates, the Weakly Interacting Massive Particle (WIMP) stands as the most promising since it offers an explanation for the current abundance of dark matter as a thermal relic from the Big Bang. The Global Argon Dark Matter Collaboration (GADMC) is dedicated to directly detecting WIMP interactions through DarkSide-20k, a multi-ton dual-phase argon Time Projection Chamber (LAr TPC) currently under construction at INFN, Laboratori Nazionali del Gran Sasso. This LAr TPC will be capable of detecting WIMP-nucleon scattering events by capturing both the prompt scintillation light and the ionization charge, the latter detected via a delayed electroluminescence signal proportional to the primary ionized electrons.

While WIMPs with masses on the order of hundreds of GeV/c^2 are widely expected, recent interest has shifted towards lighter WIMPs, with masses as low as 1 GeV/c^2. The properties of argon, combined with the properties of LAr TPCs, make this technology the most promising for probing these low-mass dark matter candidates. However, this search comes with significant challenges, particularly since the energy deposited by WIMP interactions is only a few keV. This low energy makes detecting scintillation signals particularly difficult, necessitating reliance on ionization signals, a phenomenon that still requires further exploration. Data collected with DarkSide-50, the predecessor of DarkSide-20k,

have allowed the development of a model for the ionization response in argon. Still, this model needs to be calibrated at recoil energies below 5 keV, a region not described in the literature and where ionization quenching fluctuations become increasingly significant.

The Recoil Directionality (ReD) experiment, which has dedicated a special measurement campaign to populating this region at low recoil energies, will make a decisive contribution to the in-depth study of this phenomenon. ReD consists of a miniaturized TPC irradiated with neutrons from a fission source in a two-body kinematics approach.

Throughout my Ph.D., I have been deeply involved in the ReD project, from its commissioning and data acquisition to its analysis. My primary contribution has been the development of a technique to classify electroluminescence signals using artificial intelligence algorithms. Given the need to detect even the smallest nuclear recoil events and their corresponding electroluminescence signals, this task focused on exploring alternative analysis methods through machine learning. The novelty of the proposed approach lies in leveraging machine learning algorithms' strength in recognizing patterns within data and extracting key information to make predictions. Neural networks are particularly useful for analyzing large experimental datasets, where the detailed theoretical model may be unknown or for identifying anomalies or events of interest. One major advantage of this method is its reliance on real data rather than simulations. Specifically, I was responsible for developing a convolutional autoencoder (CAE) to study the traces recorded by the signal readout system consisting of silicon photomultipliers operated at cryogenic temperatures. From the information extracted by the algorithm, I developed a CAE-based tagging method to label signals of interest with respect to the noise-only traces.

The structure of this thesis is as follows: Chapter 1 provides an overview of dark matter, from the earliest evidence of its existence to the current technologies used in the direct detection of WIMPs and other candidates; Chapter 2 focuses on argon and the dual-phase TPC technology employed in the GADMC program; Chapter 3 details the ReD experiment, from its conceptual design to the preliminary results presented last year; Chapter 4 covers the convolutional autoencoder I developed, with a discussion of all the components necessary for

designing a neural network and, finally, Chapter 5 presents the steps involved in implementing the CAE-based tagging method and evaluates the performance of it compared to the conventional signal-selection approach used in ReD.

Chapter 1

The Dark Matter

We live in a century that has seen important discoveries come to light, like the Higgs Boson and the first signal of a gravitational wave. Even with the achievement of these key milestones, many other open questions are still waiting for a solution. Among these, the nature of the matter content of the Universe remains one of the key unresolved puzzles in particle physics, astrophysics and cosmology from the 1930s, when Zwicky suggested the existence of a not-luminous mass to explain the observed anomalies in large astrophysical systems. It is now known that about 26% of the total mass-energy balance in the Universe is in the form of non-baryonic, non-dissipative and non-relativistic matter, which also forms large-scale structures in the Universe. We refer to this as *Dark Matter* (DM). Dark matter has dominated the evolution of the Universe since the end of the Radiation Era, shaping what we see today, but what we have so far is only indirect evidence of its existence. The baryonic content of the Universe, which is well understood, accounts for only about 4%. The remaining 69.1% is thought to be dark energy, which is responsible for the accelerated expansion of the Universe. It is generally assumed that DM is probably made up of some new, and yet undiscovered, elementary particle that cannot be part of the Standard Model (SM) paradigm of particle physics, thus providing one of the strongest arguments in support of what is called new physics Beyond the Standard Model (BSM). Other possible explanations for DM have been proposed, like black holes (BHs), most notably primordial black holes (PBHs), other astrophysical objects (MACHOs), or modifications of gravity.

This first Chapter presents the main arguments for the existence of dark

matter, beginning with the initial evidence of its gravitational effects on cosmological objects. It then outlines the primary properties that such matter must satisfy, with a focus on the best experimentally motivated candidate and the techniques employed in its search. Finally, a general overview of the state of the art is provided.

1.1 Evidences for Dark Matter

When an anomaly arises in a well-established paradigm, two possible paths unfold: discredit the theory and turn back, or walk all the way to an unknown destination. The latter was the option followed in 1933 by Fritz Zwicky [1]. He studied the velocity dispersion of eight galaxies in the Coma cluster and found an unexpectedly high value for the dispersion velocity: σ = 1019 ± 360 km/s. By applying the Virial Theorem, which relates the average kinetic and potential energies of a gravitationally bound system, Zwicky concluded that the mean density of the Coma Cluster would have had to be 400 times greater than the one derived only relying on the luminous matter observed. He attributed the discrepancy to the existence of unseen matter, referring to it as *Dunkle Materie* [1], the German for "dark matter", to point out also the difficulty to detect it with traditional methods.

In the same years, Jan Oort studied the velocities of stars in the solar neighbourhood and found that these are too large to be explained by the luminous mass in the Galaxy [2]. These are only the first hints in the list of astronomical and cosmological observations, ranging from galaxies to the entire Universe.

1.1.1 Velocity of galaxies

The most robust and direct evidence for DM on galactic scales comes from the observations of the rotation curves of stars and gas in galaxies as a function of their distance from the galactic center. It was assumed that the orbits of stars within a galaxy would closely mimic the rotations of the planets within our solar system. According to Newtonian dynamics, the rotational velocity is related to the radius:

$$v(r) = \sqrt{\frac{GM(r)}{r}}, \tag{1.1}$$

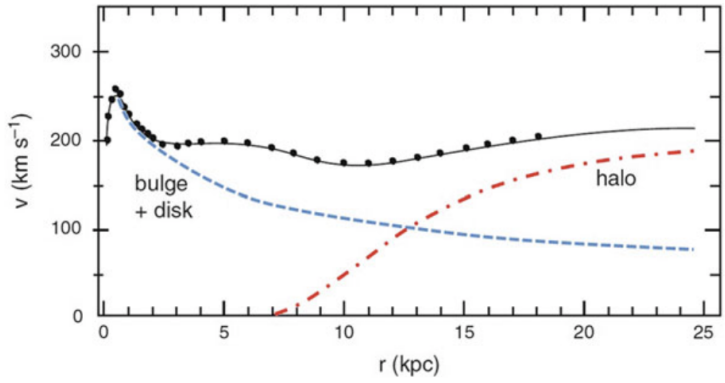

Figure 1.1: Points indicate the measured rotation speeds of stars in the spiral galaxy NGC3198, versus their distance r from the galactic center. The dashed line represents the expected contribution based on the visible matter in the galactic nucleus (bulge) and in the galactic disk; the dotted-dashed line includes the contribution of a halo of dark matter. The solid line is a fit to the experimental data assuming visible matter in the bulge and disk and dark matter in the halo [5].

where $M(r) \equiv 4\pi \int \rho(r) r^2 \, \mathrm{d}r$ is the mass included from the galactic center to the radius r, and $\rho(r)$ is the mass density profile.
A spiral galaxy, such as the Milky Way, has most of the luminous material concentrated in a central hub at small radii, plus a thin disc. In the mid-1960s, Vera Rubin studied the rotation curves of spiral galaxies using a sensitive spectrograph built by Kent Ford, measuring the velocities of clouds of neutral hydrogen with the neutral hydrogen 21 cm emission line[3, 4]. The expected rotation curve should have an increase in the velocity v at small distances from the galaxy center r, consequently falling off at large distances, namely $v \approx r^{-1/2}$. On the contrary, Vera Rubin discovered that all galaxies show a flat, or even slightly increasing, velocity profile after the initial rise, attributed to the central bulge. In almost all cases, after a rise at small r, the velocities remain constant as far as can be measured, as shown in Fig. 1.1 for the spiral galaxy NGC3198.

1.1.2 Gravitational lensing

In the Theory of General Relativity, Albert Einstein explains how the space-time field surrounds us all. The presence of a massive object can distort the gravitational field, bending the light rays passing close to such an object. This is

known as *gravitational lensing*. The greater the mass of the object, the stronger the gravitational potential and therefore the more significant the deflection. Therefore, the mass of a galaxy cluster can be inferred by measuring the deflection angle of the light path.
The lensing effect depends on the total mass of a system, so it should take into account both observable and dark matter. Indeed, by comparing the lensing results with optical observations, it is possible to calculate the missing mass. An example of where the use of gravitational lensing provides a clue to the presence of DM is in the system of the Bullet Cluster. The Bullet Cluster is a particular system formed after the collision of two clusters of galaxies. The majority of light in the system comes from hot X-ray-emitting gas clouds. The behaviour of the elements of the clusters in the collision can be clearly seen in Fig. 1.2: the baryonic X-ray gas particles in the clouds (in pink) interact electromagnetically and with the gravitational force, slowing down and assuming the typical shape of a shock wave in the intergalactic medium; the massive visible objects in orange and white are the stars, which passed through the collision site without any significant change in their motion. Contrary to expectations, the measurement of the gravitational lensing effect showed that the centre of mass does not coincide with the gas clouds, but with the distribution of galaxies (areas marked in blue). DM interacts only through gravity and therefore can pass through each other unhindered by electrostatic interactions as the two clusters escape the collision, causing the observed offset. This offset is then a very strong indication of the presence of a much more weakly interacting form of matter than baryonic matter, with a total mass that far exceeds the baryonic mass.

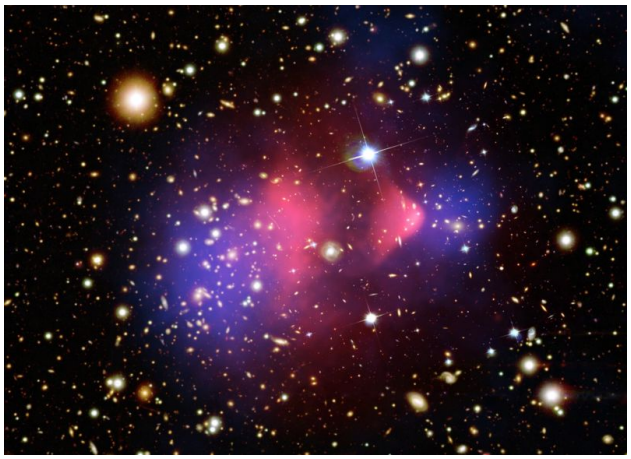

Figure 1.2: Image of the Bullet Cluster. The stars that make up the galaxies are not expected to have substantial interaction during the collision, and most have passed through. In pink, the X-ray data by Chandra, shows the hot gas distribution, compressed after the collision because of the electromagnetic interaction. Hot gas represents most of the baryonic matter in the cluster pair. The blue areas show where most of the mass is located, according to the gravitational lensing effect. It is strongest in two separated regions near the visible galaxies. Image credits: NASA/CXC/M. Weiss, Public domain, via Wikimedia Commons

1.1.3 Cosmological scale

The observations presented so far do not allow to determine the total amount of dark matter in the Universe. This information can be obtained by analysing the Cosmic Microwave Background (CMB), the electromagnetic radiation that fills all space in the observable Universe as a remnant from an early stage in Big Bang cosmology [6]. Neutral atoms formed during the recombination epoch, when the Universe became transparent to electromagnetic radiation and photons have been able to travel freely ever since. The CMB is known to be isotropic at the 10^{-5} level and it follows with extraordinary precision the spectrum of a black body with a temperature of 2.726 K. Despite its isotropic path, CMB presents small anisotropies due to the temperature fluctuations in the early Universe, caused by the under-and over-densities in different regions as particles began to freeze out at different times. The power spectrum is a measure of how much each point in the Universe deviates from the mean temperature, decomposed into spherical harmonics l. The intensity and size of these fluctuations depend entirely on the different components and species present at the time, making the CMB sensitive to the amount of DM present in the Universe. The Planck experiment [8] measured the angular power spectrum of these CMB temperature anisotropies (see Fig. 1.3), and the data were fitted according to the so-called Lambda Cold Dark Matter (ΛCDM) model. This model was developed in the late 1990s, and it was named after the cosmological constant Λ, associated with dark energy and the postulated cold dark matter: *cold* refers to the fact that these particles were non-relativistic at the time of their *decoupling*, when these particles ceased to interact significantly with regular matter or radiation, effectively becoming independent and evolving under the influence of gravity alone. This decoupling allowed cold dark matter to begin clustering under gravitational forces, forming the seeds of large-scale structures such as galaxies and galaxy clusters that are observed today.

The ΛCDM model is based on the general framework of Big Bang cosmology and includes six main parameters associated with different characteristics of the Universe and its components:

- the Hubble constant H_0, which defines the expansion rate of the Universe. The current best estimated value for it is around $\sim 70\,\mathrm{km\,Mpc/s}$
- three density contributions, Ω_Λ, Ω_M and Ω_b, for dark energy, matter and

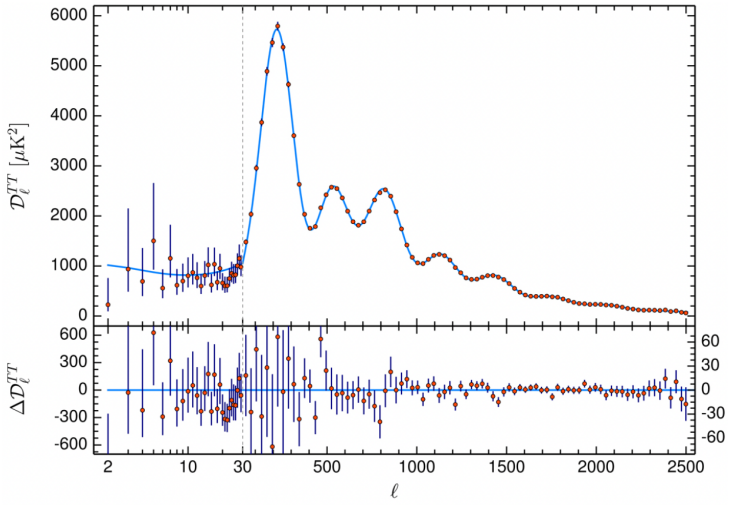

Figure 1.3: Angular power spectrum of CMB temperature anisotropies. Data are shown as blue points with the best fit ΛCDM cosmological model, shown as a red line [7].

baryons respectively, defined as the ratio $\Omega_i = \rho_i/\rho_c$. ρ_c is the critical density required for the Universe to be flat and homogeneous, and it is defined as $\frac{3H_0^2}{8\pi G}$, where $G = 6.67 \times 10^{-11}\,\mathrm{m\,s^2/kg^3}$ is the gravitational constant. It is typically found to be $\rho_c \approx 8.5 \times 10^{-27}\,\mathrm{kg/m}$[1]

- the scalar spectral index n_s, which describes the shape of the primordial density perturbations in the early Universe

- the amplitude of the primordial perturbation A_s, which is related to the magnitude of the temperature fluctuations observed in the CMB radiation.

The power spectrum and the best fit using the six parameters of the ΛCDM are shown in Fig. 1.3. The amplitude of the power spectrum at different values of the multipolar index l, the angular size (π/l) of a given spherical harmonic, gives a quantitative measure of the anisotropies in the CMB, which allows to determine the abundance of different types of particles in the Universe after the freeze-out.

[1] $\rho_c \approx 1.878 \times 10^{-26} h^2 \mathrm{kg/m^3}$, where h is the dimensionless Hubble parameter defined by $H_0 = 100h$ km/s/Mpc. The value for ρ_c quoted in the text is obtained for $h = 0.7$

Parameter	68% limit
Ω_Λ	0.685 ± 0.013
$\Omega_M h^2$	0.1426 ± 0.0020
$\Omega_b h^2$	0.02222 ± 0.00023
$\Omega_{CDM} h^2$	0.1197 ± 0.0022
H_0	67.31 ± 0.96

Table 1.1: Density parameters obtained by the Plank Collaboration [7]. Both the baryonic and cold dark matter density contributions are reported. $h = H_0/(100\,\mathrm{kms}^{-1}\mathrm{Mpc}^{-1})$ is the reduced Hubble constant.

The values obtained by Plank for the density components are summarized in Tab. 1.1. The results for the i-th component are given in terms of the density parameter $\Omega_i = 8\pi G\rho_i/3H_0^2$, where G is the gravitational Newton's constant, and are constrained with an accuracy of less than 2%, pointing to the conclusion that 85% of the matter content of the Universe is in fact dark.

1.2 Properties and particle candidates

Once the existence of dark matter has been established, the evidence outlined above must be used to infer its possible properties, guiding the identification of potential experimental approaches for its detection. In principle, the DM puzzle could be explained in terms of something else than particles, but such approaches suffer from problems. This approach includes modifying gravity (MOND) [9] which still needs to invoke DM in order to explain all data [10], or cosmic fluid [11] which is also increasingly challenged by observations. Gravitational waves observed by the LIGO/VIRGO collaboration have discarded many theories of modified gravity [12, 13].

A preliminary hypothesis to solve the DM puzzle was to look for massive non-luminous objects that could populate the galaxies' halos, like black holes, neutron stars, unassociated planets, or brown dwarfs that would emit very little to no radiation. This family of astronomical bodies is usually referred to by the acronym MACHOs, which stands for *MAssive Compact Halo Objects*. To test this theory, MACHOs objects were searched using gravitational microlensing, that is gravitational lensing effect at masses of the order of 10^{-7} solar masses, toward

the Large Magellanic Cloud [14]. However, the results obtained showed that these candidates could explain at most 20% of the effect due to DM. One alternative is primordial black holes, formed in the early stages of the Universe and therefore not bound by cosmological parameters [15], but this has also been discarded [16].

The study of the properties of the CMB indicates that DM is non-baryonic, although this does not in itself constrain the possible form of DM interactions. Dark matter contributes gravitationally to the Universe, and it is also clear that candidate DM particles do not have electromagnetic charge, otherwise their detection through traditional techniques would have been more straightforward. Furthermore, the observed structure and evolution of the Universe are consistent with DM particles having non-strong interactions [17]. The other possible DM interaction with the ordinary matter should be the weak interaction, where weak may stand for both the standard weak force and, or instead some other (sub)weak force defined by some coupling to SM particles. DM particles could also interact with themselves, and this type of self-interaction is in fact rather poorly constrained. Dark matter particles should also be either absolutely stable, or extremely long-lived $\tau_{DM} \gtrsim t_{\text{Universe}}$, otherwise they would have already decayed.

As already mentioned, it is assumed the non-relativistic nature of DM according to the ΛCDM model. In the context of cosmology and astrophysics, the terms *cold* and *hot* refer to the initial velocities or kinetic energies of particles in the early Universe in comparison with the speed of light. It implies that a cold DM particle would have a velocity much lower than the speed of light at the time of decoupling, whereas a hot DM particle would move relativistic. In the latter scenario, the high velocities of the DM particles would have made it difficult to form structures on small scales, leading to the smoothing out of small-density perturbations. The cold DM hypothesis is instead consistent with the observed large-scale structure of the Universe, such as the distribution of galaxies and galaxy clusters [18]. The slow velocities of cold DM particles allow them to cluster gravitationally and form structures from the bottom up, starting with small-scale structures that later merge to form larger structures.

Finally, the last question to consider in identifying the possible candidate is how heavy DM is. The mass range is extremely wide, and can cover nearly 50 orders of magnitude, from values as small as 10^{-21} eV (fuzzy DM) for bosons with de Broglie wavelength of the order of typical size of dwarf galaxies [19] up

to the reduced Planck scale $\overline{M}_P \simeq 2.4 \times 10^{18}$ GeV.

This is as far as we can be fairly certain about the general properties of DM, but it is only a first step towards identifying its real nature since they can easily be satisfied by a wide range of specific particle candidates, or indeed classes of candidates. Many frameworks of BSM contain viable DM candidate particles. In the following, I briefly discuss some of the most motivated candidates.

1.2.1 Sterile neutrinos

Neutrinos are the only electrically neutral and long-lived fermions in the SM. Neutrinos were involved in weak interactions that kept them in thermal equilibrium down to temperatures of a few MeV in the early Universe. Furthermore, the observed oscillations in neutrino flavors have experimentally proved that neutrinos are massive, in contrast to the predictions of the SM. Although they seem to be good candidates for DM, the neutrinos were relativistic at the time of decoupling and, as hot dark matter, could not have contributed to the formation of large structures. However, some studies are introducing a new neutrino flavor, the so-called *sterile neutrino*, since it does not interact with the electroweak force, apart from the mixing with active neutrinos. It is defined as an electrically neutral massive particle, which does not interact through any fundamental force, except gravity, and non-relativistic [20]: this would be in agreement with DM properties and with the bounds on neutrinos masses, since these only concern relativistic species.

1.2.2 Axions

A class of non-thermal relics that is theoretically highly motivated is axions and axion-like particles [21]. The axion is a hypothetical neutral pseudoscalar boson. It was proposed by Peccei and Quinn [22] as an attractive solution to the *strong CP problem*. It arises from the non-Abelian nature of the quantum chromodynamics (QCD) gauge symmetry, or color symmetry. The strong interaction Lagrangian should violate the charge-conjugation and Parity symmetry (CP), but this breaking of symmetry has not been observed experimentally, although there is no known reason in QCD for it to be necessarily conserved. Peccei and Quinn proposed a spontaneous breaking of a new U(1) chiral symmetry, whose associated Goldstone boson would be axion. If axion exists, it

could be a promising candidate for DM because it couples weakly to ordinary matter.

1.2.3 WIMPs

In the past few decades, one of the most investigated candidates was the so-called *Weakly Interactive Massive Particle* (WIMP). In the past, WIMPs have also been theoretically proposed within the framework of low-energy supersymmetry (SUSY), a theory initially developed to address the gauge hierarchy problem in the Standard Model. An attractive candidate for WIMPs, the neutralino, naturally arises within SUSY as a byproduct of these efforts. However, supersymmetry searches at colliders up to $\sqrt{s}$= 13 TeV have only given null results [23]. WIMPs have attracted the most attention because they should have been produced at an early and hot stage of the evolution of the Universe by a thermal freeze-out mechanism when SM and DM particles were at their thermal equilibrium.

They are expected to be stable particles, cold at the time of decoupling, colorless and electrically neutral, and to interact with SM matter with the coupling characteristic of weak interactions in addition to gravity. Predicted WIMP masses are typically in the range from a few GeV/c^2 up to tens of TeV/c^2.

The DarkSide program is involved in the search for WIMPs, so in this work, I will focus more on describing this candidate.

1.3 Believing in WIMPs experimentally: the WIMP miracle

What makes WIMPs such an attractive candidate is the theoretical production model: according to this mechanism, WIMPs are produced with a relic density consistent with that required for DM, and this is known as the *WIMP miracle*. In its first stage, the Universe was hot and dense, and all particles, both DM, denoted by the letter χ, and SM ones, were in equilibrium as a thermal plasma. As the Universe cooled at a temperature T_f lower than DM mass (m_χ) and expanded, WIMPs froze out of equilibrium with the plasma. This decoupling occurred when the annihilation rate Γ^{χ}_{ann} fell below the rate at which the Universe

expands, called the Hubble parameter H,

$$\Gamma^{\chi}_{ann} \lesssim H \propto \frac{T_f^2}{\overline{M}_P}, \tag{1.2}$$

where $\overline{M}_P$ $\left(2.4\times10^{18}\text{GeV}\right)$ is the reduced Plank mass. Therefore, the number of DM particles asymptotically approached a constant, which is the comoving relic number density. Employing the Boltzmann equation

$$\frac{\mathrm{d}n}{\mathrm{d}t} = -3Hn - \langle\sigma_{ann}v\rangle\left(n^2 - n_{eq}^2\right) \tag{1.3}$$

it is possible to calculate the relic density. In Eq. 1.3, n is the number density of DM particle χ, H is the Hubble parameter, $\langle\sigma_{ann}v\rangle$ is the thermally averaged product of the cross-section for WIMP pair annihilation and their relative velocity, and n_{eq} is the DM number density at the equilibrium. The solution for the relic density by solving Eq. 1.3 is

$$\Omega_\chi h^2 \sim \frac{x_f T_0^3}{\rho_0 \overline{M}_P}\langle\sigma_{ann}v\rangle^{-1}, \tag{1.4}$$

where h is the Hubble constant in units of 100 km/(s Mpc), the quantities n, T and ρ with subscripts 0 are the present day number density, temperature and density respectively. The ratio $x_f = m_\chi/T_f$ is typically equal to 20. The relic density is inversely proportional to $\langle\sigma_{ann}v\rangle$, that is the thermally averaged product of the cross-section for WIMP pair annihilation and their relative velocity. At the freeze-out it is numerically found $\langle\sigma_{ann}v\rangle \approx 3\times10^{-26}\,\text{cm}^3/\text{s}$: the velocity is assumed to be $v = 0.1\,c$ and σ_{ann} of the weak scale is of the order of $\simeq 10^{-36}\,\text{cm}^2$.

So this coincidence is the WIMP miracle: WIMP with such a cross-section comparable to the weak scale results in the correct thermal DM relic density of Ω_{CDM}= 0.27 [24]. WIMPs are expected to be BSM particles with a mass scale close to the electroweak scale, and their expected detection rates match the sensitivity range of current and planned detectors, thus increasing the experimental interest in this class of detectable candidates. WIMPs properties could be substantially different from the electroweak scale. Denoting the WIMP effective coupling to the SM particles, on a dimensional ground one often finds $\sigma_{ann} \propto g^4/m_\chi^2$, and keeping the ratio fixed, the correct relic density can be achieved for a very wide range of g, from gravitational to strong, and also m_χ, from ~ eV to 120 TeV, consistent with the freeze-out mechanism [25–27].

1.3.1 Light WIMPs

Over the past ten years, WIMPs in the mass range of few GeV to few TeV were largely searched, even if up to now all the experiments did not observe any signal, except for the DAMA/LIBRA results [28]. Recently, the search for lighter WIMP candidates diffused, the so-called *low mass* WIMP. The reason why at the beginning a low mass WIMP was not considered is because it did not seem to have the correct relic density: smaller WIMP masses would be associated with lower annihilation cross-section, resulting in an excessive relic abundance, since in that context WIMPs are considered to be fermions and thus having an annihilation cross-section proportional to their mass [29]. Considering a scalar WIMP results instead in a relic density dependent on the coupling g with ordinary matter, rather than on the m_χ [29]. This is the reason why big efforts have been made by several WIMP-searching experiments to increase their sensitivity to smaller energy depositions and lighter DM candidates.

1.4 How to detect a Dark Matter particle

Once the pieces of evidence and possible candidates have been discussed, it is needed to study the possible interaction of DM particles with SM particles and how it could be possible to detect it. Fig. 1.4 summarizes the possible interaction channels and it can be read in three directions: from top to bottom for annihilation, from left to right for scattering or from bottom to top for direct production. One could refer to these using the experimental approach used as indirect detection, direct detection and production at accelerators, respectively.

Production at accelerators: while interacting, two SM particles could produce DM particles. This process could occur at particle colliders, like the Large Hadron Collider (LHC), and the produced DM particles could be seen as missing energy and momentum in the collision products. Despite big efforts, there has been no evidence of DM particles observed so far with this technique [30].

Indirect detection: this approach focuses on looking for SM particles produced by DM in mechanisms like annihilation, oscillations, and decays, as well as the secondary effects of particles that occur in the Sun, Earth or other

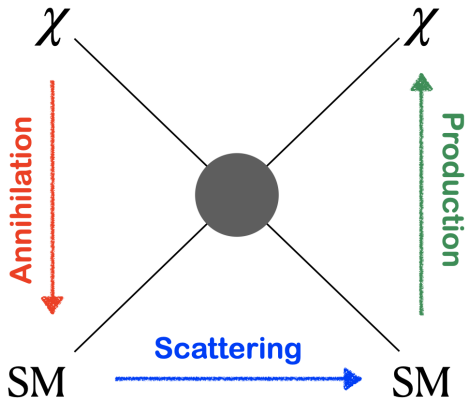

Figure 1.4: This diagram summarizes the three possible interactions through which dark matter may be detected. Two dark matter particles can annihilate each other, producing Standard Model products (red line from top to bottom). Conversely, two Standard Model particles can interact to produce two dark matter particles (green line, from bottom to top). Finally, dark matter scattering off a standard particle can produce a detectable signal (blue line, from left to right).

astrophysical sources. Indirect searches are carried out using telescopes originally designed for astronomy and astrophysics, which are sensitive to various SM particles, like photons (Fermi-LAT, CTA), Neutrinos (IceCube, ANTARES/KM3NeT), cosmic ray positrons, cosmic ray antiprotons (AMS), and cosmic ray anti-helium. An excess of these kinds of particles, produced by various galactic sources, could potentially be caused by DM. The most challenging aspect in this research field is the weak interaction between DM and SM particles resulting in a small expected rate of particle production and potential large backgrounds from astrophysical particle production.

Direct detection: DM particles could also interact with the baryonic matter which detectors are made of, resulting in nuclear recoils (NR) produced by the collision of DM particles with the target nuclei. The experimental signature consists of the energy deposited in the detector, which is converted into a detectable signal through different processes such as scintillation, ionization, or phonon creation. Due to the presence of cosmic rays and natural radioactivity that could overwhelm these rare events, Earth-

based detectors used in this direct detection approach must be built underground with extremely radio-pure materials and require a deep study of the background.

The ReD experiment that I worked on during my Ph.D. and that is discussed in this thesis was designed with a direct DM detection approach, as was the entire DarkSide experimental program, so I will focus on direct detection techniques in the following.

1.5 Cross-section and event rate for WIMP signal

WIMP particles that elastically scatter off nuclei transfer to the nucleus a small amount of energy, named recoil energy E_R, that is given by

$$E_R = \frac{\mu^2 v^2}{m_N}\left(1-\cos\theta_{CM}\right) \tag{1.5}$$

where μ is the WIMP-nucleus reduced mass defined as $\frac{m_\chi m_N}{\left(m_\chi+m_N\right)}$, v is the WIMP velocity and θ_{CM} is the scattering angle in the center-of-mass frame.

Considering the case of a WIMP with m_χ in the range of tens of GeV/c^2 , with a $v \sim 220$ km/s, which is the average velocity relative to the Earth of the DM in the Milky Way halo [31], it would produce in Ar $\left(m_N \sim 40\,\text{GeV}/c^2\right)$ NRs of the order of tens keV [32]. The identification of such a low-energy interaction requires detailed knowledge of the event signature, the particle physics aspect and the nuclear physics modelling. Given the weak nature of WIMP interactions, the probability of a WIMP undergoing multiple collisions within the detector is negligible. Therefore, a spectrum of single-scattering events constitutes a key signature.

The event rate for recoil energy can be written as

$$\frac{\mathrm{d}R}{\mathrm{d}E_R} = N_t \Phi_\chi \frac{\mathrm{d}\sigma}{\mathrm{d}E_R}. \tag{1.6}$$

N_t is the total number of particles in the target and can be written as the ratio between the total target mass and the nuclei mass. Considering a unit mass detector it could be written as $1/m_N$, where m_N is the nuclei mass.

Φ_χ denote the dark matter flux, and can be expressed as a function of the density and the velocity distribution $\Phi_\chi = \nu_\chi v f(v) dv$. The number density can be written as $\nu_\chi = \rho_\chi / m_\chi$, that is the ratio between the local mass density and the mass of the WIMP.

$\frac{d\sigma}{dE_R}$ is the differential cross-section. It must be related to the differential scattering cross-section per solid angle.

Therefore, by rewriting the rate, the differential recoil spectrum due to the interaction of a WIMP with a target can be expressed as

$$\frac{dR}{dE_R} = \frac{\rho_\chi}{m_\chi m_N} \int_{v_{min}}^{+\infty} v f(v) \frac{d\sigma}{dE_R} dv. \tag{1.7}$$

The integral is calculated from the minimum WIMP velocity (v_{min}) up to all the possible velocities. v_{min} is obtained from Eq. 1.5 as the minimum velocity needed to have a nuclear of energy E_R

$$v_{min} = \sqrt{\frac{m_A E_R}{2\mu^2}}. \tag{1.8}$$

The astrophysical parameters ρ_χ and $f(v)$ are derived from astrophysical models of the galactic halo and given as input parameters, while the experimental observables are the WIMP-nucleus differential cross-section and m_χ. The latter, as calculated in[31, 33], is equal to

$$\frac{d\sigma}{dE_R} = \frac{|M|^2}{32\pi m_\chi^2 m_A v^2}, \tag{1.9}$$

in which M is the scattering amplitude.

Considering how the DM particles interact with the target nucleons, two scenarios could be considered: Spin-Independent (SI) interactions, where the contribution of neutrons and protons to the scattering mechanism is equal (isospin conservation), and Spin-Dependent (SD) interactions, where only unpaired nucleons contribute to the scattering. Focusing only on the Spin-Independent cross-section, the associated amplitude is [34]

$$|M|^2_{SI} = 16 m_\chi^2 m_A^2 \left| f_p Z + f_n (A - Z) \right|^2 \left| F(q) \right|^2, \tag{1.10}$$

where Z and A are the atomic number and the mass number of the target, f_p and f_n are the WIMP coupling to the proton and neutron and $F(q)$ is the nuclear form factor. Substituting Eq. 1.10 in Eq. 1.9 the WIMP-nucleus differential

cross section becomes

$$\frac{\mathrm{d}\sigma_{SI}}{\mathrm{d}E_R} = \frac{m_A}{2\pi v^2}\left|f_p Z + f_n(A-Z)\right|^2 \left|F(q)\right|^2 \tag{1.11}$$

that leads to the expression of the differential rate

$$\frac{\mathrm{d}R}{\mathrm{d}E_R} = \frac{\rho_\chi}{2\pi m_\chi}\left|f_p Z + f_n(A-Z)\right|^2 \left|F(q)\right|^2 \int_{v_{min}}^{v_{max}} \frac{f(v)}{v} dv. \tag{1.12}$$

The rate can be further simplified by assuming that the WIMPs are distributed as an isothermal sphere with an isotropic Maxwellian velocity distribution, in line with the Standard Halo Model (SHM). The velocity integral gives a roughly exponential spectrum. The upper limit is the escape velocity

$$\frac{\mathrm{d}R}{\mathrm{d}E_R} \propto \left|f_p Z + f_n(A-Z)\right|^2 \left|F(q)\right|^2 e^{-\frac{E_R}{E_0}} \tag{1.13}$$

where $E_0 = 2\mu^2 v_0^2 / m_A$ and $v_0 = 220\,\mathrm{km/s}$ the average velocity of the DM in the Milky Way halo discussed earlier in this section. In many dark matter models, WIMPs are assumed to interact similarly with both protons and neutrons due to isospin symmetry. This assumption implies that the coupling constants for WIMP-proton and WIMP-neutron interactions are approximately equal, i.e., $f_p \approx f_n$. Consequently, in SI interaction models, setting $f_p = f_n \sim 1$ further simplifies the calculation, leading to a reduction in the complexity of Eq. 1.13 to

$$\frac{\mathrm{d}R}{\mathrm{d}E_R} \propto A^2 \left|F(q)\right|^2 e^{-\frac{E_R}{E_0}} \tag{1.14}$$

This contains two very important pieces of information: first, the dependence on A^2, which indicates that for the same mass of the target, heavier elements provide a higher rate of scattering interactions, and second, for the threshold energies in the detectors, it must be taken into account that the rate decreases exponentially with E_R. The expected recoil energy spectrum at different nuclei is shown in Fig. 1.5 (a), where it is possible to note that the expected rate for direct WIMP detection is low, not higher than 10^{-5} counts/day/kg/keV. In addition, the oscillations observed in the energy spectrum of the predicted recoil are due to the nuclear form factor. These oscillations occur because the form factor takes into account the internal structure of the nucleus, which affects the scattering process, especially at higher recoil energies.

The challenge of current experiments is to identify and count events above a threshold that is determined by experimental factors such as background and detector efficiency. Fig. 1.5 (b) shows the integrated rate as a function of the energy threshold: the integrated rate is of the order of 10^{-3} counts/day/kg for the lowest energy threshold, thus making WIMP searches strongly challenging.

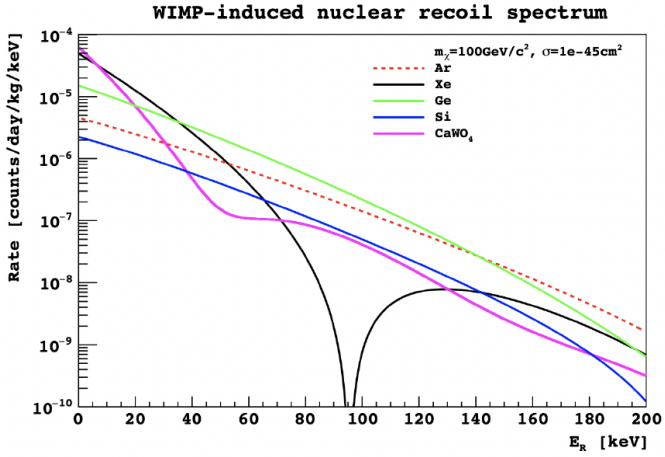

(a)

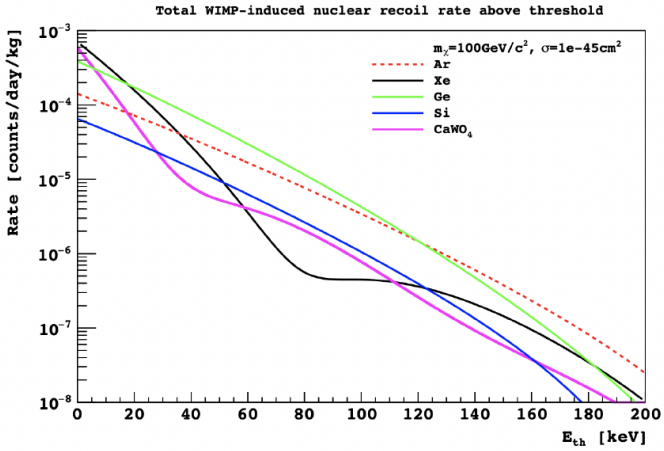

(b)

Figure 1.5: **(a)** Expected recoil energy spectrum calculated for different target nuclei assuming a WIMP mass of $100\,\mathrm{GeV}/c^2$, $\sigma = 1\times10^{-45}\,\mathrm{cm}^2$ and SHM parameters. For the same targets, in **(b)** are reported the integrated rates as a function of the energy threshold E_{th} [31].

1.6 Direct detection techniques and status of the art

A WIMP particle elastically scattering off the target nucleus will transfer energy to the nuclei, which could be seen in direct detection experiments in the form of *heat production*, *charge* and *light signals* (Fig. 1.6). These signals are proportional to the energy deposited in the detector, and by combining two of these detection channels it is possible to perform pulse shape discrimination (PSD) based on the type of particle depositing the energy, providing a powerful tool for background discrimination.

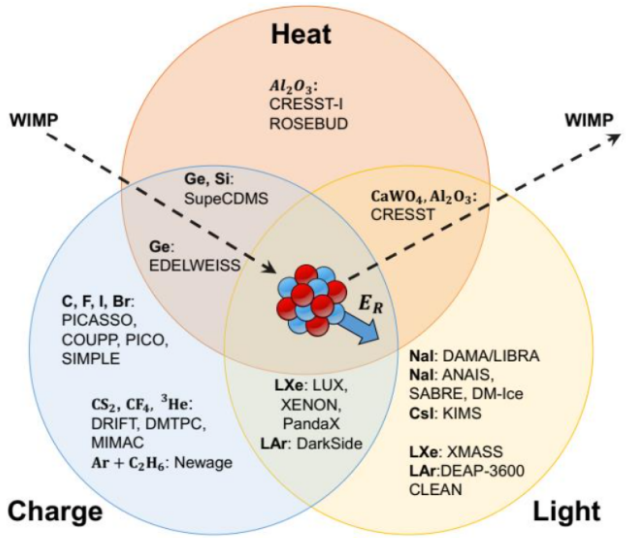

Figure 1.6: This diagram illustrates the three primary channels for detecting energy deposition in a detector by a dark matter particle. For each type of energy, corresponding experiments designed to detect signals specific to that channel are presented. The interconnected circles were deliberately chosen to emphasize that experiments can be constructed to detect signals from two of the three channels simultaneously. The observation of two distinct signals provides a robust method for verifying the detection and enables the discrimination of the properties of the particle responsible for the observed signals.

The **heat** detection techniques are related to the phonons generated by a nuclear recoil in a crystal lattice. Phonons are collective excitations of lattice atoms that induce a tiny temperature fluctuation within the target material. Detectors operating with this detection approach are bolometers, which use

crystals cooled at cryogenic temperature to measure the variation in resistivity that allows reconstructing temperature fluctuations at the order of μK. Other detectors that exploit heat are bubble chambers filled with superheated liquids as targets. The liquids are kept at a temperature just above their boiling point so that a local phase transition creates a bubble of energy above a certain threshold that is deposited in a microvolume.

The scintillation phenomenon involves the emission of optical photons by excited atoms within a material. The de-excitation results in a **scintillation light** that can be detected using a photosensor, like a photomultipliers tube (PMT) or silicon photomultipliers (SiPM). A good scintillator should have high efficiency for converting excitation energy into fluorescence radiation, and be transparent to its own fluorescence radiation to allow transmission of light. In addition, to be used in DM searches, the scintillator must meet the levels of radio-purity essential for low background experiments, and a short de-excitation time between the scattering event and the emission of light to disentangle multiple scattering events caused by background particles. Materials that fulfill these properties are high-purity scintillator crystals, like NaI(Tl), Cs(Tl) or $CaWO_4$, and noble cryogenic liquids such as Argon and Xenon. These latter are used in single-phase Time Projection Chambers (TPC). In addition, noble gases possess a combination of favorable properties, including low ionization energy, weak interatomic forces, and a high atomic number, making them highly efficient for detecting and amplifying ionization events. These properties make them ideal for use in dual-phase (liquid and gas) TPCs, where both the primary scintillation light and the ionization electrons can be detected

Specifically, the third detection channel involves **ionization charge**. When the impinging particle deposits enough energy in the target, some of its atoms may be ionized, generating free electrons or energy-hole pairs that can be collected by establishing an electric field in the detector to avoid recombination effects. Examples of ionization detectors are germanium and silicon semiconductor detectors. Those detectors have an excellent energy resolution since only a small amount of energy is needed to create an electron-hole pair, 2.9 eV and 3.6 eV for germanium and silicon, respectively. In addition to the dual-phase scintillating noble element TPCs mentioned above, other examples of detection channel combinations are scintillating bolometers for phonon and

light detection, and Ge or Si crystals equipped to measure the phonon signals as well.

Fig. 1.6 provides a graphical overview of the experiments involved in the direct search for dark matter, categorized by their respective detection channels. Several of these experiments are designed to simultaneously detect multiple types of signals, which are represented by the intersections of the circles. In direct dark matter searches, the ability to detect two distinct signals offers significant advantages, such as enhancing the credibility of detected events, aiding in the identification of the interacting particle, and improving the overall sensitivity to dark matter interactions. This dual-channel sensitivity is particularly valuable for minimizing background interference, refining particle identification, and increasing the robustness of the experimental results, making it a vital strategy in the ongoing efforts to detect dark matter.

The current exclusion limits set by the main experiments that, exploiting different techniques, are involved in the direct detection of DM particles are reported in Fig. 1.7.

Below is an overview of past and ongoing experiments focused on the search for DM particles. To summarize, here are the characteristics that any direct dark matter particle search experiment must possess, according to what is discussed in Sec. 1.5. Such a detector must be able to achieve a low-energy threshold to detect small recoil energies, be stable in its performance over the time scale of a few years, have a large volume to increase the exposure and thus the probability of interaction within the target, and be built with radio-pure materials and operated in underground laboratories with efficient shielding to keep the background at low levels and increase the statistical significance of the observations.

CRESST (Cryogenic Rare Event Search with Superconducting Thermometers) was the first project to employ scintillating crystals as cryogenic detectors for DM searches, being up to now the leading experiment adopting the approach of measuring simultaneously heat and scintillation light signal. It is located at INFN, Laboratori Nazionali del Gran Sasso (LNGS) in Italy. CRESST-III is the third generation of CRESST, specifically designed to have a world-leading sensitivity for DM with mass $< 2\,\mathrm{GeV}/c^2$. It uses scintillating small $CaWO_4$ crystals as target material operated at ~10 mK [36]. In detail, 10 scintillating crystals of (20×20×10) cm^3 for ~25 g each

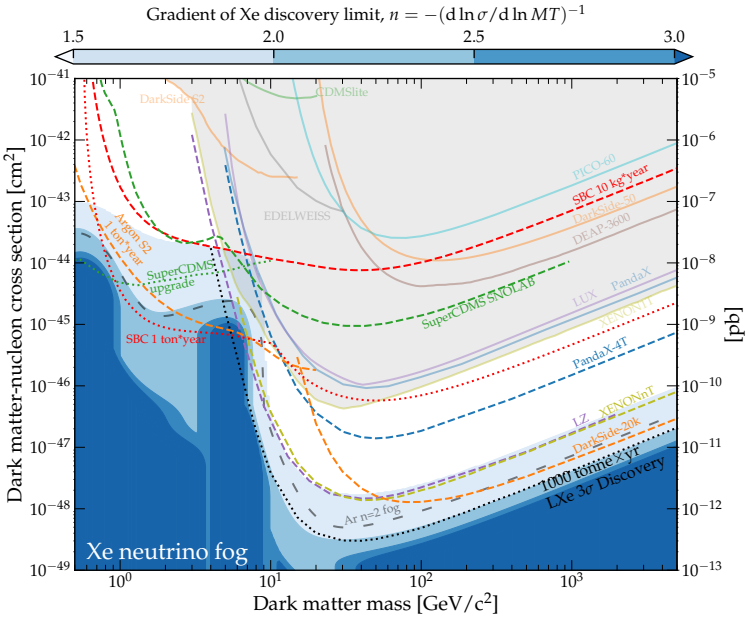

Figure 1.7: Upper limits on the spin-independent WIMP-nucleon cross-section for past (solid lines) and future (dashed lines) experiments as a function of the WIMP mass. The region of the phase space in grey is the one already excluded, while the region colored in the blue scale marks where the neutrino background becomes dominant [35].

are organized in an array that is read out as cryogenic calorimeters and scintillating detectors, thus providing a tool for particle identification on an event-by-event basis to suppress background induced by charged particles, while the heat signal provides a precise measurement of the total energy deposition independent from the nature of the interacting particles. It completed the first data taking in 2018 [37].

CDMS (Cryogenic Dark Matter Search) employs Ge detectors equipped with low-impedance Transition Edge Sensors (TES) and ionizing electrodes to detect heat and charge. The first campaign was operated in 2016 in the Soudan underground facility, hence the name SuperCDMS-Soudan phase [38]. CDMS achieved the world leading Ge-based WIMP constrain

from $\sim 1.5\,\mathrm{GeV}/c^2$ to $250\,\mathrm{GeV}/c^2$ [39–41]. By amplifying the signal via the Neganov-Trofimov-Luke (NTL) effect in a gram scale Si detector, the SuperCDMS demonstrate sensitivity to single $e^- - \mathrm{h}^+$ pair for the first time [42], providing also the first silicon calorimeter based sub-MeV/c^2 DM-electron constraints. CDMS is currently building SuperCDMS SNOLAB, an experiment designed to search for nucleon-coupled DM in the 0.5-5 GeV/c^2 mass range.

XENONnT XENONnT is a dual-phase xenon (LXe) TPC used to detect both light and charge signals. It is the latest upgrade of the XENON1T detector [43] designed by the XENON Dark Matter project and it is shaped as a cylinder with a diameter of 1.33 m and a height of 1.49 m of 5.9 t (fiducial volume 4 t) of LXe enclosed by 24 polytetrafluoroethylene (PTFE) reflector panels. The XENON experiment is hosted in the Hall B of INFN LNGS, and it has been collecting data since 2020. It is equipped with 494 3-in diameter PMTs divided in two arrays placed on the top (253 PMTs) and the bottom (241 PMTs) of the TPC and arranged in a compact hexagonal structure to maximize the light collection efficiency. XENONnT performed a blind analysis of nuclear recoil events in the energy range from 3.3 keV to 60.5 keV, finding no excess and thereby setting a minimum upper limit on σ_{SI} of 2.58×10^{-47} cm^2 for a WIMP mass of $28\,\mathrm{GeV}/c^2$ at the 90% confidence level [44].

LUX-ZEPLIN (LZ) is a LXe TPC operating 1480 m underground in the Davis Cavern at the Sanford Underground Research Facility (SURF) in Lead, South Dakota, USA. The active volume of 7 t (5.6 fiducial) of LXe is contained in a double-walled Titanium cryostat. The TPC has a cylindrical shape (1.5 m diameter and 1.5 m height) clad in PTFE and instrumented with 494 PMTs (3-in diameter) divided into two arrays on the top and on the bottom. To detect and veto signals due to background the TPC is surrounded by two detectors. The so-called *skin detector* is a thin volume of $\sim$ 2 t of LXe surrounding the TPC and it is monitored by 131 additional PMTs. Since the presence of a signal in this region indicates that an interaction in the TPC is not from a WIMP, it is used as an anti-coincidence detector. The second veto, surrounding the double-wall cryostat, is the *outer detector* is made of 17 t of Linear AlkylBenzene (LAB) scintillator doped with Gadolinium to enhance neutron detection. Acting as a neu-

tron veto, it tags ~90% of the neutrons that generated a single scatter signature inside the TPC. The shielding layers are completed by an active water Cherenkov muon veto. The sensitivity of LZ to SI WIMP-nucleon couplings is $1.5 \times 10^{-48}\,\mathrm{cm}^2$ (90% C.L. $40\,\mathrm{GeV}/c^2$ WIMP) [45].

DEAP-3600 is a single-phase liquid argon (LAr) detector: such a technology looks for WIMPs only by inspecting the light channel. It is located at approximately 2 km (6 km water-equivalent) underground at the SNOLAB facility near Sudbury, Canada. It consists of a spherical acrylic vessel of 85 cm of radius filled with 3.3 t of atmospheric argon. The inner part of the sphere is coated with Tetraphenyl butadiene (TPB) wavelength-shifter for efficient detection of the scintillation light observed by 255 8-inch diameter PMTs coupled to the vessel through 45 cm long acrylic light guides. DEAP-3600 has exploited PSD to achieve electron recoil background rejection with a leakage probability of 4.1×10^{-9} with 90% acceptance for nuclear recoils, reducing this background to insignificance. The experiment holds the most stringent exclusion limit in argon for WIMPs above $20\,\mathrm{GeV}/c^2$ [46].

DarkSide-50 was a dual-phase LAr TPC operated between 2013 and 2019 in the Hall C of INFN LNGS. Except for the first two years of data-taking in which it used atmospheric argon, DarkSide-50 was filled with 50 kg of low-radioactivity argon with reduced activity of cosmogenic isotopes. The active volume was a cylinder of 36.65 cm in diameter and height with a structure made of PTFE. The PTFE sidewalls were surrounded by copper rings to establish a uniform electric field of 200 V/cm in the liquid volume. The optical sensors employer were 38 3-in diameter PMTs equally divided in two arrays installed respectively on the top and bottom part of the detector. Photons emitted in argon are in the UV, so the PTFE and the fused silica windows at the top and bottom of the cylinder are coated with TPB wavelength shifter, that absorbs the 128 nm photons emission and reemits softer photons with a peak wavelength at 420 nm. The veto system consists of a Liquid Scintillator Veto (LSV) operated as a hermetic neutron veto, immersed in a Water CherenkoV Veto (WCV) against cosmic muons [47]. DarkSide-50 was able to set an upper limit on the DM-nucleon SI cross-section of $1.14 \times 10^{-44}\,\mathrm{cm}^2$ ($3.78 \times 10^{-44}\,\mathrm{cm}^2$, $3.43 \times 10^{-43}\,\mathrm{cm}^2$) for a WIMP mass of $100\,\mathrm{GeV}/c^2$ ($1\,\mathrm{TeV}/c^2$, $10\,\mathrm{TeV}/c^2$) per-

forming a blind analysis of a (16660 ± 270) kg·d exposure of low radioactive argon mined from underground deposits [48].

Chapter 2

Liquid Argon and the DarkSide programme

Over the past decades, dual-phase Time Projection Chambers (TPCs) filled with noble gases have become a leading technology in the direct detection of WIMP particles[44, 48]. The strength of this approach lies in the intrinsic radiopurity and scalability of the target material, as well as the precise topological reconstruction achieved through the detection of both scintillation and ionization signals. Xenon and argon are the primary elements utilized, leading to a differentiation within the scientific community based on the choice of target for different experiments.

Xenon is an excellent scintillator, with a wavelength of 178 nm, and can be ionized easily (W = 15.6 eV). Due to its high density (Z = 54 and $\rho = 2.8\,\mathrm{g/cm}$) it is possible to build massive and compact detectors with self-shielding capabilities. Eq. 1.14 shows that the interaction rate scales as A^2: with its mass number of 131.3, Xenon serves with excellent sensitivity to SI interactions. LXe-based TPCs are also leading the search for WIMPs with mass above a few GeV/c^2, thanks to the very low energy threshold of $\sim$ 1 keV$_{ee}$ (electron equivalent) and $\sim$ 5 keV$_{nr}$ (nuclear recoil equivalent) when reading out both light and charge signals. The use of individual scintillation photons in the analysis can further reduce the threshold, while only using the charge signal is possible to reach a lower threshold of a few electrons thus extending the sensitivity down to 2 GeV/c^2 for a WIMP-nucleon scattering of 1.6 keV$_{nr}$ threshold [49].

Also, liquid argon has a fairly similar performance as LXe in terms of ioniza-

tion yield. LAr has an atomic mass of 40 and a density of 1.4 g/cm, lower than the LXe one. On the one hand, due to its lower target mass compared to LXe, an LAr TPC has a reduced interaction probability, requiring longer exposure times to achieve the same sensitivity. On the other hand, a low-mass WIMP scattering off argon produces more energetic recoils, with a higher probability of being detected above the threshold. This aspect has enabled DarkSide-50 to compensate for the smaller argon cross-section and position itself as the most sensitive detector currently available for interactions in the $[1.8-3.0]\,\mathrm{GeV}/c^2$ mass range, with a fiducial LAr target of only $\sim 20\,\mathrm{kg}$ [50].

Another notable difference between LXe and LAr is related to the ability to discriminate nuclear recoil (NR) events from electron recoils (ER) events of the background by using the PSD technique. When charged particles excite atoms, they form excimers before emitting scintillation light. This light consists of two components with different decay times: a fast component from the singlet state and a slow component from triplet state excimers. The decay constants of these two components are 4.3 ns and 22 ns for LXe, 7 ns and 1.6 µs for LAr, respectively [51]. In LXe, the discrimination is performed using the ratio of ionization charge to scintillation light in the event, which is higher for ER events than NR events. However, due to the similarity of the singlet and triplet scintillation decay time, PSD based on the singlet/triplet population is not powerful for xenon. The obtained rejection of the ER events is to the 10^{-3} level at 50% NR acceptance [52]. The rejection level remains essentially constant down to the low energy threshold and, due to the partial overlap of the ER and NR distributions, can be increased by reducing the NR acceptance. However, effective PSD would require many detected scintillation photons, which would be incompatible with the low-threshold goal of LXe detectors.

In conclusion, LAr is advantageous for detecting potential WIMPs across a wide mass range, including the 100s of GeV/c^2 scale due to its highly effective suppression of ER background through PSD, as well as the increasingly studied low-mass WIMPs. LAr technology has been chosen as a central element in the DM research program conducted by a large consortium of researchers and organizations that joined together in the Global Argon Dark Matter Collaboration (GADMC). Building on the experience of previous experiments, the GADMC aims to integrate all experiments searching for WIMPs using argon-based detectors under a unified approach. The goal is to fully cover the spin-independent coupling WIMP hypothesis from $1\,\mathrm{GeV}/c^2$ up to hundreds of TeV/c^2.

The collaborations involved in GADMC are DarkSide, at INFN Laboratori Nazionali del Gran Sasso, Italy, ArDM at Laboratorio Subterraneo de Canfranc (LSC), in Spain, and, outside Europe, Mini-CLEAN and DEAP-3600 operated at SNOLAB in Canada.

In this Chapter, the properties of liquid argon are outlined alongside key scientific achievements and milestones of the GADMC program. The focus is on the search for low-mass WIMPs, presenting the argon ionization model and the analysis conducted by DarkSide on the data collected by DarkSide-50. The investigation of low-mass WIMPs is particularly intriguing, as the theoretical models and detection techniques need further study and data to be established, offering significant opportunities for new experiments, such as the Recoil Directionality (ReD) experiment within the GADMC, discussed in this thesis. Since the end of DarkSide-50 campaign, the GADMC has been going through a rich phase of innovation, research and design, with particular attention also to some studies that have provided interesting indications of a directional sensitivity effect on nuclear recoil in a LAr-TPC. Columnar recombination models suggest that the magnitude of the recombination should vary with the angle between the electric field and the direction of the ionization track. A difference in the electron-ion recombination effect is expected when the field and the track are either parallel or orthogonal.

To investigate the possibility of exploiting the process of columnar recombination in LAr to assess the directionality of a two-phase TPC with the ReD program [53].

Although initially designed with this scientific objective, ReD planned and conducted a second data-taking campaign in order to investigate the ionization response to nuclear recoils in the range of a few keV in a two-body-kinematic approach, since the literature is scarce in exploring this low-energy range.

2.1 Particle interaction in Liquid Argon

Once a particle interacts in LAr releasing energy, it originates excited Ar atoms and ionizes the medium, generating a light signal or electric charge respectively, as is shown schematically in Fig. 2.1.

Further scintillation light could be emitted by an ionization charge that undergoes a recombination process. In addition, a fraction of energy is lost as heat

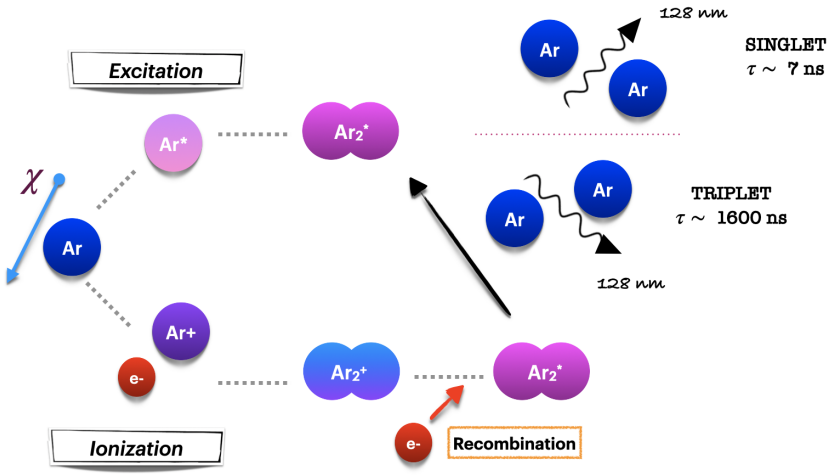

Figure 2.1: Pictorial scheme of processes in LAr. More details are provided in the text.

and it is not measurable. The interacting particle transfers its energy E_0 both to electrons and nuclei, according to Lindhard's theory [54, 55]. Considering these two contributions separately is reasonable because slow-moving atoms, recoiling after a primary interaction, are unable to excite electrons. Conversely, the energy transferred to the electrons can only return to the atoms gradually. The total deposited energy can be written as

$$E_0 = \eta + \nu \tag{2.1}$$

where η is the mean energy given to electrons and ν is the mean energy spent in nuclear recoil. The energy given to argon nuclei is either transferred to other nuclei, creating a series of nuclear recoils or dissipated as heat. In noble liquid detectors, signal formation is typically attributed to the electronic fraction of the deposited energy, which can be split into three distinct contributions linked to as many different physical mechanisms [56]:

$$\eta = N_i E_i + N_{\text{ex}} E_{\text{ex}} + N_i \epsilon \tag{2.2}$$

with E_i and E_{ex} as the mean energies spent to respectively ionize or excite an atom; ϵ is the sub-excitation energy for free electrons that goes into heat because it is lower than the excitation potential. These electrons can only elastically scatter atoms, increasing the temperature of the medium and this energy contribution can not be detected, thus it is lost. The mean number of ionized

and excited atoms are N_i and N_{ex} respectively, while N_h is the mean number of electrons with energy below the excitation potential. In the gas phase, the energy quantities in Eq. 2.2 can be referred to as the atomic ionization potential I= 15.75 eV. However, LAr exhibits a band structure in its electronic states resembling that of a solid, where the concept of ionization potential becomes less applicable. Consequently, energies are referred to as the band gap energy, E_g = 14.2 eV in Ar, allowing Eq. 2.2 to be reformulated as

$$\frac{\eta}{E_g} = N_i \frac{E_i}{E_g} + N_{\text{ex}} \frac{E_{\text{ex}}}{E_g} + N_i \frac{\epsilon}{E_g}. \tag{2.3}$$

Defining W' as the ratio of the deposited energy η over the number of ionized atoms it is possible to rewrite Eq. 2.3 as

$$\frac{W'}{E_g} = \frac{E_i}{E_g} + \frac{E_{\text{ex}}}{E_g} \cdot \frac{N_{\text{ex}}}{N_i} + \frac{\epsilon}{E_g}. \tag{2.4}$$

The ratio N_{ex}/N_i it is assumed to be ∼0.2 for electron recoils and ∼1 for nuclear recoils [57].

However, in a condensed medium, the recombination of charges along the particle tracks plays a crucial role. The observable ionization and scintillation signals depend on the possibly applied electric field. In the presence of an electric field in the detector, the phenomenon of recombination leads to a lower number of electrons collected with respect to N_i. This depends on both the ionizing particles properties and on the applied field itself. The fraction of electrons escaping recombination with the positive ions is higher for ERs than for NRs: electrons have low ionization density and the number of collected electrons is almost N_i already at a field of 1 kV/cm, while for particles with higher ionization density, it can be significantly smaller even at tens of kV/cm because of the dense structure of their tracks. Therefore, in the case of nuclear recoil, more energy is contributed to the scintillation signal than to the ionization signal, while the reverse is true for electrons: for which the fraction of electrons escaping recombination is higher.

2.1.1 Scintillation in liquid argon

Scintillation light is emitted by excited diatomic Ar molecules while decaying, and also electron-ion pairs, formed after ionization, can contribute to the scintillation light via the recombination effect. The result of both two cases is the

emission of a vacuum ultraviolet (VUV) photon with wavelength λ = 128 nm, thus requiring a wavelength shifter to be seen.

The two contributions differ in the excimers formation process:

- **Exitation luminescence process**: excited atoms (Ar^*) produced in the scattering process on Ar emit scintillation light through the reaction chain

$$Ar^* + Ar \rightarrow Ar_2^*$$

$$Ar_2^* \rightarrow Ar + Ar + h\nu$$

  with Ar_2^* the excited argon dimer.

- **Recombination luminescence process**: an argon ion Ar^+ and a neutral argon atom in the ground state bond together and give an argon molecular ion Ar_2^+

$$Ar^+ + Ar \rightarrow Ar_2^+$$

$$Ar_2^+ + e^- \rightarrow Ar^{**} + Ar$$

$$Ar^{**} \rightarrow Ar^* + heat$$

$$Ar^* + Ar \rightarrow Ar_2^*$$

$$Ar_2^* \rightarrow Ar + Ar + h\nu$$

where Ar_2^* is a highly excited argon atom. In their decay, the two excimers can populate either a singlet state or a triplet state that differs in the lifetime: the singlet state has a lifetime $\tau_s \sim 7$ ns, while the triplet has $\tau_t \sim 1.6$ µs. The particle that generates the interaction does not affect the lifetime values of the states, that are constant. What differs is the ratio of the population between singlet and triplet states that depends on the species of ionizing particles [58]. Therefore, from the time profile of the scintillation signal it is possible to discriminate the particles that induced electronic or nuclear recoil, i. e. perform the so-called *Pulse Shape Discrimination* (PSD) technique. Nuclear recoils events, that are elastic scattering WIMP-nucleus-like events, populate more singlet states than triplet states, and therefore show different behavior with respect to Electron recoils, that are due to events where β or γ particles interact with the electrons of the clouds of the Ar atoms. PSD in Ar is therefore a powerful tool to get rid of the background.

2.1.2 Ionization in liquid argon

In the process of ionization, free electrons and positive argon ions Ar^+ are created, which, in a few picoseconds, form molecular ions Ar_2^+. Meanwhile, electrons lose their energy both through inelastic and elastic collision: in the former type of collision, electrons give rise to further ionization and excitation, in the latter electrons generate heat by scattering on Ar atoms. The average energy spent to form an electron-ion pair is used to describe the ionization process; thus the ratio between the total deposited energy and the number of produced pairs can be defined as

$$W(E_0) = \frac{E_0}{N_i}, \tag{2.5}$$

while the ratio between the energy given to electrons and the number of produced pairs is

$$W'(\eta) = \frac{\eta}{N_i} \tag{2.6}$$

Considering relativistic particles, $E_0 \sim \eta$ and almost all the deposited energy goes to electrons, giving $W_{\text{rel}} \sim W'_{\text{rel}}$. On the other hand, for slow ions which generate nuclear recoils $W_{\text{NR}} = W'_{\text{NR}}(\nu + \eta)/\eta$; it is a reasonable approximation to suppose that $W'_{\text{rel}} = W'_{\text{NR}} = 23.6$ eV in LAr. This implies that the average energy required to create an electron-ion pair is independent of the type of primary particle interacting with the argon atoms, even though energy loss is influenced by the particle type. The difference in the number of pairs generated by slow ions and relativistic particles is solely due to the varying fraction of energy transferred to the electrons. However, due to the presence of impurities that capture electrons and the recombination process, it is not possible to measure these values as the number of electrons collected at an electrode does not reflect the number of pairs initially produced. As previously stated, recombination depends mainly on the type of particle that caused the ionisation and its kinematic conditions, since these two aspects determine the initial distribution of ions and electrons, as well as the strength of the applied electric field.

In conclusion, to detect the ionization signal, several conditions need to be fulfilled:

- charge carriers must avoid recombination

- they should exhibit high mobility within the electric field to reduce signal degradation and prevent capture by impurities
- the probability to form low mobility states along the drift path must be low
- a strong amplification mechanism is necessary to generate a detectable signal.

2.2 Signals in a LAr TPC

As schematically illustrated in Fig. 2.2, a dual-phase argon TPC consists of a bulk of LAr volume as the active target with a layer of the gaseous element in equilibrium on the liquid. The latter is known as *gas pocket* and could have a thickness of approximately one centimetre, while the liquid volume typically has a height of the order of the meter. The signal seen in the liquid target is due to the prompt scintillation light, and it is referred to as S1. Also, the light from electron-hole recombination contributes to the S1 signal, that is

$$\mathrm{S1} \propto N_{ph} = N_{ex} + f N_i \tag{2.7}$$

with N_{ph} the number of generated photons and f the fraction of ionized atoms N_i that recombine. Two conductive plates are positioned on the top (anode) and bottom (cathode) part of the detector and are kept to a fixed potential. Beneath the surface of the gas-liquid interface it is placed a metal or wire grid kept at a fixed voltage. Between the cathode and the grid is established the so-called *drift field* ($\mathscr{E}$) that allows electrons formed after ionization to escape recombination drifting from the interaction site to the top part of the detector. It is mandatory to keep this field as much uniform as possible, so the volume of the TPC is usually surrounded by copper rings to shape the field. Drifted electrons are extracted and accelerated by two stronger fields formed between the grid and the anode: the *extraction field* ($\mathscr{E}_{ex}$) is in the liquid phase, which extracts electrons in the gaseous phase, and the *electroluminescence field* ($\mathscr{E}_{el}$) which accelerates electrons in the gas and produces a secondary light, by electroluminescence (S2). This transition is generally energetically disadvantaged, but thanks to fields of the order of 2.5-3 kV/cm all electrons have on average enough kinetic energy to be directly extracted [59]. This signal is proportional

to the number of electrons and delayed in time with respect to the prompt scintillation signal. The TPC is equipped with arrays of light sensors on the top and bottom parts of the detector to measure S1 and S2 signals, also allowing to accurately spatially localize each event. Lateral diffusion along the drift path is negligible [59, 60], thus it is possible to establish the vertical position of the interaction inside the detector using the time difference between S2 and S1, while the light pattern seen by the photosensors on the upper part of the TPC gives the position on the (x, y) plane. In a dual-phase LAr TPC is thus possible to determine the position of energy deposits in liquid at the mm scale in the drift direction and ~ 1 cm or better in the two transverse directions, thus allowing the fiducialization within the detector and thus rejecting background events from the surfaces.

Measuring both scintillation light and ionization charge at the same time allows for improved energy resolution and gives the chance to distinguish between ER and NR. As mentioned, the long-lived triplet state is more likely to be present in ER, resulting in a longer scintillation time. A parameter that is calculated to exploit this different behavior and distinguish between WIMP and background events is f_{prompt}, defined as the fraction of prompt scintillation light in a fixed time window with respect to the total S1 signal.

The prompt window in DarkSide-50 was 90-ns long, so the parameter was

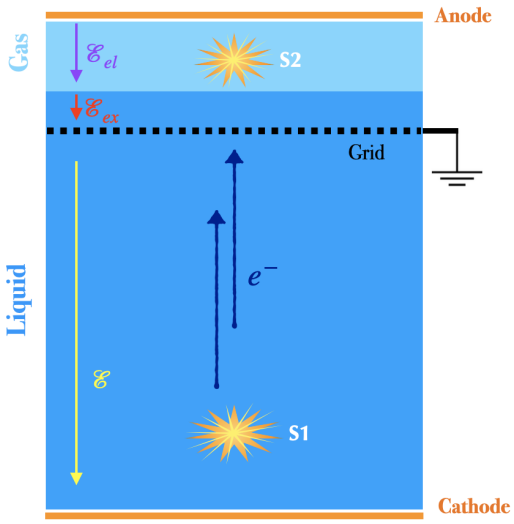

Figure 2.2: Sketch of a dual-phase argon TPC. More details in the text.

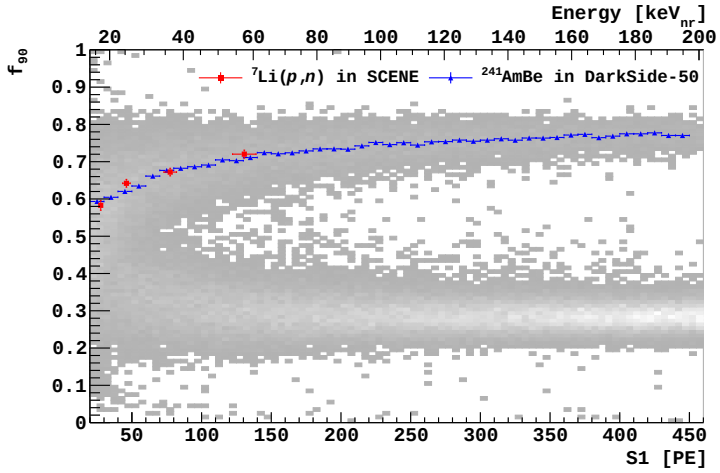

Figure 2.3: Ratio of the scintillation signal in the first 90 ns with respect to the total time window of the signal (f_{90} parameter) as a function of the scintillation signal. The two grey bands are well separated and the upper zone is due to neutrons from ^{241}Am-^{9}Be source (WIMP-like signals) while the lower one is due to background from γs and βs [61].

commonly known as f_{90} [48]

$$f_{90} = \frac{\int_0^{90\,\mathrm{ns}} \mathrm{S1}\,dt}{\int_0^{\mathrm{total}} \mathrm{S1}\,dt}. \tag{2.8}$$

Fig. 2.3 shows the f_{90} parameter as a function of S1: events populate two sufficiently separated bands, so it was possible to select NR events (upper band with f_{90} ~0.7) and discard ER events generated by β particles and γ-rays of background radioactivity (lower band with f_{90} ~0.3) [48].

2.3 Future plans to explore the DarkSide

The long-term program of GADMC will completely cover the the spin-independent WIMP hypothesis parameter space, reaching down to the theoretical lower limit for WIMP-like dark matter models that can be probed through direct detection experiments, commonly referred to as the *neutrino fog*. This term denotes the sensitivity threshold where dark matter signals become indistinguishable

from the background produced by neutrinos, making further detection challenging. The scientific program of the GADMC includes two new experiments. The near-future one is DarkSide-20k [62, 63], a dual-phase TPC that aims at a significant improvement in the sensitivity for direct detection of WIMPs, reaching $1.2 \times 10^{-47}\,\mathrm{cm}^2$ for WIMPs of $1\,\mathrm{TeV}/c^2$ mass. DarkSide-20k is proposed to achieve this result with an active (fiducial) mass of 23 t (20 t), for a total exposure of 100 t·yr to be accumulated in 5 yr.

The ultimate goal of GADMC will be the construction of the Argo detector, planned by the end of the next decade. This detector will have a fiducial mass of about 300 t to push the sensitivity deep in the region of the phase space where the irreducible neutrino background becomes not negligible.

For the success of these large future detectors, careful research into the radio-purity of materials to be used and a background check of the radioactive sources present in the argon used as a target is essential.

During its lifetime, in addition to achieving the electronic recoil background suppression with a power of $\sim 10^7$ using the pulse shape discrimination technique, DarkSide-50 achieved another milestone: the measurement of residual ^{39}Ar contamination in underground argon, ~3 orders of magnitude lower than atmospheric argon. This was possible since, after 2015, the atmospheric argon originally used in DarkSide-50 was replaced by argon with lower radioactive isotope contamination extracted from underground mines. Another step forward will be the use of depleted argon for future experiments, a project the DarkSide Collaboration has been working on for several years. The UAr programme of DarkSide, which will be presented next, is part of the broad program of research and technological innovation of the GADMC, which may also contribute to the provision of other experiments not related to the search for dark matter. Crucial for future experiments will also be the accurate simulation of the detector response to liquid argon scintillation, its ionization and electron-ion recombination processes, performed with `g4ds`, the Geant4-based Monte Carlo package developed within the collaboration [64].

2.3.1 Underground argon and the ARIA facility

Argon constitutes 0.934% of the volume of our atmosphere and exists in three isotopes: ^{40}Ar (99.604%), ^{38}Ar (0.063%) and ^{36}Ar (0.335%). This implies that its production on a commercial scale is not too expensive.

^{40}Ar is not a radioactive isotope, but exist also a trace amount of cosmologically activated radioactive isotopes of argon, including a small amount of ^{39}Ar, an unstable isotope which β-decays with an endpoint energy of 565 keV and a half-life of 269 years. Besides cosmogenic activation, ^{39}Ar may be generated in the subsurface environment by the neutron capture by ^{39}K or α emission from Ca. The concentration of ^{39}Ar is one part per trillion (ppt) in atmospheric argon (AAr), but although small, it becomes a source of background when trying to achieve the purity required to detect DM.

During the first two years of activity, DarkSide-50 was filled with AAr, and it was measured an ^{39}Ar activity of ~1 Bq/kg [65]. The trigger was primarily dominated by ^{39}Ar β-decays, and, at longer drift time (order of several hundred microseconds), it causes a large number of pile-up events. This overlap of events can complicate the identification and reconstruction of individual interactions, becoming a considerably bigger issue when dealing with larger detectors. Additionally, the abundance of ^{39}Ar events lowers the sensitivity of WIMP searches considering the leak of electronic recoil background in the nuclear recoil zone. To solve this problem the DarkSide Collaboration looked for cosmogenically protected argon in underground sites that has a lower concentration of ^{39}Ar. The search led to the Kinder Morgan Doe Canyon mine in Cortez, Colorado [66]. At Fermilab, this underground argon (UAr) was purified and isotopically distillated. The URANIA project therefore deals with the extraction of argon and its purification form CO_2.

In April 2015, the DarkSide-50 TPC was filled with ultra-pure UAr and, as shown in Fig. 2.4, the ^{39}Ar concentration was measured to be lower than AAr by a factor $(1.4 \pm 1.2) \times 10^3$ [61]. A further key component in the experimental program of the next-generation detectors of the GADMC is the UAr chemical purification step performed by the Aria facility [67]. Aria is a cryogenic distillation plant made of two columns, named Seruci-1 and Seruci-2, each measuring 350 m in height. It is installed in a mine shaft at Carbosulcis S.p.A., Nuraxi-Figus (SU), Italy. These columns are designed to further reduce the isotopic abundance of ^{39}Ar in the already ^{39}Ar-deplated argon. The method will also reduce the traces of N_2, O_2 and Kr to levels that are suitable for DM experiments [68]. Last, samples of argon baches from both URANIA and ARIA will be characterized by the DArT facility [69] at Canfranc to measure ^{39}Ar and identify potential problems before the insertion of the UAr in future DarkSide-20k.

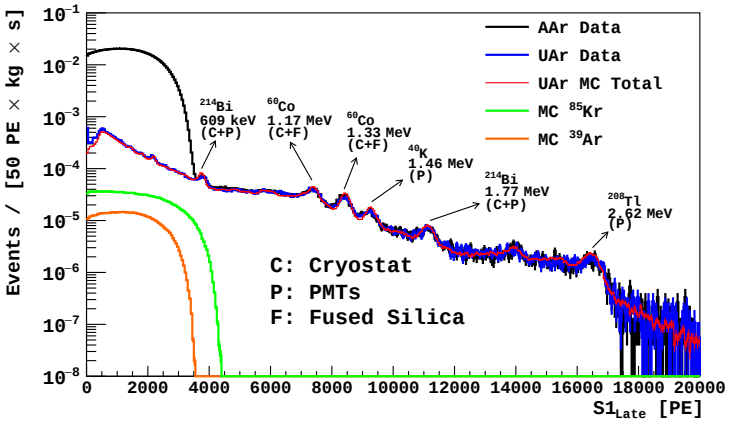

Figure 2.4: The measured field-off spectra for the UAr (blue) and AAr (black) targets are compared, with normalization to exposure. Also presented are the Monte Carlo fit to the UAr data (red) and the individual components of ^{85}Kr (green) and ^{39}Ar (orange) derived from the fit [61].

2.3.2 DarkSide-20k

The TPC of DarkSide-20k is shaped as a prism with an octagonal base, with a vertical dimension of about 348 cm and an octagonal inscribed circle diameter of 350 cm. The top and bottom lids of the octagon are made in pure acrylic and their inner planes are coated with a thin conductive material, Clevios^{TM}, and TPB as a wavelength shifter. The barrel pieces of the octagonal volume are machined and coated with Clevios to define a field cage of conductive rings connected by resistors and biased such as to define a uniform and stable drift field of 200 V/cm. The detector is surrounded by a stainless steel (SS) vessel filled with UAr, and the volume between the barrel and the vessel is sensitive itself and operated as an inner veto. Finally, the SS vessel is enclosed in a membrane cryostat, similar in design to the one developed for the DUNE experiment [70], where is immersed in an AAr bath. The total mass of UAr is 49.7 t (32.0 t inner veto), while the inner detector fiducial mass for the physics run is 20.2 t. The total AAr mass is about 600 t and will be used as Outer Veto for cosmic muons. The readout system for light signal is based on Silicon Photomultipliers (SiPMs) developed with Fondazione Bruno Kessler, Trento, Italy. The devices selected for DarkSide-20k have photo detection efficiency (PDE)

> 40% and dark count rate (DCR) < 0.01 Hz/mm^2 at 77 K (at 7 V overVoltage). Single SiPMs (8 mm × 12 mm) are grouped together to make a basic light collection unit, named Photon Detection Unit (PDU). 24 SiPMs are firstly ganged together in a (5 × 5) cm^2 tile, 16 tiles are in turn assembled into a (20 × 20) cm^2 PDU, each having four (10 × 10) cm^2 readout channels. Finally, 264 PDUs are installed in each optical plane, whereas 120 more, the so-called veto PDU, are installed on the outer surfaces of the barrel pieces and of the optical panels. It is particularly noteworthy that PDUs are produced mostly in-house by the Collaboration at Nuova Officina Assergi (NOA), a new INFN-LNGS facility. The experiment started the implementation phase and the external cryostat is being put in place in the Hall C at LNGS. The detector construction will follow, and the data taking is expected to start in late 2026. In addition, DarkSide-20k will also be sensitive to core-collapse supernova neutrinos (SN): 1.6 NR events are expected as a consequence of coherent scattering of SN after an exposure of 100 t·yr [71]. If this happens, DarkSide-20k will be one of the first experiments (with XENONnT [72]) to reach this important threshold.

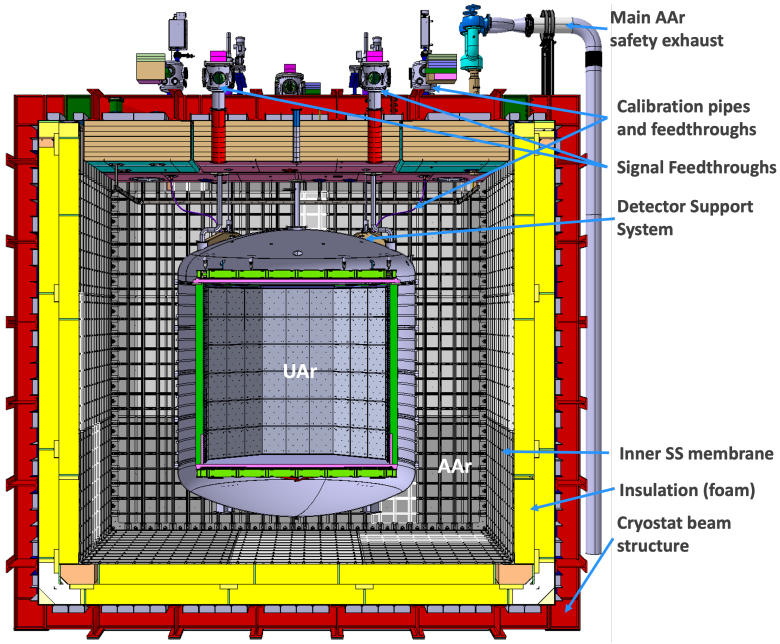

Figure 2.5: Current design of the DarkSide-20k detector, shown in section views. Inner detector and Inner veto, hosted in their SS vessel and, in turn, are hanging on the roof of the AAr cryostat, along with installed feed-throughs for support and signal extraction [73].

2.4 Liquid Argon to search low mass WIMPs

In 2018, DarkSide-50 broadened its research by also investigating the case of lighter dark matter particles. The search for a WIMP with masses of the order of $1\,\mathrm{GeV}/c^2$ is challenging because at the recoil energies that would occur, the S1 signal would be too small to be detected, and the only possible detection channel would be the ionization channel. Utilizing the ionization component enables exploration of the sub-keV energy range, reducing the energy threshold from approximately 20 keV_{nr} (nuclear recoil equivalent) to just a few hundred eV_{nr}. The drawback is the reduced background discrimination power due to the impossibility of using the PSD technique on the scintillation light and fiducialisation along the electric field, since the drift time is no longer measurable.

Nevertheless, DarkSide-50 set a 90% C.L. exclusion limit for SI cross section of $3\,\mathrm{GeV}/c^2$ mass WIMP on nucleon at $6\times10^{-43}\,\mathrm{cm}^2$. The analysis extends the exclusion region for SI DM interactions below the current experimental constraints in the $[1.2, 3.6]\ \mathrm{GeV}/c^2$ WIMP mass range [50]. This result was possible because the analysis was the result of a great deal of effort in the accurate determination of the LAr ionization response to nuclear and electronic recoils down to the sub-keV range. However, this energy range is still almost unexplored by experiments in a two-body kinematic approach that are crucial to constrain the fit analysis. If further investigated, the potential of a dual-phase LAr TPC technology in direct dark matter searches could be significantly enhanced.

DarkSide-50 measured the ionization response to ER down to $\sim$ 180 eV_{er} (electron recoil equivalent) by using β-decay of ^{37}Ar and ^{39}Ar from the 2013-2014 AAr campaign, acquired with the same drift field of 200 V/cm.

On the other hand, NR ionization response was measured down to $\sim$ 500 eV_{nr}, corresponding to $N_{e^-}=3$ ionization electrons, the lowest ever performed in argon, using *in situ* neutron calibration sources and external datasets from neutron beam experiment, coupled with detailed Monte Carlo simulations [74].

2.4.1 Electronic Recoil Ionization Yield

The ionization yield per unit of ER energy is defined as

$$Q_y^{\mathrm{ER}} = \frac{N_{i.e.}}{E_{er}} = \frac{(1-r)N_i}{E_{er}}, \tag{2.9}$$

where $N_{i.e.}$ is the number of ionization electrons escaping recombination, E_{er} is the rotated energy variable, and r is the electron recombination probability. The Thomas-Imel box model [75] predicts the value of r at low energies, $\mathcal{O}(\mathrm{keV}_{er})$

$$1 - r = \frac{1}{\gamma N_i}\ln(1+\gamma N_i), \tag{2.10}$$

where γ is a free parameter describing the recombination of the initial electron-ion pairs contained in a box and immersed in an electric field. This model is proven in noble liquids for short tracks [76] in the $\mathcal{O}(\mathrm{keV}_{er})$ range for ERs, where it is possible to parametrize Eq. 2.9 as

$$Q_y^{\mathrm{ER}} = \frac{1}{\gamma}\frac{\ln\left(1+\gamma\rho E_{er}\right)}{E_{er}}, \tag{2.11}$$

with γ the free parameter of the model expressed as the ratio between the parameter C_{box} and the drift field $\mathscr{E}$ (200 V/cm). C_{box} depends on the mean ionization electron velocity and on the size of the ideal box containing the electron-ion cloud. The parameter ρ is defined as N_i/E_{er}. In this parametrization, it is assumed the approximation of a constant excitation-to-ionization ratio (N_{ex}/N_i of 0.21 [77]) Thus having that N_i is proportional to the deposited energy as in [78] and ρ is parametrized as a constant.

DarkSide-50 used ^{37}Ar and ^{39}Ar data, selecting events in the TPC within a central cylinder volume with 2 cm radius and 21.6 cm height, 16.8 cm far from the lateral walls and 7 cm from the top and bottom of the TPC, to remove the external contamination due to radioactivity in detector materials surrounding the active mass. In addition, multiple scattering events, i.e. events with more than one S2 pulse, were rejected as not compatible with the topology of the ^{39}Ar β-decay signature. The rotated energy variable leverages the full anticorrelation between S1 and S2 signals to reconstruct the kinetic energy of each event

$$E_{er} = w\left(\frac{\mathrm{S1}}{g_1} + \frac{\mathrm{S2}}{g_2}\right). \tag{2.12}$$

In Eq. 2.12, w is the average energy required to produce a quantum (excitation or ionization) and its value is 19.5 ± 1.0 eV [57]; g_1 is the S1 collection efficiency (0.16 ± 0.01 [78]) and g_2 is the measured S2 yield, defined as the mean number of photoelectron per ionization electron extracted in the gas pocket, and the

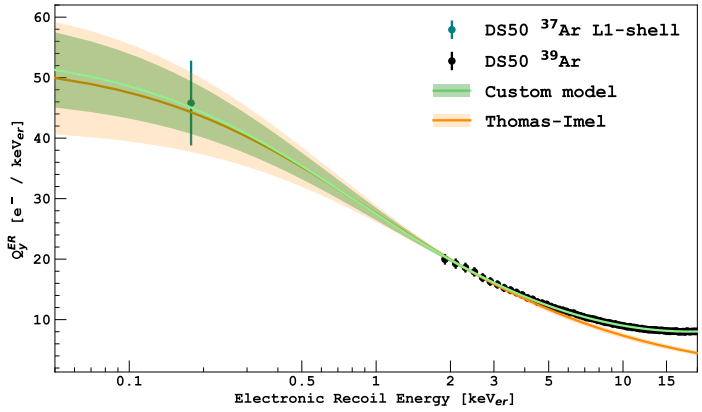

Figure 2.6: Fit of the ER ionization yield measured from β-decay of ^{39}Ar (black) and ^{37}Ar (teal) in a 200 V/cm drift field. The fit is done with the Thomas-Imel box model up to 3 keV$_{er}$, while the extended version of the model [Eq. 2.14] is used up to 20 keV$_{er}$. The model bands correspond to 1 σ with the correlation from the g_2 systematic included [74].

associated relatives resolution are 23 ± 1 PE/e^- and ~ 27% [79]. For each event of the ^{39}Ar sample $N_{i.e.}$ and calculated as

$$N_{i.e.} = \frac{\mathrm{S2}}{g_2} - 1, \tag{2.13}$$

which accounts for the subtraction of the primary electron from the β-decay. Using Eqs. 2.12 and 2.13 for each 0.2 keV$_{er}$ bin it is possible to estimate the mean value of the ER ionization yield, Q_y^{ER}. A lower threshold of $E_{er} > 1.7$ keV is applied to guarantee 100% efficiency in the identification of the S1 pulse. The uncertainty is dominated by the systematics from the g_2 parameter. Eq. 2.11 is used to fit ^{39}Ar data, ^{37}Ar line included, up to 3 keV$_{er}$.

The Thomas Imel box model agrees with points at $E_{er} < 3$ keV$_{er}$, as it is shown in Fig. 2.6. The empirical Doke-Birks parametrization [77] allows for extending the Thomas-Imel model in the 3-20 keV$_{er}$ range, however, a lack of compatibility appears with the ^{39}Ar data in the range. The agreement with the data is recovered in the entire range by adding a custom term with two free

parameters, p_0 and p_1, to Eq. 2.11 that becomes

$$Q_y^{\mathrm{ER}} = \left(\frac{1}{\gamma} + p_0\left(E_{er}/\mathrm{keV}_{er}\right)^{p_1}\right)\frac{\ln\left(1+\gamma\rho E_{er}\right)}{E_{er}}, \tag{2.14}$$

More details about the measurement can be found in [74], what it is important to highlight is that the extrapolation of the ER ionization yield below the 179 eV_{er} from the ^{37}Ar L1-shell electron is weakly dependent on the custom term introduced in Eq. 2.14 as it is mainly driven by the Thomas-Imel box model.

2.4.2 Nuclear Recoil Ionization Yield

In analogy with the ER ionization yield in Eq. 2.9, the NR ionization yield Q_y^{NR} is formalized as

$$Q_y^{\mathrm{NR}} = \frac{N_{i.e.}}{E_{nr}} = \frac{(1-r)N_i}{E_{nr}}, \tag{2.15}$$

where the electron recombination probability r is described by the Thomas-Imel model in Eq. 2.10. Assuming that the excitation to ionization ratio is constant, Ni can be expressed [80] as follows

$$N_i = \beta\,\kappa(\epsilon) \;=\; \beta\,\frac{\epsilon\; s_e(\epsilon)}{s_n(\epsilon)+s_e(\epsilon)} \tag{2.16}$$

with β in a normalization constant that plays the role of the second parameter of the model together with C_{box}. The energy lost in electronic excitation giving rise to ionization and scintillation signals is the dimensionless parameter κ; s_e is the rate at which electrons are excited by inelastic collisions, and s_n is the rate at which energy is transferred to recoiling nuclei by elastic collisions. They all depend on the dimensionless parameter ϵ, which is given by

$$\epsilon = \frac{a}{2e^2Z^2}\,E_{nr}/\mathrm{keV} \;\simeq\; 0.0135\,E_{nr}/\mathrm{keV} \tag{2.17}$$

with $a = 0.626\cdot a_0\cdot Z^{-1/3}$ [80] which is the Thomas-Fermi screening length with $a_0 = \hbar/(\alpha m_e c) \simeq 0.529\cdot 10^5$ fm. As in [80], the stopping power s_e can be expressed as

$$s_e(\epsilon) = \frac{0.133\;Z^{2/3}}{A^{1/2}}\,F(v/v_0)\,\sqrt{\epsilon} \simeq 0.145F(v/v_0)\sqrt{\epsilon}. \tag{2.18}$$

The correction factor $F(v/v_0)$ depends on the nuclear (v) and Bohr ($v_0 = e^2/\hbar$) velocities and it is assumed equal to 1. As in Ref. [80], an *ad hoc* function is defined to test the sensitivity of the calibration data to a potential suppression of $s_e(\epsilon)$ at low energies. The nuclear stopping power s_n is modeled by Ziegler *et al.* [81] employing an universal screening function:

$$s_n(\epsilon) = \frac{\ln(1+1.1383 f_Z \epsilon)}{2[f_Z \epsilon + 0.01321(f_Z \epsilon)^{0.21226} + 0.19593(f_Z \epsilon)^{0.5}]}. \tag{2.19}$$

f_Z is a conversion factor for argon: it is ≃0.953 and accounts for the slightly different dimensionless energy definition in [81] compared to Eq. 2.17.

Results of the model calibration

When studying the ionization response of argon in [79], the DarkSide Collaboration considered two extreme model areas: on the one hand, one model allows for fluctuations in energy quenching, ionization yield and recombination processes obtained with a binomial distribution, on the other hand, the other model set all the fluctuation in energy quenching to zero.

The analysis described in [74] considers the model without quenching fluctuation as it is not possible to distinguish between the two possible scenarios since the difference in the results is negligible. The model from Eq. 2.15 is constrained both by fitting DarkSide-50 calibration data, collected during the UAr campaign by using ^{241}Am-^{13}C and ^{241}Am-^{9}Be neutron sources [82], and by simulated events, following a method similar to that described for ERs in Sec. 2.4.1. In addition, external datasets from small-scale LAr detectors exposed to neutron beams are used to further constrain the LAr response to ionization signals. The ionization yield values measured by SCENE [83], ARIS [84] and Joshi *et al.* [85] are the only available in the literature.

The SCENE experiment has a drift field of 193 V/cm, really close to the DarkSide-50 one, and it measured the ionization yield at four NR energies from 16.9 to 57.3 keV, with g_2 = 3.1±0.3 PE/e^-. The differences in fields are assumed negligible and the SCENE results are normalized to the DarkSide-50 response by the ratio between their g_2 values.

The ARIS collaboration characterized the response at 200 V/cm for eight NR energies in the range between 7.1 and 117.8 keV. The ratio between S1 yields of DarkSide-50 (8.0±0.1 PE/keV) and ARIS (6.35±0.05 PE/keV) at the null field is used to rescale the ARIS field-on data to DarkSide-50 ones.

Joshi *et al.* have measured the ionization yield for NRs at 6.7 keV, the current lower energy value in LAr, using the end point of a spectrum induced by a monochromatic neutron beam (70 keV). The measurement is obtained at a 240 V/cm field, so the experimental point has been corrected for their single electron yield using the 2.82 keV K-shell capture ^{37}Ar line from their experiment and DarkSide-50 as a cross-calibration point. The corrected value for the NR ionization yield is Q_y=6.0$^{+0.8}_{-1.8}$ e$^-$/keV and it is just quoted in the comparison of the final result shown in Fig. 2.7.

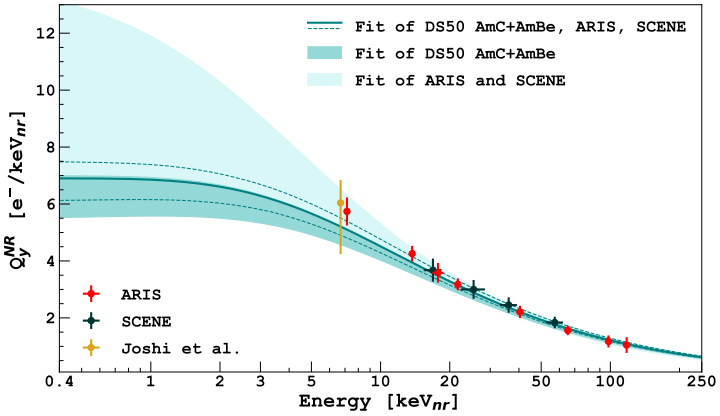

Figure 2.7: NR ionization yield at a 200 V/cm field as a function of the nuclear recoil energy. The Fit comes from the combined fit of DarkSide-50 ^{241}Am-^{13}C and ^{241}Am-^{9}Be calibration data toghether with the external dataset from SCENE [83] and ARIS [84]. The measured Q_y^{NR} by Joshi *et al.* [85] at 6.7 keV$_{nr}$ is reported for comparison. The model bands correspond to 1 σ uncertainty[74].

In conclusion, the sensitivity of the DarkSide-50 data to different models of the nuclear-stopping power as a function of energy, resulting from different assumptions about the screening effects of atomic electrons, has been investigated [74]. Fig. 2.8 shows the Q_y^{NR} obtained from the fit using the different screening function. It is possible to note that among the tested models in [74], the one by Ziegler *et al.* is the one that leads to the lowest Q_y^{NR} in the region of interest for the WIMP searches. Therefore DarkSide adopted this model as a results in the more conservative choice for for the sensitivity to WIMPs.

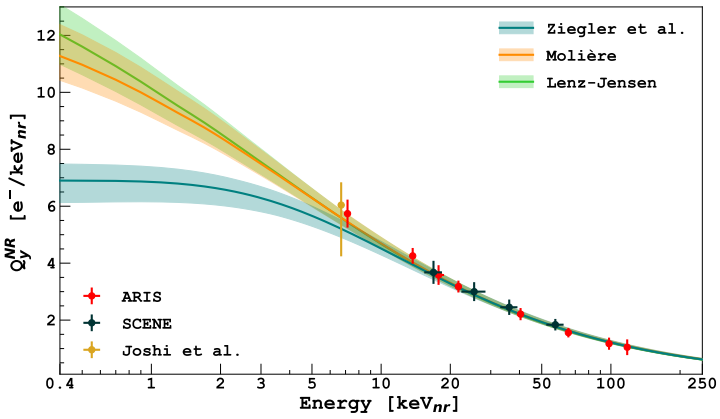

Figure 2.8: Fit of DarkSide-50 ^{241}Am-^{13}C and ^{241}Am-^{9}Be data, and ARIS and SCENE datasets using Ziegler *et al.* (Eq. 2.19) [81], Molière [86], and Lenz-Jensen [87, 88] screening functions. The model bands correspond to 1σ uncertainty.[74].

Chapter 3

The Recoil Directionality (ReD) Experiment

As proved by DarkSide-50, LAr TPCs are currently one of the leading technologies for probing a broad spectrum of DM masses, including the search for light WIMPs with masses of less than 10 GeV/c^2. The previous Chapter discussed the properties of liquid argon, emphasizing how the measured ionization yields for both electron recoils and nuclear recoils will influence direct searches for light WIMPs using the ionization component only.

The response model of argon developed by DarkSide-50 in [50] could be further enhanced through a deeper investigation of the ionization quenching effect. Beyond the fluctuations caused by exciton and ionization electron splitting and ion-electron recombination, quenching also introduces fluctuations that, at such low energies, can increase the probability of detecting events above the analysis threshold.

When considering two scenarios, one where quenching fluctuations are present (QF) and one where they are absent (NQ), the latter scenario has been chosen in [50]. Although not physically accurate, this conservative choice better supports the modeling of WIMP searches. In the QF scenario, fluctuations are assumed to be governed by a binomial statistic between ionization electrons and excitons, which are detectable, and the undetected heat contribution due to phonon. Fig. 3.1 shows the exclusion limits above 1.2 GeV/c^2 obtained by DarkSide-50 for both NQ and QF cases compared to existing 90% C.L. exclusion limits and claimed discovery. Reported in grey is also the LAr neutrino fog.

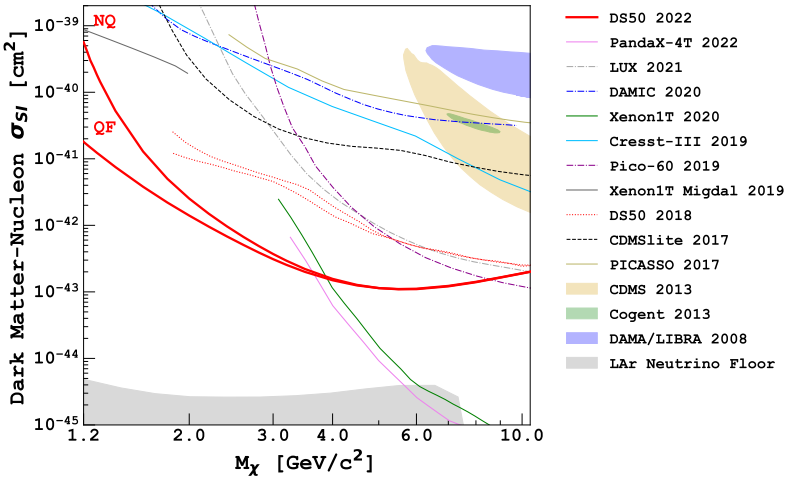

Figure 3.1: The plot shows the comparison between DarkSide-50 limits to the 90% C.L. exclusion limits and claimed discovery from Refs.[37, 79, 89–100]. The two scenarios for quenching fluctuations (NQ vs. QF) are reported. The comparison to the neutrino fog for LAr experiments [101] is shown in grey [50].

Future improvements in the limits by DarkSide-50 could be achieved by better characterizing the ionization response of liquid argon and refining the stochastic model that governs NR quenching. To this end, dedicated measurement campaigns using setups exposed to neutron beams in a two-body kinematics approach are necessary.

The Recoil Directionality (ReD) experiment, part of the GADMC, has carried out a focused measurement campaign with its LAr TPC to characterize the response of liquid argon to nuclear recoils below 5 keV, a region that was unexplored for LAr. Beginning in 2021, the ReD group commissioned the elements of this campaign at the INFN Sezione of Catania, where the experiment was conducted until March 2023, when the data collection phase concluded. In this Chapter, I will describe the ReD experiment, detailing the components of the apparatus, the data collection strategies employed, and concluding with the performance achieved and preliminary results obtained.

3.1 Conceptual design of low-energy recoils campaign with ReD

The goal of the ReD experiment is to collect a dataset of nuclear recoil events in the energy range of 2 to 5 keV and to correlate these events with the corresponding electroluminescence signal S2 of the drifting ionization electrons. The experimental setup has been conceived to achieve this objective. The LAr TPC of ReD has a small volume of approximately 150 cm^3. It was designed as a benchmark for technologies to be implemented in the DarkSide-20k experiment, notably the readout system. Specifically, ReD was the first LAr TPC equipped with cryogenic Silicon Photomultipliers (SiPMs) as the readout system.

The TPC is irradiated with neutrons produced in spontaneous fission events by a ^{252}Cf source. Such neutrons interact with liquid argon nuclei via elastic scattering (n,n'), giving NRs of energy E_R. Two-body kinematics is used to determine the recoil energy value, with the formula adapted from Eq. 1.5:

$$E_R = 2E_n \frac{m_n m_{Ar}}{(m_n + m_{Ar})^2}(1 - \cos\theta_s), \tag{3.1}$$

where m_n and m_{Ar} refer to the masses for the neutron and the Ar respectively, θ_s is the scattering angle and E_n is the kinetic energy of the neutron. To define the energy range for nuclear recoils, 18 plastic scintillators, referred to as Pscis hereafter, are positioned in a downstream neutron spectrometer to detect these particles as they scatter.

Neutrons emitted from ^{252}Cf have a continuous energy spectrum ranging from 0 to 10 MeV, rather than being monochromatic. Therefore, Time of Flight (ToF) measurements are necessary to determine their energy E_n. While the Pscis in the spectrometer provide the stop signal for the neutron flight, an additional signal is required to mark its start, coinciding with the fission event. For this purpose, two barium fluoride (BaF_2) detectors, each paired with a photomultiplier tube (PMT), are used to detect fission events and initiate the neutron flight timing. BaF_2detectors and Pscis work as tagger detectors, recording the ToF of neutrons over a fixed distance. Once the kinematics have been closed and the neutron energy determined from the ToF measurements, the recoil energy can be calculated based purely on kinematic principles. These calculated recoil energies are then correlated with the signals detected by the SiPMs in the TPC. At low recoil energy values, such as those targeted in these measure-

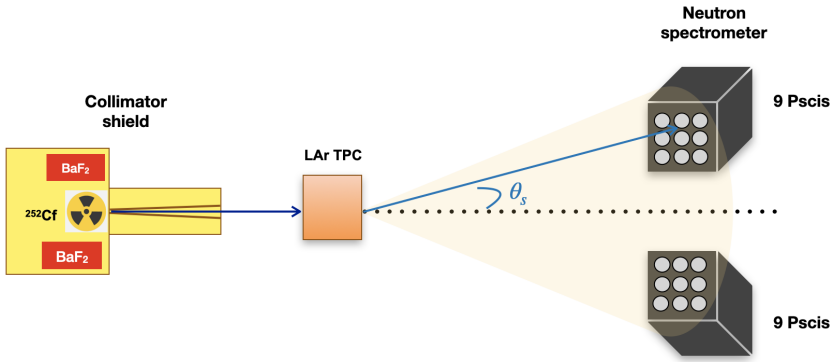

Figure 3.2: Illustration of the ReD geometrical scheme at INFN-Sezione of Catania. On the left, in yellow, is the collimator shield, where the ^{252}Cf source and the two BaF_2 are hosted. The blue arrow stands for the path traveled by the neutron before scattering elastically inside the TPC, the cyan one is the possible path of the outgoing neutron n' within the solid angle seen by the neutron spectrometer.

ments, the S1 scintillation signal is often difficult to detect. Therefore, the only expected signal is a single S2 pulse from the scattering.

3.2 The experimental setup

Now that the idea behind the experiment has been described, it is time to examine the ingredients that are necessary for the implementation of the experiment. Fig. 3.2 shows a schematic representation of the experimental setup of ReD in this campaign. Shown on the left, in yellow, is the structure that contains the ^{252}Cf source. It serves a dual purpose: to host and collimate the neutrons emitted by the source toward the TPC and to absorb the emitted particles, ensuring a safe laboratory environment. Deployed close to the source are the two BaF_2 crystals. The LAr TPC, along with its ancillary cryogenic system for argon liquefaction and recirculation (not shown in the illustration), is positioned in the central part of the schema. On the right side is the neutron spectrometer, which features Pscis arranged in two 3×3 matrices. All components are arranged and aligned according to a precise geometry to close the kinematic. A detailed description of each element follows.

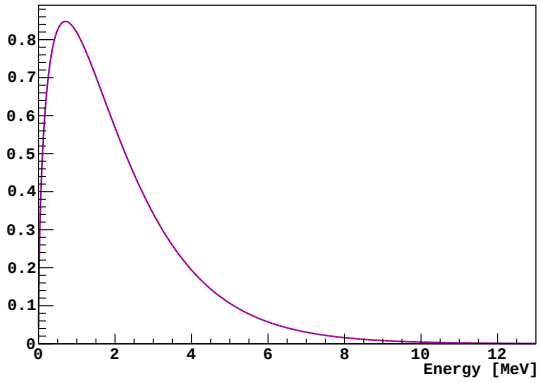

Figure 3.3: Energy spectrum of neutrons emitted by ^{252}Cf .

3.2.1 Inside the shield: source and BaF_2 detectors

^{252}Cf is a strong neutron emitter: it decays by α-emission to ^{248}Cm, with a branching ratio of 96.9%, and by spontaneous fission (SF) for the other 3.1% [102]. One µg of ^{252}Cf emits 2.3 million neutrons per second, an average of 3.7 neutrons per spontaneous fission [103]. The energy spectrum for fission neutrons from ^{252}Cf is continuous up to about 10 MeV and, as shown in Fig. 3.3, has a Maxwellian shape: it exhibits a most probable value of 1 MeV while its mean value is of 2-3 MeV [102]. The source used in the ReD campaign has an activity of about 1.0 MBq, resulting in an activity for SF of ~ 26 kBq.

For radiation protection, the source is enclosed in a cubic shield composed of three layers of boron-loaded high-density polyethylene (HDPE), each with a thickness of 5 cm. The borated HDPE is effective for moderating neutrons, except for a channel that permits neutron escape. This channel, located on one face of the box, consists of 10 layers of the same boron-loaded HDPE, drilled to form a 2° exit cone directing neutrons towards the LAr TPC, which is positioned 90 cm from the source. Additionally, the entire collimator shield is further protected by a 4-mm lead foil and 1 cm of iron to attenuate γ-rays from fission events and secondary radiation resulting from neutron moderation and capture. Fig. 3.6 illustrates the design of the shield and its final construction. A custom boron-loaded HDPE structure is placed inside the shield to secure the source. The holder has a slot that positions the source directly at the exit hole of the cone. Adjacent to the slot, two small blocks are incorporated to align

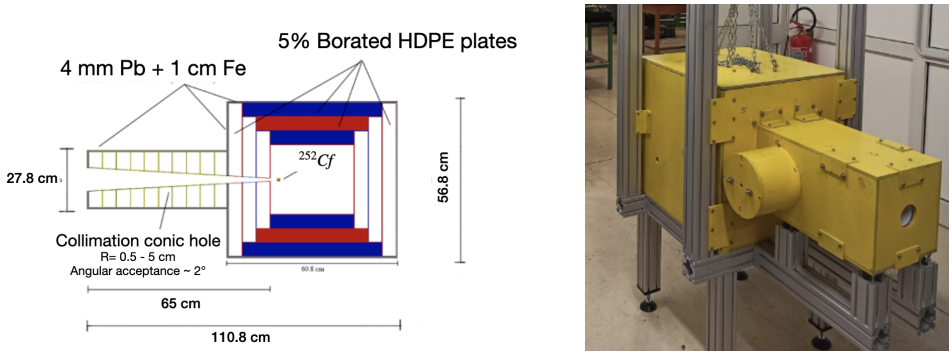

(a) (b)

Figure 3.6: The collimator shield: **(a)** vertical section of the design and **(b)** picture of the facility.

the two BaF_2 detectors at the same height as the source, allowing placement on both the left and right sides.

As a scintillator, barium fluoride is particularly suited in applications where both high detection efficiency per unit volume and a fast response are required. The scintillation light emitted by BaF_2 consists of two components: a fast component, with a decay time of 0.6 ns emitted in the short wavelength region of the spectrum, and a slower component with 630 ns decay time at somewhat longer wavelengths. Two cubic BaF_2 crystals, each with a 3 cm side, are used to detect the γ radiation associated with SF events. Each crystal is coupled to a HAMAMATSU H11934 series PMT. One of these PMTs is specially designed to be highly sensitive in the UV region, which enhances the detection of the fast component of the scintillation light for one of the two BaF_2. To maximize the light collection the crystals have been wrapped with teflon and aluminum tape and adhered to the PMT sensor via a layer of optical grease (see Fig. 3.9). Then, the BaF_2 crystals are further covered with black tape and protected from delayed γ-rays from thermal neutron capture by a Pb foil shaped to cover the faces that are not directly exposed to the source. A picture of the prepared setup inside the shield is shown in Fig. 3.10.

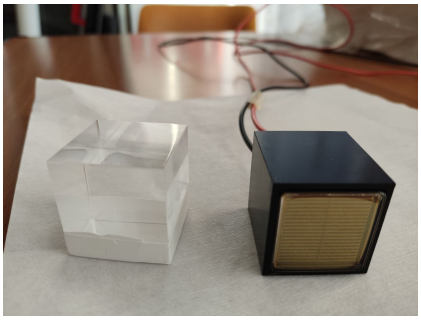

(a)

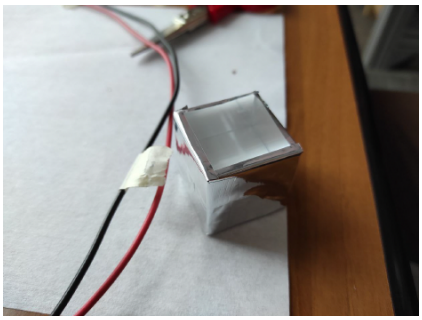

(b)

Figure 3.9: **(a)** One of the cubic BaF_2 crystals and its PMT. **(b)** Each scintillating crystal is carefully prepared to maximize light gathering.

Figure 3.10: Hosted in the center of the shield, right in front of the hole corresponding to the vertex of the exit cone are placed the ^{252}Cf source and the deployed tagger scintillators.

3.2.2 The TPC of ReD

The heart of the ReD experiment is its LAr TPC, designed and realized by the University of California Los Angeles (UCLA) DarkSide group. A detailed picture of the TPC is shown in Fig. 3.11. The geometry chosen is that of a square-section volume of 5 cm (length) × 5 cm (width) × 6 cm (height). The inner volume is delimited by two 4.5 mm thick acrylic windows, one at the top and the other at the bottom, and by a reflecting sandwich-style acrylic structure on the four walls. This consists of two acrylic plates of 1.5 mm thickness with a 3M Enhanced Specular Reflector film (3M™ESR) in between that enhances the light amount inside the detector. The two windows are coated with a 25 nm thick conductive layer of Tin-Indium-Oxide (ITO) as in the DarkSide-50 detector, to operate them as anode and cathode for the electric field formation. Inside the active volume of the TPC, at a distance of about 1 cm from the anode window, there is the 50 µm thick stainless steel etched mesh made by hexagon cells with a 95% transparency.

The gas pocket is generated using a bubbler, which employs a PT-1000 resistor to boil the liquid argon. The resulting gas is channeled through a teflon inlet tube into the *diving-bell*, a narrow region within the detector between the external PTFE frame and the active volume. From there, the gas enters the active volume of the detector. The diving-bell has a hole that acts as an overfull and fixes mechanically the height of the gas pocket at 7 mm. In the double phase configuration, the TPC has a 5 cm maximum drift length, that is the distance between the grid and the cathode, a 3 mm thick layer of liquid argon above the grid that in the standard configuration operates at a 0 voltage potential, and finally a 7 mm thick gas layer. Both windows and all around the walls of the TPC are evaporated with a layer of TPB wavelength shifter. This is necessary to convert VUV photons emitted by argon into the visible range, and make them detectable by optical sensors. The coating thickness can vary from about 160 µg/cm^2 to about 200 µg/cm^2.

In the data-acquisition configuration, the three fields established inside the TPC have the following values: $\mathscr{E}$ of about 200 V/cm, $\mathscr{E}_{ex}$ of 3.8 kV/cm in the liquid argon, and $\mathscr{E}_{el}$ of 5.7 kV/cm in the gas region.

Finally, the PTFE supporting structure of the TPC is hanged to the cryostat main flange by the use of four threaded rods (Fig. 3.11) [53]. The ReD TPC was commissioned and characterized in 2019 at the INFN “CryoLab” at the Uni-

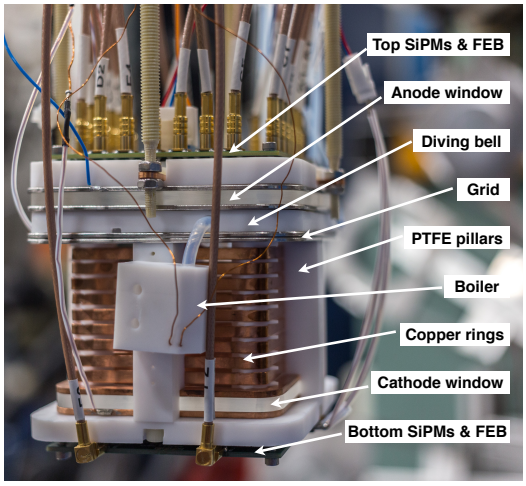

Figure 3.11: A picture of ReD LAr TPC with all its elements. It is possible to note its teflon pillar structure, the field cage (copper rings that provide a homogeneous electric field), and the bubbler with the gas inlet tube that provide the formation of the gas pocket [53]. Further details in the text.

versity of Naples Federico II, and was operated continuously for 165 days [53] proving the stability of the readout system.

The ReD Optical Readout

Unlike the DarkSide-50 predecessor, DarkSide-20k will be equipped with new generation SiPMs. Therefore, the ReD TPC is the first TPC equipped with this optical readout, in order to test its performance.

SiPMs are constituted by several Single Photon Avalanche Diodes (SPADs) that, connected together in parallel, work in Geiger mode, i.e. every time a photon generates an electron/hole pair, they are drifted by an electric field in the multiplication region where they induce an avalanche. The voltage at which the avalanche is triggered is the *breakdown voltage* V_{bd} [104]. So, usually SPADs work a few volts above this threshold value:

$$V_{bias} = V_{bd} + V_{ov} \tag{3.2}$$

where V_{ov} is the so-called *overvoltage* value. Since the discharge is self-sustaining, a quenching resistance is placed in series with every single SPAD so that, after the discharge phase, the diode recharges in order to be ready for the detection

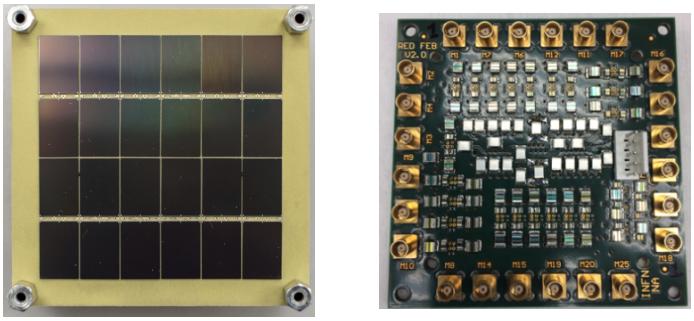

(a) (b)

Figure 3.14: **(a)** Front view of a NUV-HD-Cryo SiPM tiles. It has a rectangular shape and it is made of 24 SiPMs bounded together by several micro-length wires. **(b)** Front-End Board (FEB) with 24 channels read-out [53].

of a new signal. Basically, a SPAD is a binary device, so it is common in the application to group thousands of them to have a SiPM of a few millimeters.

Compared with standard PMTs, SiPMs have also higher gain (in a range between 10^5 and 10^7) and better Photon Detection Efficiency (PDE). PDE is defined as:

$$PDE = QE \times \mathscr{P} \times \epsilon_{geom} \tag{3.3}$$

with QE quantum efficiency, i.e. the probability for an incident photon to generate an electron-hole pair, $\mathscr{P}$ the generating avalanche probability and ϵ_{geom} the geometrical efficiency of the device. PDE increases also with the increasing of over-voltage bias [104].

The ReD LAr TPC uses customised NUV-HD-Cryo SiPMs with maximum PDE at about 420 nm in the near UV region of the electromagnetic spectrum. The SiPMs are made especially for the DarkSide project by *Fondazione Bruno Kessler* (FBK) in Trento, Italy, and they have triple doping concentration together with a 25 µm cell pitch and a 10 MΩ quenching resistance at cryogenic temperature. Each SiPM has a rectangular shape of 11.7 mm × 7.9 mm and it is assembled onto a 5 cm × 5 cm tile with 24 devices. Thus, the ReD TPC is equipped with two tiles: one placed at the top and one at the bottom, each behind its respective acrylic window. The Front-End Boards (FEBs) used for the output read-out in ReD supply power to the photosensors and amplify the output signals at cryogenic temperature. Each SiPM is operated at a fixed V_{bias}

of 34 V, corresponding to V_{ov} = 7 V with respect to the breakdown voltage V_{bd} [53]. Fig. 3.14 (a) and Fig. 3.14 (b) display the NUV-HD-Cryo SiPMs, positioned at the top and bottom of the TPC, and the Front-End Board (FEB) responsible for the electronic readout, respectively. FEBs are amplified with an independent low-noise Transimpedance Amplifier (TIA) developed especially to assure optimal performance of the device at the working temperature of ~ 87 K.

They are coupled directly to the tiles and, depending on whether they are coupled to the top or bottom tile, have differences in the readout scheme. The bottom tile is arranged in order to assemble the SiPMs in four groups each made by six SiPMs (three branches with two SiPMs in series), coupled in series and then summed in parallel. The output read-out is made of a four-channel FEB realized at INFN - LNGS and was used at the V_{bias} of 68 V (2 × 34 V). In fact, 34 V are distributed to each of the three branches and the six SiPM signals are summed and amplified, giving a total of four output channels.

On the other hand, the top tile has a single-SiPM read-out in order to improve the $x-y$ resolution on the ionization signal. In this case, the SiPM matrix is coupled with a 24-channel FEB read-out designed and realized by the INFN - Napoli in collaboration with INFN - LNGS and INFN - Bologna groups of the DarkSide collaboration. Therefore, the FEB on the top manages each SiPM independently, both as regards the distribution of the common bias voltage to the 24 devices, and for the reading and amplification of the signals. As shown in Fig. 3.14 (b), it has 24 MCX connectors for cabling each single SiPM of the tile. The SiPMs are biased via a CAEN SY 5527 power supply module, while signals are acquired, digitized and stored in a CAEN V1730 Flash ADC board with 16 channels for the total of 28 channels needed.

Signals from the SiPMs have a fast rise, of the order of a few nanoseconds, followed by a slower tail, of the order of 1 µs, depending on the recharge time of the devices. An example of a waveform seen by one SiPM in a dual-phase mode run is shown in Fig. 3.15. The waveform length can be selected from 80 to 120 µs. This time interval is chosen to account for the maximum drift time in the TPC, which is about 65 µs, and to ensure that the S2 signal is also recorded in the event.

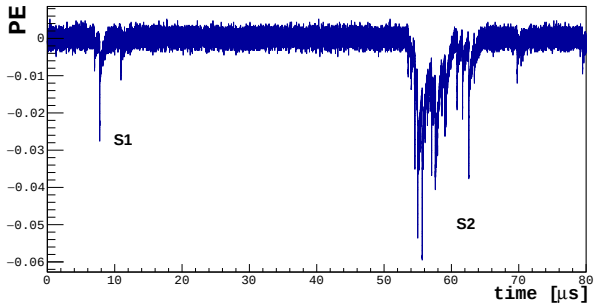

Figure 3.15: Example of a waveform registered by a SiPM in a double-phase mode. It shows both scintillation (S1) and ionization (S2) signals captured.

The Cryogenic System

To ensure that the system is at the cryogenic temperatures, necessary to work with a material such as argon, the TPC is equipped with a cryogenic system. This system, developed by the Criotec company in Chiavasso, allows both the liquefaction of commercial gas argon, and its recirculation inside the system, together with the purification. To facilitate placement and movement, this cryogenic system, complete with electronics and electrical connections, is fully deployed in a cart.

According to the scheme shown in Fig. 3.16, during the filling phase, the argon gas from a commercial bottle is pushed into the system. By a Mass Flow Controller (MFC), it reaches the condenser where it is cooled down by the presence of a copper cold head. Then, the gas enters the dewar where the ReD TPC is located: continuous circulation of gas argon with increasingly lower temperature together with the cooldown of all mechanical components allows for the liquefaction of argon.

The dewar is a double-wall container that hosts the TPC and the liquid argon. It has a conical shape and its internal diameter varies from about 13 cm at the bottom to about 25 cm at the top, where it is closed by a CF250 flange. For the purposes of the experiment, about 30 cm of LAr are produced inside the dewar, a level that in standard conditions is reached in about 12 hours of continuous cooling down. The filling procedure of the dewar with LAr is monitored thanks to 4 PT-100 RTDs sensors positioned at different levels within the cryostat.

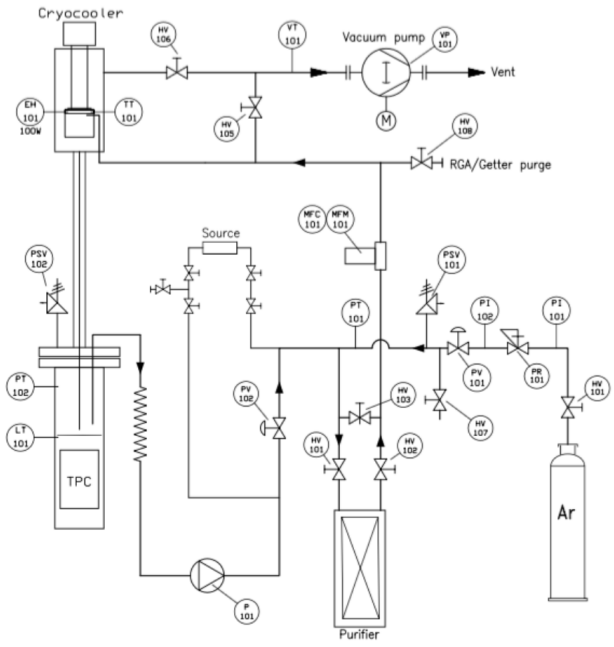

Figure 3.16: Drawing of the ReD cryogenic system. Argon gas from a commercial bottle is pushed inside the condenser where liquid is produced by means of a cold head connected to a cryocooler. Liquid argon then drops inside the cryostat, which contains the TPC. During a regular data taking phase, the pump P101 on the bottom of the drawing provides recirculation of the gas through the purifier, and once again to the condenser, in a continuous loop [105].

Figure 3.17: One of the plastic scintillators EJ-276 used in the neutron spectrometer.

Once the level reaches the desired value, the system is switched to the recirculation mode. The argon gas flow is stopped and, by means of open/closing valves, the argon vapor is pushed through a recirculation pump inside the purifier system, which consists of a SAES hot getter. Then, the argon gas is purified and pushed again into the system, and the loop can start again.

3.2.3 The Neutron Spectrometer

The ReD experimental setup includes a neutron spectrometer located approximately 100 cm from the TPC. This spectrometer is used to detect the scattered neutron n' after interacting with the argon nucleus inside the TPC.

It is composed of 18 1-inch Pscis of EJ-276 51-mm long and coupled each with its Hamamatsu R1924A PMT (see. Fig 3.17). They are produced by Scionix and have improved PSD features with respect to the previous performance of past plastic scintillators produced with the same Eljen Technology [106, 107]. All the Pscis are housed in two 3D-printed arrays, each shaped as a 3 × 3 matrix. These scintillators are chosen to perform n/γ PSD of the particle hitting the spectrometer via the f_{prompt} parameter, as it is possible to see in Fig.3.18, while their small diameter (1 inch) allows to obtain a better granularity on the neutron position in the kinematics calculation.

The custom-built structure of the spectrometer consists of a frame made with ITEM beams where the two plastic matrices have been fastened, as shown in Fig. 3.23. The center of the frame has been aligned with the position of the TPC inside the dewar and with the position of the source. With respect to it,

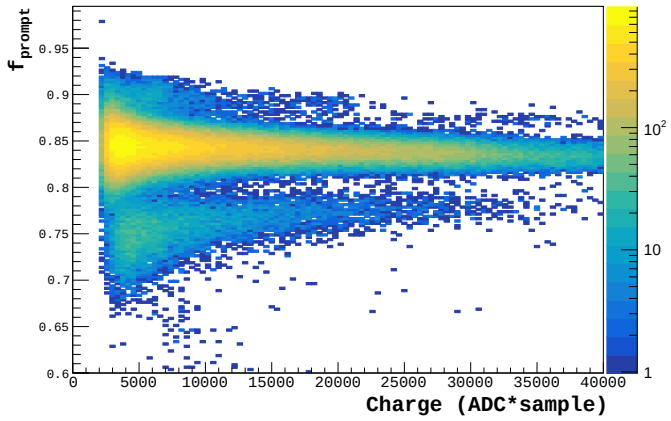

Figure 3.18: The parameter f_{prompt} allows to identify the nature of particles that deposited charge in the Pscis. The data shown were taken during a calibration campaign with the ^{252}Cf source. The upper band is populated by γs while the lower one by neutrons.

the two matrices are displaced at about $\pm$ 25 cm to control the alignment systematic. Furthermore, the matrices are placed outside the direct exit cone of the neutrons to avoid detecting neutrons coming directly from the source that have not interacted within the TPC. The scintillators are positioned to cover the angle range $\theta_s = 12^\circ - 17^\circ$ with respect to the TPC.

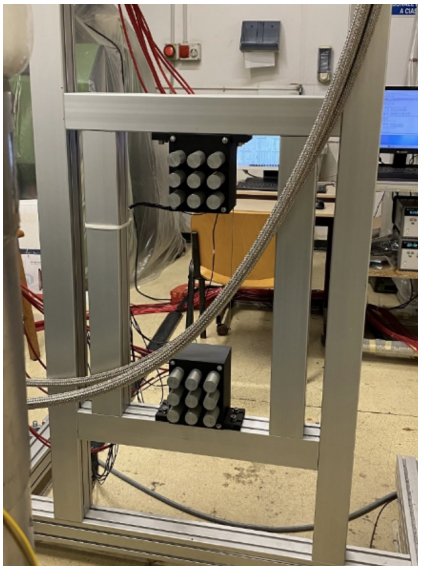

Figure 3.19: Photo of the neutron spectrometer. The 18 Pscis are divided into the two symmetrically-placed matrices.

3.3 Data taking at INFN-Sezione of Catania

This campaign was conducted at the INFN Sezione of Catania. The experimental setup for ReD was assembled in a dedicated laboratory in the workshop rooms of the Physics Department at the University of Catania, shown in Fig. 3.22. The commissioning phase began in 2021 and lasted until the end of November 2022, when the TPC and the entire cryogenic system were cooled to the operating temperature of 87 K. The runs collected in December were mainly devoted to checking the performance of the TPC in both single and double phases, and the data taking campaign of physical events started in January 2023 and lasted until March 2023.

Calibration runs with external gamma sources (^{241}Am and ^{137}Cs) and laser runs were performed weekly. The data acquisition (DAQ) system is controlled by the same external trigger signal. Calibration and background runs are conducted to determine and correct the TPC response, ensuring homogeneity within the detector.

Laser runs are performed to assess the stability of the SiPM by evaluating their single electron response. The SiPMs used in ReD can be calibrated to ob-

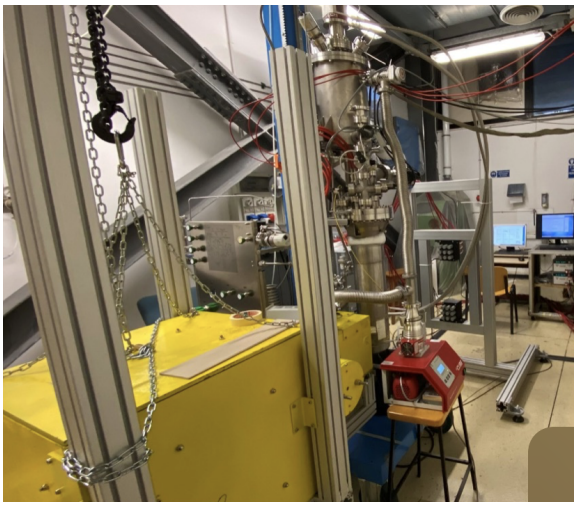

(a)

(b)

Figure 3.22: Photos of the real thing in the lab of INFN-Sezione of Catania located in the Physics department. Picture **(a)** is the perspective that faces the neutron spectrometer as it is seen by neutrons, while **(b)** shows the opposite point of view.

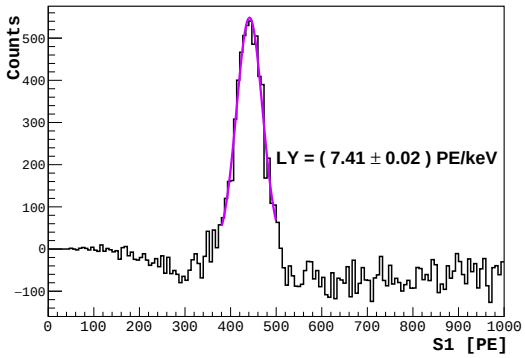

Figure 3.23: ^{241}Am is a γ source and the spectrum reported shows the full energy peak at 59.54 keV. Once the background is subtracted, the peak is fitted to estimate the light yield (LY).

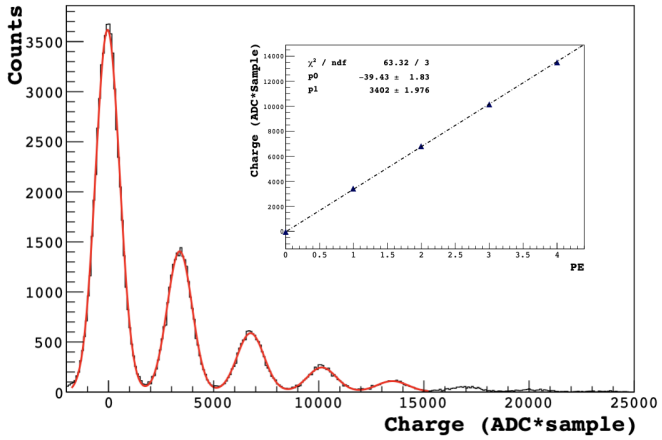

Figure 3.24: Charge spectrum measured by one channel in the bottom tile of the TPC of ReD. Each peak corresponds to a specific number of detected photoelectrons. A fit with a sequence of Gaussian functions is performed on this spectrum to obtain the mean value of each peak. The SER value for the SiPM is extrapolated by linearly fitting the mean values, as shown in the inset.

tain a normalization factor, allowing the conversion from charge to energy in terms of photoelectrons (PE) produced per incident photon. This calibration is performed by studying the single electron response (SER) spectrum, integrating the charge of each detected pulse to form a charge spectrum where each peak corresponds to one or multiple photoelectrons (see Fig. 3.24) [105]. In the photoelectron spectrum, or SER, the distance between consecutive peaks is constant and is used to calculate the gain, which corresponds to the charge released by a single SPAD. The SER in ReD is investigated using a Hamamatsu PLP-10 pulsed diode laser, externally triggered at 100 Hz, with a wavelength of 403 nm and 50 ps pulse emissions. A bundle of optical fibers is used to deliver the laser pulses to the inner volume of the TPC. Laser runs were also performed to study cross-talk and afterpulsing effects in SiPMs. On average, these two processes can result in the detection of more than one photon for each primary single-photon emission. The proper photon counting statistics was modeled according to a geometric chain process by Vinogradov [108, 109]. As in previous ReD campaigns [53, 110], this model allows the derivation of a duplication coefficient to correct the final PE gain.

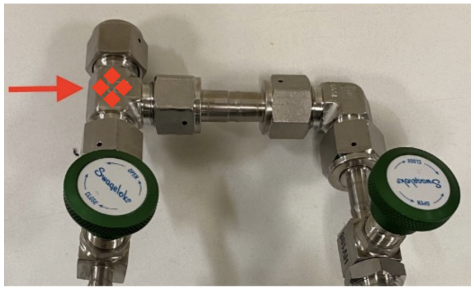

(a)

(b)

Figure 3.27: **(a)** Picture of the pipe in which are hosted the ^{83}Rb evaporated on carbon beads. The photo in **(b)** shows the pipe installed in the cryogenic system. Flowing argon transports and diffuses krypton within the TPC.

3.3.1 Calibration with ^{83m}Kr

In addition to the routine calibration runs described above, a calibration procedure is performed to evaluate the uniformity of the response of the TPC in $x-y$. This is possible thanks to an internal source, ^{83m}Kr , directly flushed into the TPC. ^{83m}Kr is the progeny of ^{83}Rb, which decays by electron capture with a half-life of 86.2 d. It is widely used in calibrating both LXe and LAr detectors since it decays via emission of 32.1 keV and 9.4 keV conversion electrons with $T_{1/2}$ = 1.83 hours, thus allowing a characterization of the response of the detector at low-energies [105, 111].

The way it is possible to calibrate the ReD TPC with ^{83m}Kr is by evaporating ^{83}Rb on carbon coal grains that are hosted in a proper pipe and then sealed for integration in the experimental setup. By opening the appropriate valve, ^{83m}Kr is circulated through the system for data collection. Within approximately 24 hours, ^{83m}Kr fully dissolves in the LAr inside the active volume of the TPC, leaving no long-lived radioisotopes behind. The activity of the ^{83}Rb in ReD was about 25 kBq.

Using this source it was possible to perform ER calibration at low energy

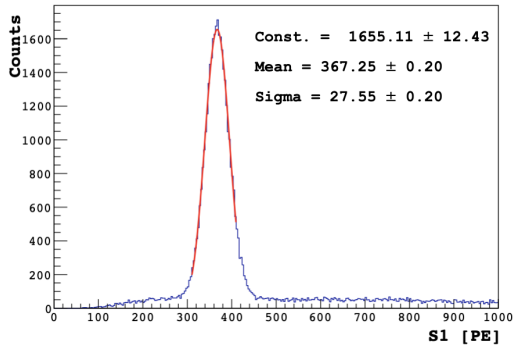

(a)

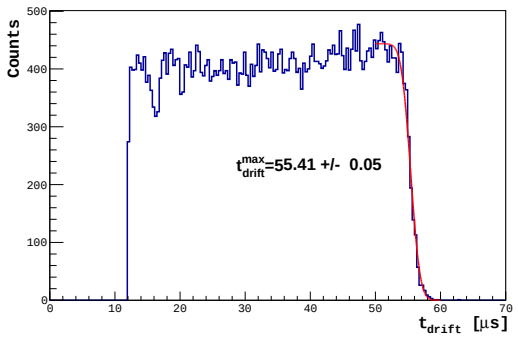

(b)

Figure 3.30: **(a)** S1 distribution from a ^{83m}Kr calibration run. **(b)** Electron drift time distribution from the same ^{83m}Kr calibration run. As it is possible to note, it is flat, as expected.

and test the uniformity of the response of the TPC. In Fig. 3.30 (a) is shown the measured spectrum, while in Fig. 3.30 (b) the distribution of the drift time is reported, flat as expected in correct uniformity configuration.

3.3.2 Data Acquisition and Software

The ReD Data Acquisition (DAQ) system is made by three CAEN V1730 Flash ADC Waveform Digitizers, each with 16 channels for a total of 48 acquisition channels. Of these channels, 28 are dedicated to SiPM readout: 24 for the top tile and 4 for the bottom tile. Additionally, 2 channels are allocated for BaF_2

detectors and 18 for Pscis. An external clock module by TRIUMF synchronizes the three boards. The DAQ software is a custom-made version of the PADME experiment code [112], which allows the data taking via a graphical interface. Several trigger conditions can be configured via a software interface. The width of the acquisition window varied according to the type of run being performed, which depended on the nature of the signals to be recorded. Also, the pre-trigger window, used to estimate the baseline, which is then subtracted from the total signal integral, is set accordingly.

Typical trigger configurations include:

- **Single-phase mode**: Used primarily to record the scintillation signal, with a window set to 20 µs and a pre-trigger of 6 µs.
- **Double-phase mode**: Employed in calibration runs when the TPC is operated to detect both scintillation and ionization signals, featuring two possible window settings, 100 µs and 120 µs, with corresponding pre-trigger values of 10 µs and 9.6 µs.
- **^{252}Cf source trigger in physics runs**: Configured with a window of 80 µs and a pre-trigger of about 5 µs.

In order to digitize signals, each ADC has a resolution of 14-bit, a 2 V_{pp} (Peak-to-Peak Voltage) input range and a sampling rate of 500 MHz. SiPMs are supplied by a CAEN SY 5527 power supply module together with two Agilent 32250A for the FEBs biases, while a CAEN 1471 power supply module is used to set-up the fields of the TPC.

A Lakeshore 336 Temperature Controller is used to monitor the liquid argon temperature inside the cryostat by reading the four PT-100. A Keithley 2280S powers the resistor to create and control the gas pocket inside the TPC. Finally, all the sub-systems are remotely controlled by the Slow Control system developed and maintained by INFN - Genova group. This, via a user-friendly graphical interface developed in LabView language [113], enables the operator to control all electronic components of the system and monitor all parameters of the cryogenic system.

Trigger

When designing the trigger logic, it had to be taken into account that at the energies involved for the desired nuclear recoils, the only detectable signal in the

TPC is S2, as the scintillation signal is often too weak to be detected. This poses a challenge for integrating the TPC into the trigger logic, which typically relies on the faster and more easily detectable scintillation signal. For this reason, it was decided to acquire the TPC in slave mode and select the events of interest during offline analysis. The trigger signals are produced by the tagger detectors only, i.e. the two BaF_2 and Psci. For an event to be considered a valid physics event, a signal must be detected in one of the two BaF_2 detectors within an appropriate time window, coinciding with a signal from any of the Pscis after the particle has completed its flight. The final trigger logic can be represented as (BaF_2 in `OR`) `AND` (Psci in `OR`), meaning a coincidence between a signal in one BaF_2 detector and any of the Pscis.

Numbering the three boards as board0, board1, and board2, the channel distribution is organized as follows:

- **board0**: 2 BaF_2, 4 SiPMs from the bottom tile and 10 SiPMs from the top tile
- **board1**: remaining 14 SiPMs from the top tile and the first 2 Pscis from the upper array
- **board2**: 7 Pscis from the upper array and the 9 Pscis in the lower array

The master trigger signal is produced by using a standard NIM logical module by ORTEC coupled with a Lecroy 428F linear FAN-IN/FAN-OUT module. Subsequently, the building of the event is performed offline in the event reconstruction phase by looking at the events recorded in the TPC.

Offline reconstruction

Once the event has been collected following the trigger, the combination of the ToF measurement and the PSD response from the neutron spectrometer will determine whether or not to look for a trace in the TPC.

To enable data sharing for collaborative analysis, the raw data recorded on the local DAQ machine are also stored on two separate systems: the INFN-CNAF Tier 1 (both on disk and tape) and the 'astro' machine, which is maintained by the FAPESP group in Brazil. Finally, ROOT trees (TTrees) are created via the same custom-made reconstruction software developed inside the ReD working group, called *red-daq-light*, and used in previous campaigns. A novel

reconstruction model, *red-deconv*, has been developed for this campaign, with the capability to deconvolve the SiPM response from the raw waveforms, which inspired its name. The observed raw traces in ReD are the convolution of the PE collection with the Single Photo-Electron (SPE) time response. The SPE time response is wide enough to distort the original shape of S1 and S2 pulses and the deconvolution method that restores the original shapes. Thus, the analytical parametrization of the time response of the SiPMs to one SPE is

$$spe(t;\tau_s,p_2,\sigma_s) = p_s\frac{e^{-t^2/2\sigma_s^2}}{\sqrt{2\pi}\sigma_s} + \left(1-p_s\right)\frac{e^{-t/\tau_s}\,e^{\sigma_s^2/2\tau_s^2}}{2\tau_s}erfc\left(\frac{\sigma_s^2-t\tau_s}{\sqrt{2}\sigma_s\tau_s}\right) \tag{3.4}$$

where τ_s, p_s and σ_s (with the subscript s for slow) are parameters of the SiPM, and their value are 595.35 ns, 0.89 and 12.53 ns, respectively. This formula is used to fit the raw waveforms and is the first step in the refined reconstruction used in this campaign, which distinguishes between two levels:

- The *Red level*, where exactly this fit takes place, and a preliminary search for pulse and charge integration. TTrees are created with these deconvolved packets. An example of a raw waveform and its deconvolved form are provided in Fig. 3.33.

- The *Blue level*, starting from the deconvolved wavefrom, signal cluster searches, $x-y$ reconstructions and subsequent time corrections are performed. TTrees with the integrated quantities of the variables of interest obtained from cluster and pulse shape fits are generated.

The so-called blue events are those used in the high-level analysis.

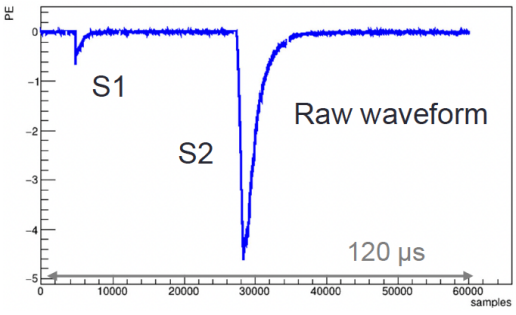

(a)

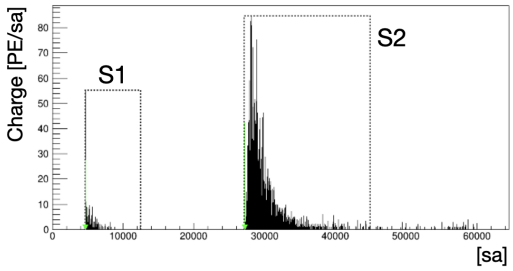

(b)

Figure 3.33: In **(a)** is shown a raw waveform averaged over all the SiPMs, while in **(b)** is displayed its deconvolved form obtained form at the Red level of the reconstruction performed with red-deconv.

3.4 How to select NR events

Physics runs were acquired continuously over three months, with a registered event rate of ~ 2.5 Hz for waveforms with a length of 80 µs (about 600 GB/day). Once all data have been acquired, the next step is to identify suitable candidates for nuclear recoil events. This selection is achieved by analyzing signals from both the neutron spectrometer and the two BaF_2 crystals. The trigger logic employed enables tagging of approximately 60% of spontaneous fission events. Following each fission event, the emitted neutrons travel toward the TPC, located approximately 92.1 cm from the ^{252}Cf source. The neutrons interact with the argon nuclei via (n, n') scattering. Scattered neutrons within the fixed energy range are subsequently stopped by one of the Pscis positioned 100.4 cm downstream from the TPC, resulting in a total distance of 195.5 cm from the source. The ToF is calculated over this total path, with the expected time range for neutrons being between 40 and 160 ns (see Fig. 3.34).

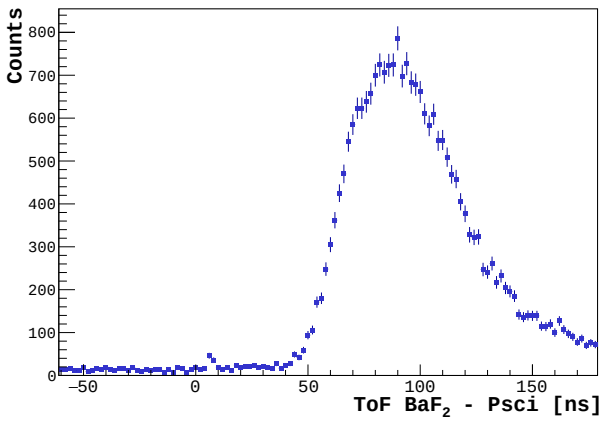

Figure 3.34: ToF distribution for neutrons travelling from the BaF_2 to the neutron spectrometer.

As can be seen in Fig. 3.35, the resolution of the ToF measurement is ~0.7 ns, allowing an event-by-event measurement of the neutron kinetic energy at better than 5%.

Through ToF measurements, some background sources can be eliminated: a background source that is easy to reject consists of γ-rays emitted by the source that do not interact during their flight. These γ-flash events are detected

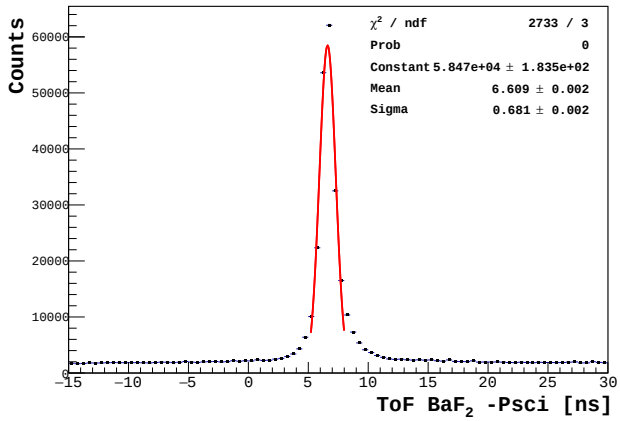

Figure 3.35: The ToF distribution for the γ flashes is fitted with a Gaussian curve to determine the ToF resolution.

by the Pscis after approximately 6.5 ns, how it is shown in Fig. 3.35. Moreover, the signal by the γ-flash is taken as a reference to perform the time alignment of the signals in the different boards.

Another background source to consider is accidental γ rays. It was observed that events due to accidental γs dominated the trigger rate, while candidate neutron events were about 28 event/hour (0.3%) as expected from simulations. Accidental γs can originate either from ^{252}Cf or the environment, undergoing multiple scatterings with the setup material and reaching the spectrometer in the same time window as neutrons. Thanks to PSD performed with Pscis, it is possible to distinguish neutron events from accidental background events by looking at the time profile of the signals. Fig. 3.36 displays the events recorded by plotting the measured ToF against the parameter f_{prompt} of the Pscis. Distinct loci can be observed in this scatter plot, each corresponding to events of different origins. The γ-rays exhibit a higher f_{prompt} compared to neutrons. Neutrons form a cluster in the upper left part of the plot. In contrast, γ-rays that reach the Pscis without interacting are clearly identified by the high-density spike at a ToF of 6.5 ns.

At this point, there is a series of candidate events where neutron interaction within the TPC may be expected. These are the preliminary steps in the data selection procedure: for these candidate NR events, it is necessary to check the signals recorded by the SiPMs in the TPC.

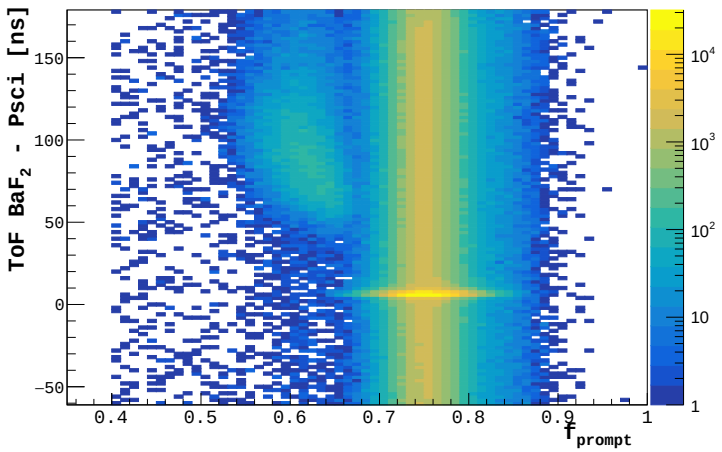

Figure 3.36: Scatter plot showing the distribution of ToF measured between BaF_2 and the neutron spectrometer as a function of the fraction of the prompt light over the total signal seen by the Pscis that allows to perform PSD. The band between 0.7-0.9 is populated by γs events, both accidentals and the spot due to the γ flash. The blob on the upper left part of the 2D plot is populated by neutrons, which have a different f_{prompt} parameter with respect to γ events.

3.4.1 Selection cuts

Additional cuts are based on the arrival time of signals in the TPC, consistent with trigger signals from the trigger detectors, and selections within the fiducial region of the TPC. In fact, only events with an S2 signal in the central (4×4) cm^2 region of the TPC are considered reliable, as predicted by Monte Carlo simulations: any low-energy events at the edge could be due to background events.

After the Blue-level step of the reconstruction procedure described previously, the recorded events are classified based on the number of recognized clusters. Possible outcomes include no signal, S1 + S2 signals, S2-only events, and multiple S2 events. Given the expected energy released by low-mass WIMPs, candidate events are expected to have a single S2 pulse or a very low S1 signal followed by a single S2 signal. Further cuts are applied to remove poorly selected events. The pulse finder has been tested on simulated deconvolved traces and is fully efficient only for events with S1 signals higher than 25 photoelectrons (PE) and for S2 signals formed by 4 electrons. This implies that some low S2 events may be noise rather than true signals from NR. The selection cut keeps only those events having an S2 signal consistent with the maximum drift time within the TPC, that is within 65 μs after the signal of the BaF_2 , and, if an S1 signal is detected, it must be less than 100 PE and with a measured ToF consistent according to the path over the distance BaF_2 to TPC. The final sample of events that passed all cuts consists of 820 events, and 75% of these are S2-only events, as expected from the MC simulations.

The procedure of event selection and the corresponding analysis procedure used on ReD are referred to as the *conventional analysis*, which I will compare to the signal-tagging method I developed during my Ph.D. with a method that involves training neural networks that will be described in the following Chapters.

3.5 Analysis and preliminary results

The goal of ReD is to provide a dataset of valid S2-only events to directly measure the ionization yield of argon recoils based on two-body kinematics. For the events surviving the selection criteria, the recoil energy is calculated using the Eq. 3.1 by entering, event by event, the value of the neutron kinetic energy

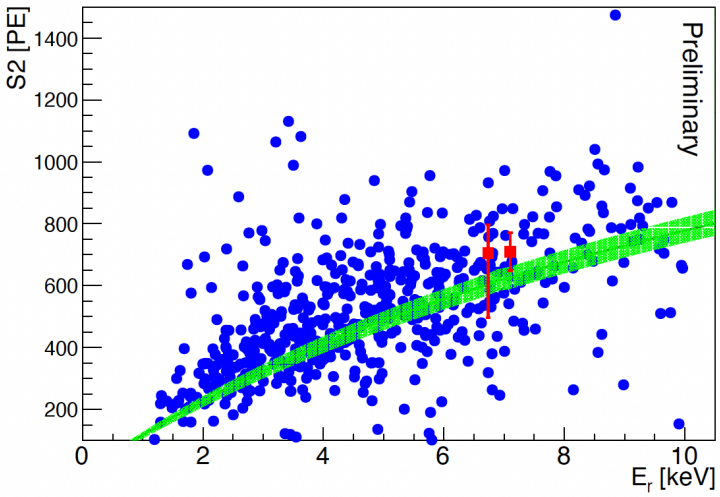

Figure 3.37: Preliminary plot of the measured S2 signals from single-scattering events and the recoil energy (here indicated as E_r) that was shown during the International Conference on Topics in Astroparticle and Underground Physics (TAUP) in [114]. The data are compared with the model derived by DarkSide-50 described in [74] which is the green band superimposed representing the best-fit with uncertainties. The two red points are the experimental measurement from Joshi *et al.* [85] and ARIS [83] at 6.7 and 7.1 keV, respectively

(uncertainty of ± 5%) calculated from the ToF measurement, and the θ_s angle given by the position of the Psci fired by the scattered neutron. The scatter plot in Fig. 3.37 shows the events resulting from the preliminary analysis, as shown at the International Conference on Topics in Astroparticle and Underground Physics (TAUP) in August 2023 [114]. Although initially considered, events with a recorded scintillation signal proved to be outliers due to multiple scattering within the TPC, as confirmed by the MC simulation, and consequently have been discarded.

The S2 signal recorded in the TPC is measured in photoelectrons (PE). However, to determine the charge yield and enable comparison with data from other experiments discussed in Sec. 2.4.2, this signal must be converted from PE to the number of electrons, N_{e^-}. This conversion is achieved by scaling the signal by the factor g_2. A preliminary estimate of g_2 is obtained through a cross-calibration procedure on the ReD data using the model developed by DarkSide-50. This procedure yields a value of approximately 17.2 PE/e^-, which is cur-

rently being used. In Fig. 3.37 are also included, overlaid on the data, predictions from the model described in [74] and the two experimental measurements known in literature by Joshi *et al.* [85] and ARIS [83] . It should be noted that the experimental point of Joshi *et al.* is rescaled using the yield of a single electron from the 2.8 keV line of ^{37}Ar.

The process of directly inferring the g_2 value from ReD data is currently underway. Once the analysis is finalized, the ReD experimental data will be employed to refine the parameters of the DarkSide-50 ionization model [74], so that it can benefit from the fit on data to compare with Monte Carlo distributions

Chapter 4

Study of signal traces with Machine Learning algorithms

In Sec. 3.4 the method employed for the identification of S2-only events from NR has been presented, starting from the selection performed via the tagger detectors to the cuts applied in the conventional analysis.

It is important to note that the pulse finder and the reconstruction algorithm used in the conventional analysis were developed and tested on a dataset of deconvolved waveforms similar to those obtained at the Red level, but generated using a detailed Monte Carlo simulation. Instead of programming a signal detection method and testing it on simulations, an alternative approach could involve developing a method that automatically learns the fundamental features of the data to identify the presence of a signal relative to the background. This approach falls into the category of problems where, given a large amount of data, machine learning can be used to extract information inherent in the data itself, potentially improving performance over traditional methods.

In 1959, Arthur Samuel coined the term machine learning (ML) to refer to the study of computer systems that learn and adapt automatically from experience without being explicitly programmed [115]. In particular, ML is a set of methods that can automatically detect patterns in data and then use those patterns to make predictions or other kinds of decisions. Practically, ML algorithms are useful for solving optimization tasks in case studies where an effective model for describing or interpreting the available data is not always known. On the basis of the model training approach, ML can be divided into three cat-

egories:

- *Supervised learning*: the goal is to learn a mapping from inputs **x** to outputs y, given a labeled set of input-output pairs. Typical problems solved with a supervised approach are classification ones, when each input is assigned to one of a finite number of discrete categories, or regression problems if the desired output consists of one or more continuous value

- *Unsupervised learning*: the algorithm is given a set of input information and must recognize underlying patterns in the data that would otherwise be difficult to enhance. Examples of applications are clustering problems, where the goal is to discover groups of data with similar features within the set, or to determine the distribution of data within space, known as density estimation, or to project data from a high-dimensional space into a lower dimensional one, to simplify the analysis or for visualization purposes

- *Reinforced learning*: this technique addresses the problem of determining actions that maximize reward, with the learning algorithm discovering the optimal steps through trial and error

Therefore, in addition to the conventional approach developed to recognize signals recorded by the SiPMs in the TPC, I collaborated with the group involved in the Centro Nazionale for HPC, Big Data and Quantum Computing, to apply machine learning algorithms in the study of waveforms for the identification of candidate S2-only events. Waveforms are time sequences characterized by background noise and signal pulses, that can be detected when a threshold is exceeded. After consulting the literature to find the type of architecture best suited to the problem at hand, the choice fell on the use of deep learning neural networks, specifically convolutional autoencoders. There are several reasons for this choice. To test the conventional selection criterion, labels associated with each event, such as the S2 value, were not used. Instead, an unsupervised approach, typical of autoencoders, was preferred. Autoencoders are particularly well-suited for processing time series data, as they can learn to compress and reconstruct sequences, capturing essential features and patterns in an unsupervised manner. The decision to use convolutional layers enables the network to automatically extract hierarchical features, reduce the

number of parameters through shared filters, and provide robustness to translation. Additionally, convolutional networks are computationally efficient and have demonstrated effectiveness across a wide range of tasks.

4.1 Deep Learning with Autoencoders

Deep Learning (DL) is a subset of ML characterized by deep stacks of computations. This computational depth has enabled DL models to untangle the kinds of complex, hierarchical patterns found in the most challenging real-world data sets by building and training so-called neural networks. Neural networks consist of *neurons* that each performs a simple computation. Their power lies in the complex connections between each single unit, mimicking the interconnected structure of the human brain. Because of their power and scalability, neural networks have become the gold standard of DL and have found endless applications in diverse fields, from medicine to economics, and physics. In the plethora of types of neural network architectures, it has been chosen to work with AutoEncoder (AE), whose goal is to learn a compressed representation of an initial input, even though it may have a high dimension [116]. The architecture of an AE, schematically represented in Fig. 4.1, consists of three elements: an encoder network and a decoder one, and an intermediate layer, referred to as *latent space* or *bottleneck*, between the previous two sub-networks. The encoder and the decoder each have a specific task to perform: the former compresses the input producing an output with lower dimensions, i.e. the latent or encoded representation, while the latter attempts to recreate the input from the compressed vector provided by the encoder. Usually, the layers in the decoder are designed as a mirror image of the encoder stage. This means each layer in the decoder has an inverse relationship to its corresponding layer in the encoder, reversing the roles of inputs and outputs to reconstruct the original data from the encoded representation.

The output of the encoder in the latent space is a fixed-length vector that provides a compressed representation of the input data, then exploited by the decoder to reconstruct them. The "goodness" of the prediction is estimated by directly comparing the input with the reconstruction delivered by the AE. If the AE performs well, the encoded-decoded data should closely resemble the original data. This can be quantified by measuring the reconstruction error between

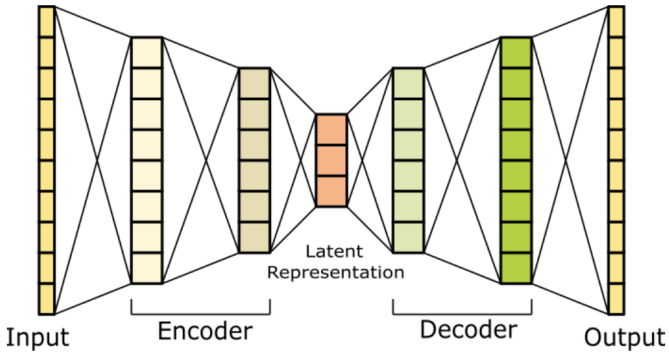

Figure 4.1: The diagram illustrates the architecture of an autoencoder. From left to right, it is possible to see the encoder layers, which gradually lead to a vector of reduced size in the latent space, and, mirrored, the decoder. The resulting output has the same dimension as the original data.

the input and output. For discrete input values in the range [0,1], the typical error metric used is the *binary crossentropy*. For other types of input, the *mean squared error* is usually the best choice. While training an AE, the weights of the network are updated using a backpropagation algorithm to minimize the differences between the output of the decoder and the original input. This process is referred to as self-supervised learning since the input data are employed to supervise the network training process. Such a learning paradigm facilitates the discovery of inherent similarities in the data without the need for pre-defined labels typical of supervised learning. Indeed, the main advantage of AEs is to implicitly highlight the fundamental characteristics of a dataset, being the network forced to learn a compressed representation while disregarding the background noise and redundancies in the dataset, making this architecture useful in physics tasks like feature extraction, noise removal [117] and anomaly search on large datasets [118].

4.2 Data selection

When working with neural networks and machine learning models, it is crucial to prepare distinct sets of data for the different stages of model development:

- *Training set*: this is the dataset used to train the model, and it should be

large and diverse enough to represent the variety of events the model is expected to be used on. During the learning phase, the model exploits this data to adjust its weights and improve its performance on the task at hand;

- *Validation set*: those data are used during the training process to assess performance accurately. This dataset is separate from the training set and is not used to modify the model weights, but instead to monitor the learning process, and possibly highlight the presence of overfitting, i.e. an excess of training that prevents the model from successfully processing data never seen before, thus resulting in a loss of its generalizing power;

- *Test set*: this set is used once the training is finished, to evaluate the ultimate performance of the model. This dataset is completely independent of the training and validation sets. The test set offers an unbiased assessment of the capability of the model to generalize to new, unseen data.

Autoencoders are tailored to the specific dataset they are trained on, learning to encode and decode exclusively that type of data. This specialization allows them to excel at recognizing and reconstructing data that share the same distribution and characteristics as their training set, while their ability to generalize to different types of data is limited. Therefore, careful selection of the training data is crucial. The initial plan was to train the model using S2-only events from nuclear recoils. To achieve this, a list of candidate events was compiled from 118 runs conducted during the source irradiation data acquisition period. After applying the selection criteria based on ToF measurement and PSD from Pscis, as described in Sec. 3.4, the initial dataset was filtered down to 1498 candidate S2-only events from NRs. However, this sample size was found to be insufficient for adequately training the model.

Recognizing that the S2-only signals produced by electron recoils are indistinguishable from those produced by nuclear recoils, a new strategy was adopted. Instead of relying solely on the limited NR events, a large dataset of accidental S2-only signals by γ-rays, which also provide a wide variety of tracks, was used to train the model. A data sample of 10505 S2-only events from ERs was collected by performing the same selection based on the signals from the tagger detectors. This approach ensures that the model is trained on a sufficiently large and varied dataset, while still being validated on relevant S2-only

events from NRs, that are used to test the trained model.

The goal of this work is to develop a data-driven tagging criterion for signal events, thus it is advantageous to use S2-only events from (n,n') elastic scattering to test the robustness of the final model. Therefore, the preliminary dataset of neutron events recorded in the TPC and presented in Ref. [114] serves as a benchmark, since this class of events have been deeply investigated in the conventional analysis described in the previous Chapter.

4.2.1 Extraction of waveforms

After the definition of the training (plus validation) and test dataset, the next step is the extraction of the recorded waveforms, that are fed to the model. The extraction of the raw waveforms is performed at CNAF, where they are identified by their run ID and corresponding event number, therefore extracting the waveforms recorded by the SiPMs in the upper tile. The first dataset I worked on was the train set, and then the procedure was repeated for the test set.

For each event in the list of candidate S2-only events from ER, individual waveforms recorded by the SiPMs are read and calibrated using the Single Electron Response parameter for each SiPM. These calibrated waveforms, in $\frac{\text{PE}}{\text{sample}}$, are then summed into a single waveform on which a smoothing filter is applied, in particular a moving average with a fixed window. This helps to reduce noise and fluctuations in the waveform, making it easier to analyze trends and patterns.

The resulting averaged waveforms consist of 40000 samples, each corresponding to a 2 ns interval (given the 500 MHz sampling rate of the SiPM acquisition) for a total duration of 80 μs. However, to enhance computational efficiency, the waveforms were downsampled, calculating the average every 4 samples. The final traces have a length of 10000 samples, thereby reducing the computational load without significantly compromising the integrity of the data. The obtained dataset of candidate S2-only events from ERs comprises 10505 waveforms, which are shown collectively in Fig. 4.2.

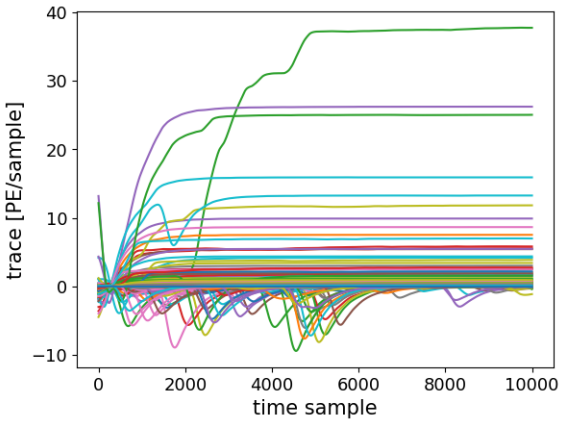

Figure 4.2: Dataset of S2-only candidate events seen in the TPC after an ER event. Downsampling from 40000 to 10000 has already been applied (see text for more details).

4.2.2 Pre-processing procedure on the data

The obtained dataset of waveforms has to be cleaned to remove obvious spurious signals and events with a non-constant baseline. Therefore, a preliminary selection of good-behaving traces was performed, as part of the pre-processing phase, mainly involving a study of the first 100 and last 100 samples of the baseline. For each trace, the standard deviation (σ) is calculated over these initial and final 100 samples. Events with a dispersion greater than 0.025 $\frac{\text{PE}}{\text{sample}}$ either at the beginning or the end are discarded (see Fig.4.5).

These first two cuts discard about 6% of the initial waveforms, removing approximately 600 and 30 events, respectively. After ensuring baseline stability at both the beginning and the end, baseline constancy is verified. Mean values are calculated for the beginning and end of each trace, and their difference is shown in Fig. 4.6. Waveforms with a start-to-end difference greater than 0.02 $\frac{\text{PE}}{\text{sample}}$ are discarded. This step removes about 20% of the remaining events, leaving a data set of 7775 events. Subsequently, the waveforms are shifted to align their baselines around zero. An offset is calculated for each waveform, defined as half of the start-to-end difference previously calculated, and this parameter is used to adjust the trace. This shift procedure alters the units of the waveforms, which are now more appropriately expressed as arbitrary units (A.U.). Fig. 4.9 (a) shows the waveforms that remain after applying the cuts and

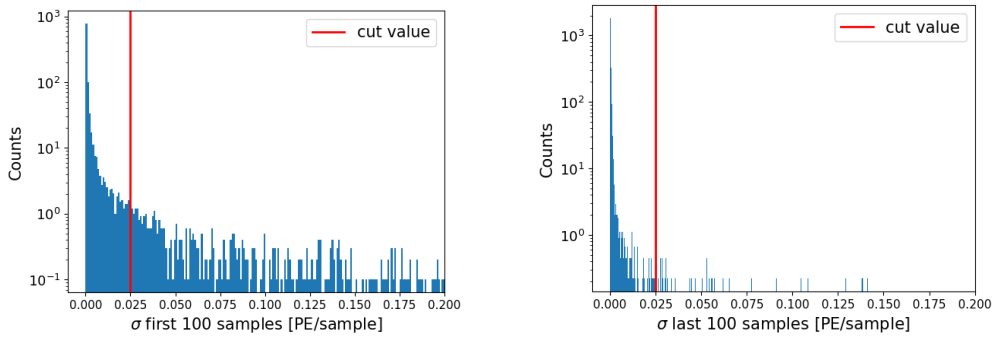

(a) Dispersion first 100 samples (b) Dispersion last 100 samples

Figure 4.5: Histograms of the dispersion of the first **(a)** and last **(b)** 100 samples for all the traces selected as S2-only events from ER. The cut value selected is 0.025 $\frac{\text{PE}}{\text{sample}}$ and all the waveforms over this threshold have been discarded.

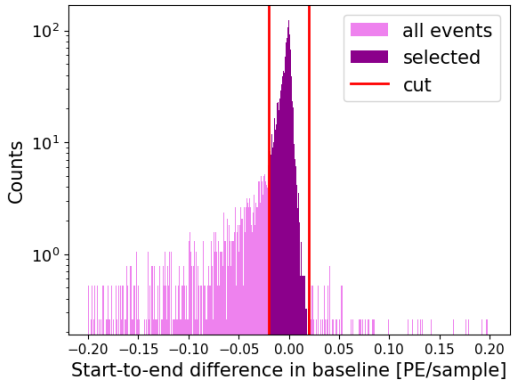

Figure 4.6: Difference between the mean at the beginning and at the end of each trace. Events outside the two red lines, indicating a jump in the baseline larger than 0.02 $\frac{\text{PE}}{\text{sample}}$, are discarded.

shifting their baselines.

Finally, events with a maximum value, corresponding to the peak in the signal pulse, higher than 1 A. U. were also removed. This cut has practically the same effect of normalizing the dataset, but it was evaluated to be more convenient since in this way small signals, whose identification is the main aim of this study, are not numerically reduced. The traces are then flipped upside-down to ensure all values are positive. Fig. 4.9 (b) shows the dataset, before

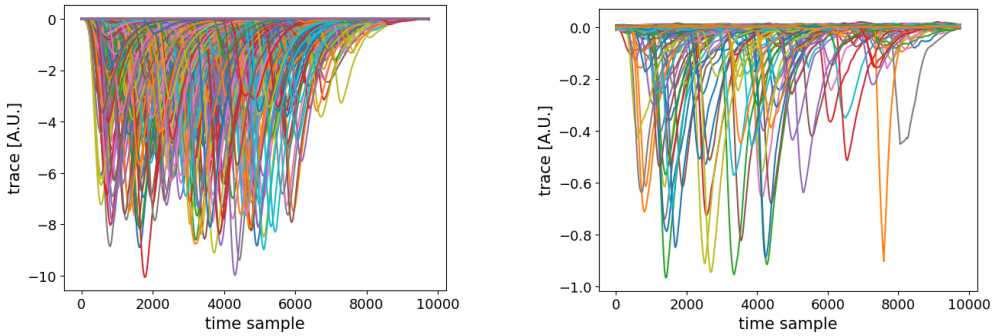

(a) Shift of the baselines

(b) Selection on the peak values

Figure 4.9: In **(a)**, the waveforms that remain after applying the cuts are shown, with their baselines adjusted to approximately zero. In **(b)**, the final dataset is presented, containing only traces where the peak (i.e., the maximum in the signal pulse) is smaller than 1 A.U.

flipping, resulting from this selection procedure. This dataset, which contains 7120 waveforms, is used to train the network. In Tab. 4.1 all the steps performed in sequence and the resulting dataset sizes are listed.

Candidate S2-only events from NR are also subjected to the same pre-processing selection, and the results are shown step by step in Tab. 4.2, while in Fig. 4.12 the initial and final sets can be visually compared. The cuts are the same as those applied on the training set: this is because all the data fed to the model must have similar characteristics to the data on which the model is trained. It

Procedure step	# events left	% events left
Starting point	10505	100%
Dispersion first 100	9904	94.3%
Dispersion last 100	9871	94.0%
Start-end difference	7775	74.0%
Peak >-1 A.U.	**7120**	67.8%

Table 4.1: Size of S2-only event dataset from ER along different pre-processing steps. In the last column is reported the percentage of events survived from the original dataset. In bold the number of waveforms for the final dataset, that is used to train the model.

Procedure step	# events left	% events left
Starting point	1498	100%
Dispersion first 100	1476	98.5%
Dispersion last 100	1475	98.5%
Start-end difference	1400	93.5%
Peak >-1 A.U.	**1378**	92.0%

Table 4.2: Size of S2-only event dataset from NR along different pre-processing steps. In the last column is reported the percentage of events survived from the original dataset. In bold is the number of waveforms for the final dataset, that is the testing set.

is important to notice that the procedure removed only 8% of the NR dataset, while the events removed from the S2-only candidate from ERs were more than 30%. This is due to the fact that the experiment is designed to collect single neutron scattering events, so that such a type of event is naturally selected with a lower fraction of spurious measurements with respect to γ-ray accidentals, normally considered a source of background events.

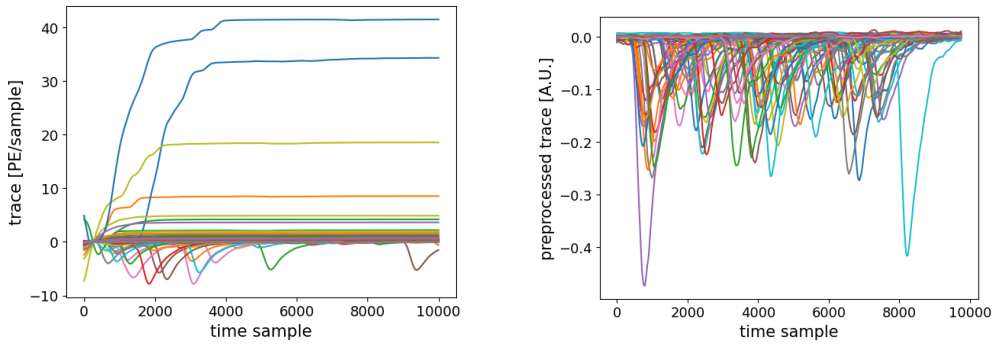

(a) Extracted dataset

(b) Dataset after pre-processing

Figure 4.12: Test set of candidate S2-only events from NR. **(a)** Dataset of waveform before pre-processing procedure; **(b)** dataset after cuts and pre-processing.

4.3 The model

After careful selection and pre-processing of the data, the next step is to build a model. The objective is to train an autoencoder to extract a minimal set of key values that effectively characterize and thus are sufficient to approximately reconstruct each trace. This section describes the architecture of the model and the training procedure. The algorithm is implemented in `Python` [119] and `Keras` [120, 121] with `TensorFlow` [122] backend. All the training and testing of the model was carried out on the INFN Cloud [123] infrastructure. INFN Cloud, part of the ML_INFN project, is a robust and tailored technological platform currently being prototyped and developed by INFN. It aims to provide essential tools for the entire INFN research community interested in high-performance computing and machine learning. INFN Cloud allows users to create virtual machines via a simple and standardized dashboard and offers access to Jupyter Notebooks and multi-user Jupyter Lab tools, facilitating an interactive environment for researchers to share code. In the near future, it will also support hardware accelerators such as GPUs, TPUs, and FPGAs.

4.3.1 The architecture

Since the input data in this study consists of long time series, the most suited type of AE is a 1-dimensional convolutional (Conv1D) one. A Convolutional AutoEncoder (CAE) is a type of neural network that uses convolutional layers in the encoder and decoder. In general, convolutional networks are particularly effective at learning hierarchical representations of data. Convolutional layers, which are described more in detail in the following paragraph, are commonly used for image data, where they can learn to extract features such as edges, shapes, and textures from the input image, and a similar job is performed on time series. The encoder maps the input into a latent representation by passing it through a series of convolutional and pooling layers, followed by a flatten layer and a dense layer. Next, the decoder reconstructs the original dimensions from the latent representation using a series of transposed convolutional layers.

The encoder and decoder weights are typically initialized randomly and are modified during the training to minimize the so-called *loss function*, which measures the difference between the input and the reconstructed output. The built architecture is shown in Fig. 4.15, where is possible to see the chosen lay-

ers and how they are combined together in a mirrored structure: Convolution, Pooling Flatten and Dense layers for the encoder are followed by Dense, Reshape, UpSampling and Transpose layers in the decoder.

Conv1D (Conv1DTranspose) Layer operates by applying convolutional filters along one dimension of the data. Filters, known also as *kernels*, are trainable weight matrices that slide over the input data to extract features. In the convolution operation, the filter is convolved with the input data by calculating dot products between the filter and segments of the sequence. The length of the filter determines how many input elements are covered at a time. This process is repeated for the entire length of the sequence, obtaining a single time bin of the output trace at each step. An arbitrary number of filters can be applied simultaneously, thus producing as many maps of features as decided by the programmer, each one capturing different characteristics from the input. The number of filters in the three conv1D layers is set to 2, 4, and 8, respectively, all with kernel sizes of 32. The filter moves along the input data with a certain *stride*, i.e. the number of time bins the filter moves along the input sequence at each step while applying the dot product operation. A stride of 1 means the filter moves one element at a time, while a higher stride skips more elements, reducing the output size. The set value for the stride is 2 and is the same in all the conv1D layers, effectively reducing the size of the output time series of a factor 2. Another optional feature that can be set when applying the filter in the convolution procedure is the so-called *padding*. It consists of adding extra values, typically zeros, to the edges of the input sequence to control the size of the output. The "same" option is chosen for the padding to ensure that the length of the output traces is not further reduced. The output of the convolution operation is a number of feature maps, equal to the number of filters, each represented by a new time series with a reduced length, which highlights the presence of specific patterns learned by the filters.

Pooling (UpSampling) Layer is a fundamental step in convolutional networks, playing a crucial role in downsampling the feature maps while retaining important information. It helps in controlling the complexity of the model, preventing poor generalization performance, and improves computational efficiency by reducing the number of parameters and compu-

tation required in subsequent layers. In particular, each convolutional 1D layer is followed by an with average pooling layer which computes the mean every 2 time bins of the output traces, effectively halving the size of the trace.

Flatten (Reshape) Layer converts the multi-dimensional output from the convolutional layers into a one-dimensional vector by concatenating them. This transformation is crucial because the Dense layer that follows expects a one-dimensional input.

Dense Layer, also known as the fully connected layer, connects every input node to every output node, which in this case constitutes the bottleneck of the CAE. The dimensionality of the data is then reduced and the most important features are captured in the latent space. This compressed representation is crucial for the ability of the CAE to perform tasks like dimensionality reduction, noise reduction, or feature learning.

In the developed CAE model, the latent space dimension is set equal to 4. This choice was initially empirical, but other training at different dimensions were also performed. More details are provided in Sec. 4.4 and in Appendix A.

Finally, it should be noticed that the length of the input waveforms had to be reduced to obtain the correct size for the output traces, given the described sequence of layers that reduce, in the encoder, or increase, in the decoder, the traces size of fixed factors. In particular, a length of 9728-time bins has been selected by removing 125 samples at the beginning and 147 at the end of each waveform.

Another key aspect in building the network is choosing an appropriate *activation function* to assign to each layer. Returning to the CAE built for the purpose of this thesis, the activation function in all the layers is the *Rectified Linear Unit*, `ReLU` for short, defined as

$$\texttt{ReLU}(x) = max(0, x) \tag{4.1}$$

An activation function in a neural network performs a crucial role by introducing non-linearity into the model. This non-linearity allows the network to learn complex patterns and relationships in the data. During training, activation functions help in the backpropagation process by providing gradients that

can be used to update the weights of the network. The use of an activation function is crucial, especially in the dense layer of the developed CAE architecture, as it maps the output to a latent space vector that captures the most important features of the observed waveforms. To understand how the activation function works, it may be useful to consider an example of a simplified AE with an input layer, the reduced vector in the latent space z, and the next output layer. The AE works by first encoding the input $y \in \mathbb{R}^d$ to the element $z \in \mathbb{R}^p$, where $p < d$. During training, the activation function f is used to allow the network to learn and model non-linear relationships in the data. Then, for the encoder it is assumed $f : \mathbb{R}^d \to \mathbb{R}^p$, then $z = f(Wy + b)$, where W is a weight matrix and b a bias factor initialized randomly and updated iteratively during the training. The decoder activation function $g : \mathbb{R}^p \to \mathbb{R}^d$ will map z to $\tilde{y} = g\left(\tilde{W}z + \tilde{b}\right)$. The activation function g, the weight matrix $\tilde{W}$ and the bias factor $\tilde{b}$ are not necessarily related to the corresponding encoder ones. This is a trivial example: to ensure the non-linearity of the network is better to have more layers or non-linear activations, then the AE becomes non-linear, which is better at detecting abstract features.

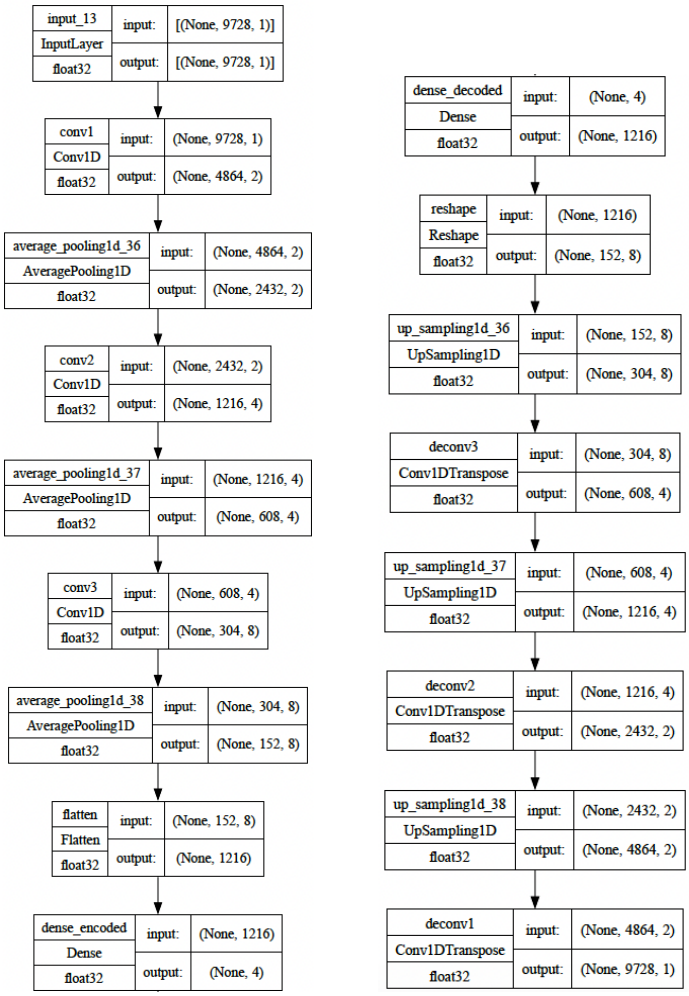

(a) Encoder network (b) Decoder network

Figure 4.15: Box representation of the architecture. **(a)** Starting from the input size, the Encoder compresses the dimension reaching a flatten layer which is the latent representation, a vector of four elements. The Convolutional and Pooling layers extract features and reduce the spatial dimensions of the input. The Flatten layer converts the output of the final convolutional layer to a vector. A Dense layer then reduces this vector to a lower-dimensional representation; **(b)** the Decoder, starting from the compressed representation, outputs a waveform with the same dimension as the input. A Dense layer first expands the low-dimensional latent space representation back to a higher-dimensional vector. The Reshape layer then reshapes this vector back into a tensor suitable for convolutional layers. Transposed convolutional layers combined with UpSampling layers reconstruct the input from this higher-dimensional tensor.

4.3.2 Hyperparameters

A convolutional autoencoder functions much like a precision machine. The layers within the autoencoder serve as the machine's gears, each contributing to the intricate process of data transformation. To operate optimally and begin the learning phase, the machine requires the correct settings, the so-called *hyperparameters*, which include *learning rate*, *batch size*, and a number of *epochs*, that are crucial for optimizing performance and capturing key features of the observed waveforms.

The training of the CAE works by attempting to minimize the reconstruction loss: since the goal is to reproduce the shape of the measured waveform the chosen function is the *mean squared error* (MSE) [124] calculated directly between the input and output traces. Referring to the simplified AE presented in the previous section, the MSE loss can be written as:

$$\mathscr{L}\left(y;\tilde{y}\right) = \|y-\tilde{y}\|^2 = \left(y - g(\tilde{W} f(Wy+b)+\tilde{b})\right)^2 \tag{4.2}$$

During the training, the parameters W, b, $\tilde{W}$ and $\tilde{b}$ are updated to reduce the loss, until $\mathscr{L}\left(y;\tilde{y}\right)$ is sufficiently small and further training does not produce a decrease anymore: when it occurs the network has converged. There are many algorithms for updating the parameters. The one used here is the ADAM algorithm [125], which is the acronym for ADAptive Moment estimation. ADAM is a robust and efficient optimization algorithm widely used for training deep neural networks. What it does is to adapt the learning rate during the training. The learning rate is the size of the step toward the minimum of the loss that is taken at each iteration of the training and thus is related to how much the parameters of the model are updated at each step.

The *batch size* is the number of training samples that are fed to the model in each training iteration, thereby used to update the weights of the layers and the learning rate by the optimizer. For the developed CAE, the initial value of the learning rate is 10^{-3} while the batch size is 100.

Another important aspect of the training is the number of epochs. Indeed, the training dataset is passed through the algorithm many times before reaching convergence. An epoch has passed when the entire data set is submitted to the training algorithm, which corresponds to a number of iterations equal to the size of the training sample divided by the batch size. Tab. 4.3 summarizes the hyperparameters chosen.

learning rate	10^{-3}
batch size	100
number of epochs	100
loss	MSE
optimizer	ADAM

Table 4.3: Selected hyperparameter values for the CAE model.

4.3.3 Training

Once the hyperparameters required to initialize the model and training procedure are set, the data fitting process can begin.

As mentioned previously, the dataset used for training the model consists of S2-only candidate events from ERs, that contains about 7100 events. 20% of these events have been selected as validation dataset. In fact, cross-validation of the performance of an algorithm on a sample independent of the training sample is a practical requirement for an unbiased performance estimate during the training procedure.

In order to obtain, after a complete training cycle, a model that has converged with a sufficiently low loss, a competitive training procedure among different combinations of model and weights initialization has been devised. The training procedure follows these steps:

1. train 25 models with different random initialization of the weights of the layers for 10 epochs, then select the model with the lowest validation loss;

2. the selected model from step (1) is trained for 25 epochs, restarting the optimizer with a different seed 10 times and then, selecting again the model according to the lowest value of the validation loss;

3. repeat step (2) four times, for a total of 110 epochs (25×4 + the initial 10 epochs from step (1)).

It was possible to accomplish this training process by taking advantage of the `Keras` *callbacks*. Callbacks allow user-defined actions to be performed at certain points during the training process of a model. These moments include the start and end of an epoch, the start and end of a batch, or the end of training. Callbacks are used to monitor and influence the training process in real-

time. Specifically, the employed callbacks and their function are described in the following:

- `ModelCheckpoint`: it allows the model and its weights to be saved at the end of each epoch if the validation loss, which is the metric monitored in this work, improves

- `ReduceLROnPlateau`: as its name suggests, this callback reduces the learning rate when the monitored metric has stopped improving. Specifically, it is set to reduce the learning rate by a factor of 2 when the validation loss does not decrease for 5 epochs. The learning rate of the winning model is the one provided to the optimizer in each step of the competitive training process previously described

- `CSVLogger`: this callback is used to monitor the results of the training by saving the training logs, the loss values and other metrics at the end of each epoch in a CSV file

Finally, Fig. 4.16 shows the result of this learning procedure, where the trends of the training and validation losses averaged over the two datasets and plotted versus the number of epochs are reported. The broken line trend and the visible spikes are the result of this non-continuous stepwise training approach: in some cases, the optimizer has to adjust the weights more to find the direction that minimizes the error gradient. It can be noticed that after epoch ~50 the two losses start to separate, with the loss for the training dataset decreasing faster than the one over the validation set. This could indicate the presence of overfitting, which occurs when a model fits the training data too well, capturing even its random fluctuations such as noise and outliers, but performs poorly when applied to unseen data. Nevertheless, in this situation, the hypothesis of overfitting is rejected, since the validation loss is still decreasing by the end of the procedure and the observed separation in the latest epochs is related to the poor representativeness of the validation set since even a few badly encoded-decoded waveforms can produce a substantial increase in the average loss. Another way to verify that we are not running into overfitting is to compare the performances of the model on the training set with those on the test set of S2-only candidate events from NR. The trained model actually returns comparable values for the loss over the test set with respect to the loss over the

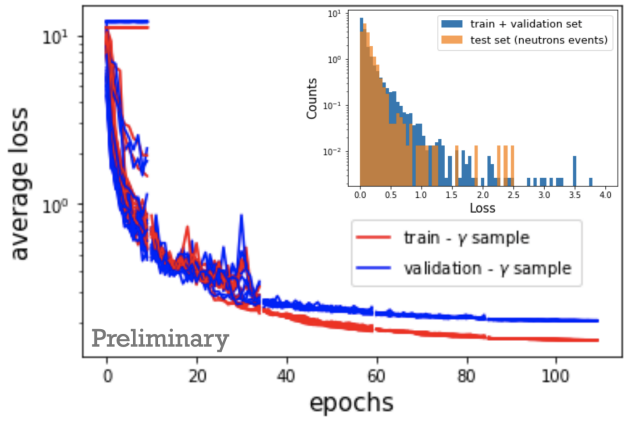

Figure 4.16: Visualization of the trend for the training loss (blue) and the validation loss (red). The inset plot shows the loss for the training set compared with the values obtained on the test set, containing S2-only events identified as nuclear recoils.

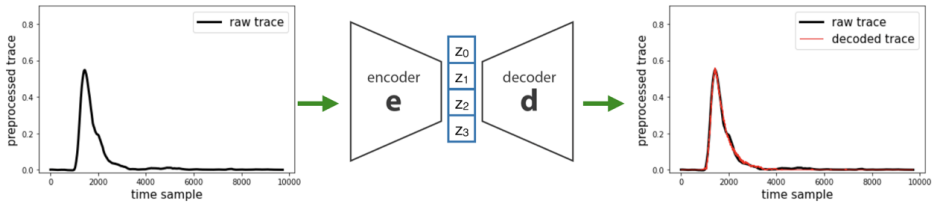

Figure 4.17: A visual representation of the CAE. On the left is an example of one of the waveforms given as input, while on the right, shown in red, it is possible to see how the model maps it back into the output. The vector in the latent space has dimension 4 and will be called z

dataset used in the learning phase, as shown in the inset of Fig. 4.16, therefore confirming the absence of overfitting.

In conclusion, Fig. 4.17 shows the schematic representation of the autoencoder with a 4-dimensional latent space vector, here called z, and also shows the example of a waveform given as input with its corresponding reconstruction as output. As can be seen, the model is able to decode the information in the z vector by returning a waveform that follows the trend of the original one quite accurately.

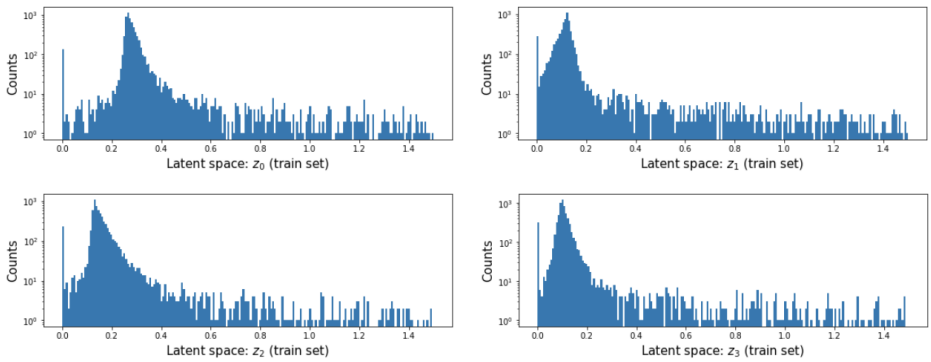

Figure 4.18: The four distributions of each z_i variable plotted for all the traces in the training set. All of them show a continuous trend with a characteristic accumulation value.

4.4 Study of the Latent Space

Once the model was trained and its performance in terms of loss verified, I moved on to the study of the representation in the latent space. In fact, the purpose of this work is to design a signal selection criteria which exploits the features extracted by the CAE model. Indeed, having a close reconstruction of the waveform trend was simply an additional assurance of the performance of the model.

A variable z_i in the latent space is not directly related to any physical property of the data, being used by the model purely to encode the characteristics of the traces needed for an accurate decoding, without holding on to redundancies within the input. Latent variables also provide a low-level representation of the high-dimensional data. The latent space dimension was selected to balance data compression with CAE reconstruction accuracy, minimizing the loss. As previously mentioned, after training models with varying latent dimensions, a size of 4 was identified as the optimal compromise. Such studies are reported in Appendix A.

Initially, I investigated the correlations and dependencies between one variable z_i and each of the others. As can be seen from the plots in Appendix B, no particular dependence was found between them. Then, the four distributions of each z_i for all traces in the training set have been examined. As it is possible to note from Fig. 4.18, the four z_i variables have assume continuous values, but

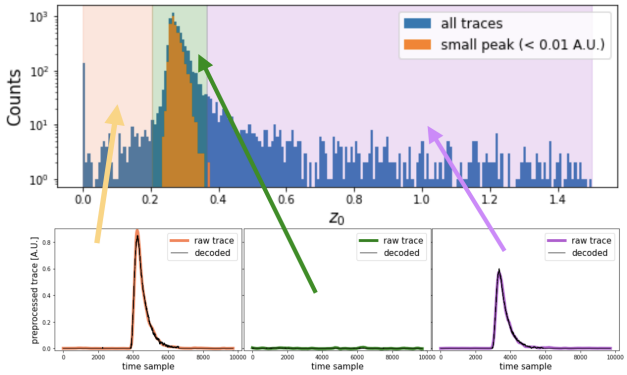

Figure 4.19: The picture shows the distribution of the z_0 parameter of the latent space. One can notice the presence of an accumulation of values in a specific region. Looking at the traces as the parameter value changes, it can be seen that z_0 equal to zero or outside the accumulation region (yellow and violet bands) corresponds to the encoding of signals clearly distinct from the background noise. On the other hand, for values in the accumulation region marked within the green band, it is more likely to find a waveform with no obvious peak in the trace. A further check is to plot the distribution of z_0 only for those traces where the peak is lower than 0.01 A. U. (distribution in orange), which falls in the region around the accumulation.

each distribution also exhibits a peculiar accumulation in a restricted range, which does not comprises the zero. Those four accumulation points are different among the z_i distributions.

The study on the distribution of the z_0 variable is shown in detail in Fig. 4.19 as an example. Qualitative correlations are sought between the values assumed by z_0 and the characteristics of the trace: traces compressed into vectors where $z_0 = 0$ show a signal, as well as traces with a z_0 value smaller or larger than the accumulation value. Traces for which z_0 falls in a neighbourhood of the accumulation value do not show a visible signal but in most cases only present baseline fluctuations.

The next step in this study was to find a quantitative characteristic of the waveforms that allows to pinpoint the presence of pulses, which are normally related to candidate signals. Given that all waveforms are inverted, the highest value of each waveform, referred to as the *peak*, is easy to identify. This quantity is advantageous because it is a consistent feature in every waveform and bypasses the reconstruction step of conventional analysis while remaining

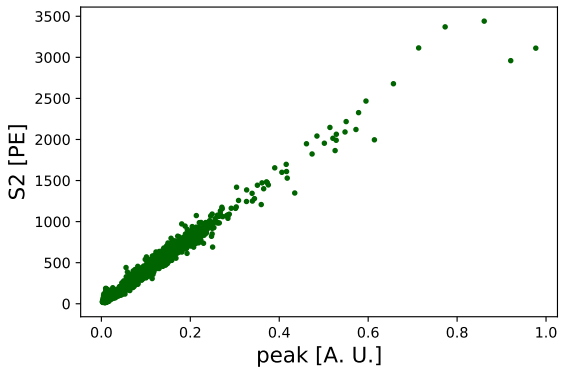

Figure 4.20: Scatter plot of the electroluminescence signal S2 versus the peak value. As can be seen, there is a linear correlation between the two quantities, which justifies the choice of using the peak value as an indication of the presence of a signal.

proportional to the S2 signal value (see Fig. 4.20). In Fig. 4.19, the distribution of z_0 for traces with a peak smaller than 0.01 A.U. is plotted over the whole distribution: it can be observed that the former (in orange) narrows to the interval around the accumulation interval.

Additional qualitative evidence supporting the relationship between the latent space variables and the peak value (used as a proxy for the signal) can be observed in the scatter plot in Fig. 4.21. This plot illustrates how the values of z_0 accumulate in a narrower and narrower range as the peak of the encoded waveforms decreases.

These behaviors are repeated for all z_i variables, as can be seen in Appendix C and Fig. 4.22, which shows the four distributions restricted to traces with a small peak (<0.01 A.U.) superimposed on the overall ones.

It is evident that traces where the peak resembles baseline fluctuations rather than a true signal are located in the region of latent space identified simultaneously by the ranges around the accumulation value of each z_i. This observation led to the development of a criterion for discarding these traces during offline analysis. The next Chapter presents this criterion and the tests conducted to evaluate its robustness. Additionally, this CAE-based tagging method is compared with the selection process used in conventional analysis.

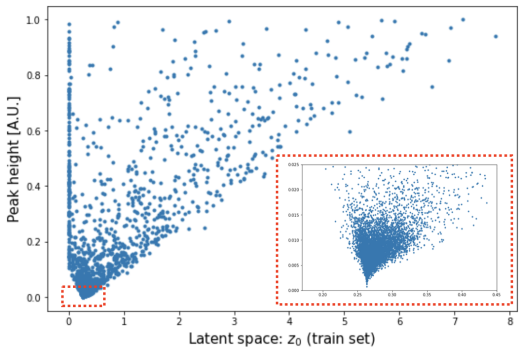

Figure 4.21: Scatter plot of the latent space parameter z_0 with respect to the height of the peak of each encoded and decoded waveform. It is evident how the z_0 values amass at around the accumulation point as the peak decreases. This behavior is consistent across all four variables. The inset provides a zoomed-in view of the plot for peak values lower than 0.025 A.U.

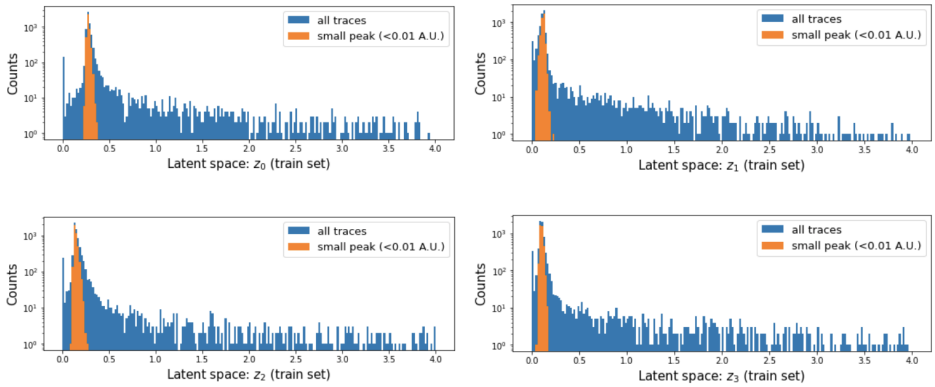

Figure 4.22: Distributions of the zi parameters for the entire training set (in blue) and for the traces with a peak lower than 0.01 A.U. (in orange). As can be seen, the cut according to the peak narrowed the distribution in the region of the accumulation value.

Chapter 5

The tagging criterion and the comparison with the ReD data

In the previous Chapter, an overview of the ingredients needed to build a deep neural network has been given, and in particular, the approach employed for the training of a convolutional autoencoder has been described. The potential of this type of architecture lies in its ability to extract a representation of the given input traces reduced to a few meaningful features. These latent space variables, called z_i, cannot be associated with any particular physical quantity of the traces, but they allow to find a criterion for selecting signals against simple baseline fluctuations.

In particular, the CAE assigns values to the latent variables z_i that increasingly approach their reference values when compressing traces with very low peaks, which resemble random pulses in the baseline more than signals. However, for each variable, this accumulation value is not discrete or easily identifiable; instead, it is an interval whose boundaries must be determined for each latent parameter. Therefore, the nickname *garage* is used to refer to the combination of these intervals, to give the idea of a repository, where the CAE stores events with a simple baseline, less interesting. At this point, it is essential to consider the size of the range for each variable and ensure that no extremely small signals are stored in this region of the latent space. To address these concerns, the distributions of each variable are examined, focusing on traces with a peak < 0.01 A. U. .

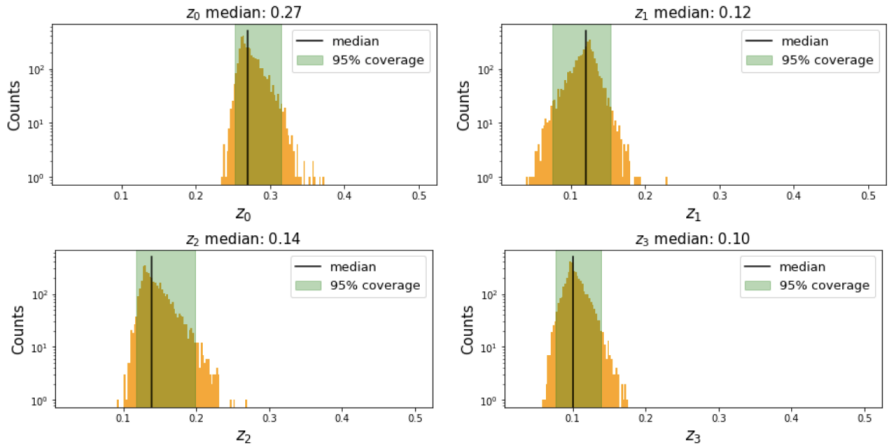

Figure 5.1: Distributions of the four z_i parameters only for traces in the training set with a peak < 0.01 A. U.. The position of the median is indicated by a black line and the corresponding value is displayed. The green bands indicate the selected 95% intervals as the latent space region for each variable z_i where the CAE places signal-free traces.

5.1 Building the criterion

Fig. 5.1 displays the distributions obtained from the encoding of waveforms with a peak < 0.01 A. U.. As noticed in the previous Chapter, in this subset of traces each of the four z_i variables assumes a value in its accumulation range. Conversely, if the four z_i latent variables of a trace do not simultaneously fall within the identified ranges, a signal is likely to be present, and the waveform can be tagged as an event. The initial step involves quantifying the accumulation values and the surrounding ranges, which serve as the basis for the selection process. The reference values of the four z_i are identified and calculated as the median of the distributions of traces with a peak less than 0.01 A. U.. The width of each range is calculated as the central interval with a 95% coverage around the median. Fig. 5.1 shows the obtained intervals, identified by the green bands.

The choice of a 95% interval is based on the hypothesis that approximately 5% of the waveforms with a peak value below 0.01 A. U. may still contain a small signal, likely embedded in the tails of the reduced distributions. Consequently, traces located in the garage region of the latent space are expected to exhibit negligible or no signal.

The **CAE-based tagging method** developed to label a trace as either a signal or a baseline can be summarized in the following steps:

1. apply the CAE to each event to obtain the associated z vector
2. check if all four values of the latent variables z_i fall within the calculated garage region
   (a) if so, the trace is marked as a noise-only event
   (b) traces that do not fall within this latent space locus have a signal instead

However, it is essential to test the validity and robustness of this method by isolating instances where it fails to correctly tag a trace. The tests aim to ensure that the chosen garage definition correctly discards all background events without misidentifying small signals. Furthermore, such tests are crucial for validating a methodology based on deep learning algorithms. The ability of the CAE to capture essential features for accurate trace reproduction has been assessed by comparing loss values on the training and test sets. It is now necessary to confirm that these variables are not only useful for encoding-decoding but also encapsulate clues about patterns in the traces that indicate the presence or absence of signals. Robustness tests of the model will determine the validity of this criterion and indirectly demonstrate the potential of the machine learning approach for studying signals where traditional methods may have limitations.

The tests done are basically two:

False-positive search : given a set of traces with only noise, estimate the fraction of events where a signal is mistakenly found

False-negative search : given a set of traces with a signal pulse, estimate the fraction of events mistakenly falling in the garage region

The following sections deal with both studies in detail, with particular attention to the specific datasets used and the results obtained.

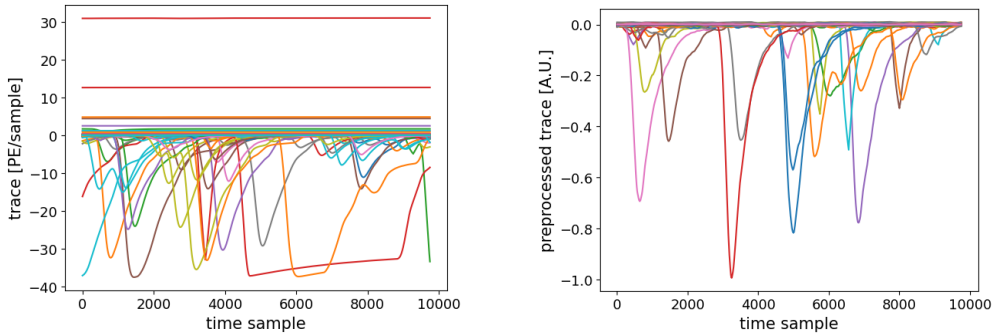

(a) Extracted dataset

(b) Dataset after pre-processing

Figure 5.4: Dataset of traces acquired with random trigger: **(a)** before pre-processing procedure; **(b)** after cuts and pre-processing steps described in the text.

5.1.1 Evaluating False Positives

An estimation of the false positives identified by the CAE-based method is necessary to assess whether the intervals determined from the observed behavior in the z_i distributions, for traces with a peak value below 0.01 A. U., effectively exclude all signal-free waveforms. In order to evaluate the efficacy of the technique in this particular instance, a dedicated dataset comprising randomly triggered events, predominantly consisting of baselines, has been employed. These events have been collected using an external trigger of 30 Hz. The acquisition window for these events is 120 µs in duration, resulting in raw traces that consist of 60000 samples. These traces are subsequently downsampled to 15000 samples through the fixed-window averaging process described in Sec. 4.2. To align the traces to the same size as the physical events, the first 5000 samples have been removed.

The initial dataset contains 10000 recorded raw traces, and it also underwent the same pre-processing steps described in Sec. 4.2. Tab. 5.1 presents the list of the various cuts performed and the events remaining at each of them. Although the events were collected to have no true signals, a few traces have a visible pulse due to accidental events recorded in the TPC, so the cutoff for peaks >-1 A. U. is applied to this data set as well. After pre-processing, the dataset consists of 9917 traces (see Fig. 5.4 (b)).

The CAE processes these traces, assigning each trace a vector z in the latent

Procedure step	# events left	% events left
Starting point	10000	100%
Dispersion first 100	9987	99.9%
Dispersion last 100	9974	99.7%
Start-end difference	9939	99.4%
Peak >-1 A. U.	**9917**	99.2%

Table 5.1: Size of the dataset of traces collected with random trigger. In the last column is reported the fraction of events survived from the original dataset. In bold is the number of waveforms for the final dataset.

space. Fig. 5.5 displays the distribution of the z_i parameters for the traces in this randomly triggered dataset, with the ranges to locate the garage overlaid. The tagging criterion is applied to each trace by assessing whether the z_i parameters fall within the garage region and, if they meet this condition, the trace is tagged as a baseline event.

As evident in Fig. 5.4 (b), 24 traces clearly exhibit an unambiguous signal, all of which are correctly identified as good events by the method. The remaining

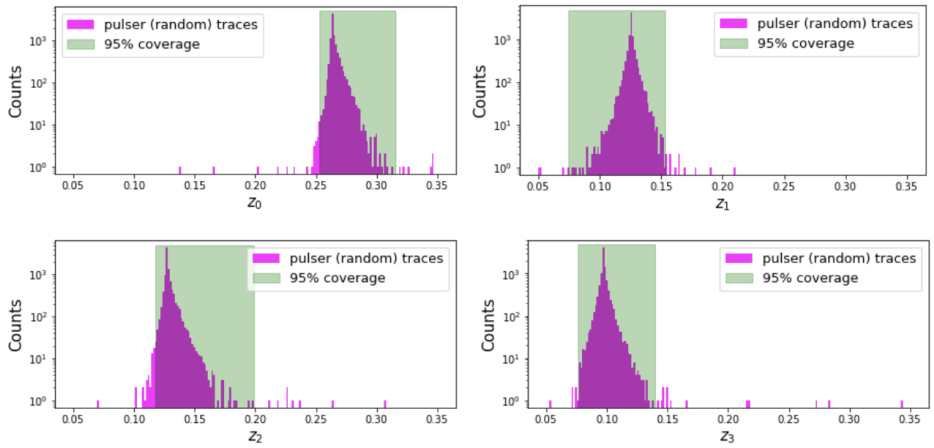

Figure 5.5: Distributions of the z_i parameters for the dataset of noise-only waveforms collected with the random trigger, with the four intervals composing the garage superimposed (in green). As mentioned, there are also traces with a visible pulse, that are encoded with at least one of the four z_i visibly outside of the given ranges, as expected.

9893 events are presumed to be true baseline-only events. Among these, the tagging criterion identifies a total of 78 out-of-garage events, that should contain a signal pulse according to the method. They represent the false positive fraction which amounts to 0.8%. This result is highly encouraging, as the CAE-based method, despite being developed using waveforms from physics runs with mainly real signals, has proven effective on a dataset composed exclusively of noise-only traces from random triggers. This finding also suggests a potential correlation among the four z-variables. For a baseline to be correctly classified, all four z_i values must lie within their respective intervals. The probability that, due to fluctuations, any one of the z_i values falls outside its interval is 0.05. Given that all four z_i values must be within their intervals, the probability of correctly identifying a baseline is $(1-0.05)^4 = 0.814$. This calculation implies an expected false positive rate of approximately 19%. However, the observed probability of correctly labeling a baseline is 99.2%, which suggests that the four variables are not orthogonal but instead exhibit some degree of correlation. This observation reinforces the effectiveness of the CAE-based method. The CAE was trained on traces where a signal was expected, even when it was sometimes indistinguishable from baseline fluctuations. When tested on a new dataset primarily composed of noise, the method demonstrated its ability to correctly recognize baselines, not merely as a result of statistical fluctuations, but as a learned capability. This indicates that the CAE-based method has genuinely learned to identify baselines through its training, rather than relying on random fluctuation in the data. The distributions of the z_i variables for both the training set, used to calculate the ranges, and the noise-only set are illustrated in Fig. 5.6.

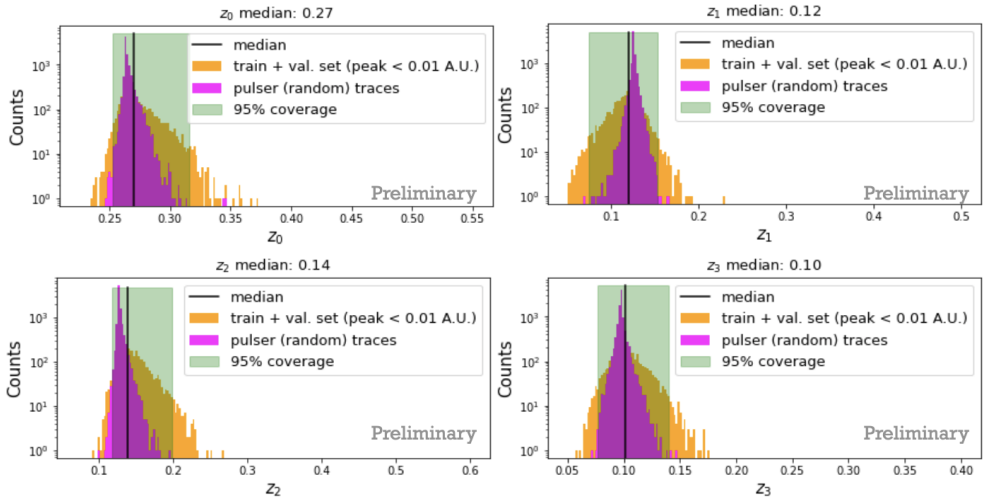

Figure 5.6: The distributions of the z_i parameters for traces with a peak < 0.01 A. U. are displayed (orange), together with the distribution of the z_i parameters for the 9893 events collected with a random trigger (magenta), where signals are not expected. As can be seen, these distributions fall within the selected range. This dataset is used to estimate the false positive of the method.

5.1.2 False Negatives Detection and Analysis on the inferences

False negatives are cases where the CAE-based method misses a positive case, that is a trace with a low signal. This results in the trace being incorrectly tagged and the potential signal being overlooked for analysis. Such a check is more easily performed on a labeled dataset, where it is possible to unambiguously verify the response on the waveform. Ideally, false negatives and tagging efficiency as a function of S2 could be studied using synthetic waveforms generated by Monte Carlo simulations with varying S2 values. However, this approach was not possible due to the lack of the necessary MC sample. The preliminary dataset presented by the ReD collaboration in [114] (see Fig. 3.37 in Sec. 3.5) is indeed a good candidate for such a test, containing a well-studied set of S2-only events from NR. However, it cannot be used for this purpose immediately, because the possibility of verifying the potential of the method developed with CAE against conventional analysis would be lost since this dataset is the result of careful selection that also occurred as a result of the analysis, as will be discussed in the following. In fact, the limitation of conventional selection is that it is less than 100% efficient for events generated by fewer than 4 e^-, making it difficult to determine whether mis-selected baselines are present among the lowest signals.

The candidate S2-only events from NR used to test the model is instead a good pool of data to be used for this purpose. Given the way the experiment is designed, this dataset is expected to consist mostly of good events. However, this dataset also included events that were mistakenly identified as signals but were actually due to baseline fluctuations.

The waveforms included in the test set were chosen according to the criteria described in Sec. 4.2:

1. event attributable to a neutron, as determined by the ToF and PSD measured by the tagger detectors;

2. the signal seen in the TPC by the SiPMs is recognised as a single scattering, that is a S2 pulse;

3. the event has a clean waveform according to the cut performed in the pre-processing procedure and the value of the peak is lower than 1 A. U.;

4. the cut on the fiducial area within the TPC is applied to exclude events that likely do not represent a true signal.

The latter cut was not previously implemented during pre-processing, as it was deemed unnecessary for pattern recognition during model training. However, it is essential for accurately identifying false negatives. By excluding events in the outermost region of the TPC, the analysis can focus on the most precise and reliable data.

Quantities obtained from the Blue level reconstruction (Subsec. 3.3.2) are associated with each waveform, including the position (x, y), derived from the SiPM that detected the most light, and the integrated S2 value. Using this information, the fiducial cut is applied to extract the desired subset. From the 1378 events in the NR test set, only those recorded by SiPMs within the fiducial region, a square located centrally in the TPC with a side length of 4 cm, are selected. In conclusion, there are a total of 872 events in the fiducial zone (Fig. 5.7) and the CAE-based tagging method is applied to them. Among these are all the *golden* events for ReD analysis, which number about 600 and are used as a benchmark of the performance of the inference made on the subset of data to which the tagging criterion is applied.

The result of this operation is displayed schematically in Fig. 5.8, which

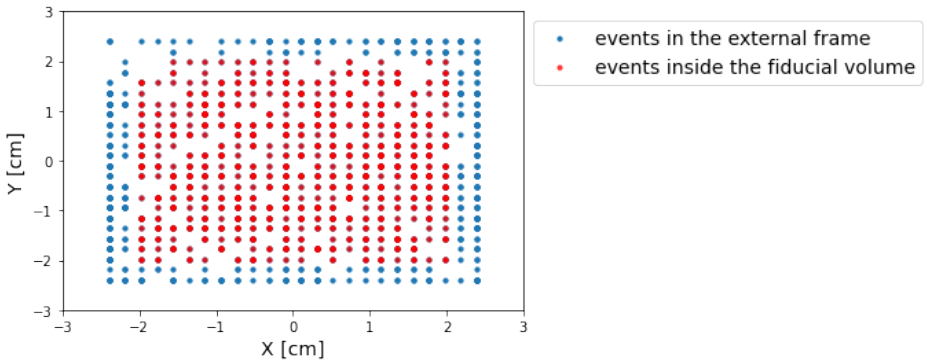

Figure 5.7: Events in the test set of candidate S2-only signals from NRs are plotted according to their reconstructed position within the TPC. In this way it is possible to discard the outermost events (in blue) and keep only the events in the most central area (in red) where good events are expected, that is, less affected by the effects of electric field non-uniformity or the possibility of not being due to a neutron entering the TPC and scattering on the argon.

shows two nested ring plots. In the outer ring, the classification of the waveforms made by the CAE-based method is clearly visible, with the events marked as signals, indicated in blue, representing 93% (813 events) of the total, while the remaining 7% (59 events), colored in orange, are the waveforms discarded because they fall within the latent space region indicated by the garages. These

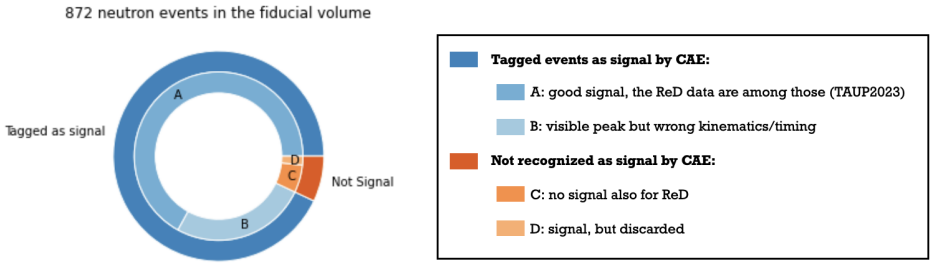

Figure 5.8: This plot schematically summarizes the result obtained by applying the tagging selection based on CAE to the reduced dataset of S2-only candidates. The outer ring simply displays the distinction, but the two classes are examined in depth to benchmark the accuracy of the criterion to evaluate the fraction of false negative events. More details in the text.

two subsets are analyzed by comparing the selection made by the CAE-based method with the cuts made by the conventional selection that led to the golden data. Those events are in the fraction of the blue events labeled with the letter A. Among the traces recognized as signals by the tagging criterion, there is a fraction, amounting to 28% (225 events) and denoted by the letter B in the graph, which consists mostly of traces that have signal pulses but do not match as NR events according to the conventional analysis cuts. The reasons why these traces are discarded are related to the unphysical timing. As mentioned in Sec. 3.5, an S2-only signal from NR is expected in a time interval that must be temporally compatible with the physics of the event. The window in which it is expected has as boundaries the arrival time of the signal from one of the two BaF_2 crystals initiating the trigger and the maximum drift time of the TPC, which is about 65 µs. Waveforms with pulses arriving before and after these two times are discarded as unphysical. Another part of these traces in B are discarded because of the calculated recoil energy, which is not in the range investigated of 1-10 keV. These cuts related to the geometry of the setup and the physics, features that could not have been learned by the model in the

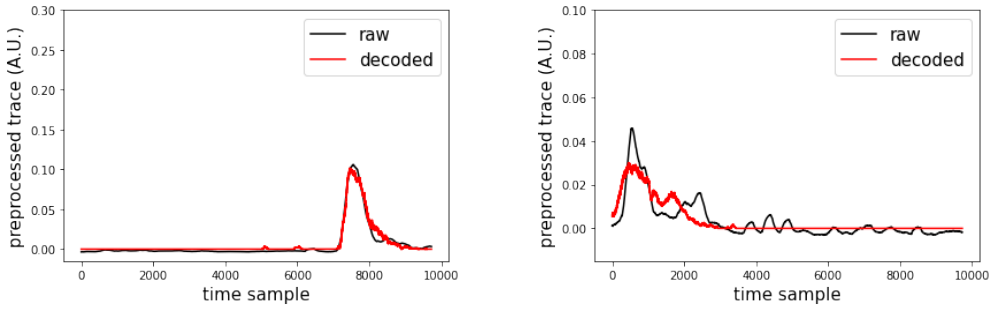

(a) (b)

Figure 5.11: Examples of raw (black) and decoded (red) waveforms having a pulse recorded within an unphysical time: **(a)** the waveform features a pulse too late if compared to the maximum drift time expected inside the TPC, while the trace in **(b)** has a signal in a time region not coherent with the start time of the BaF_2 detector that gives the trigger of the event.

unsupervised approach followed and that required *a posteriori* cleaning.

Consider the waveforms rejected by the CAE-based method, shown in dark orange in the diagram in Fig. 5.8: among these events, two distinct categories, labeled C and D, can be identified. Events in category C, comprising 78% (47 events) of the discarded traces, are also consistently excluded by conventional selection. In contrast, the events in category D (12 traces), amounting to 22% of the waveforms rejected by the CAE-based method, would have passed the conventional analysis cuts. This fraction represents the potential false negatives.

However, they, along with the detected signals in the A fraction (588 events), need further consideration in the following.

5.2 Comparison with the preliminary dataset presented by ReD

The ReD experiment has successfully collected low-energy nuclear recoil events within the recoil energy range of 1-2 keV. This achievement also serves as a benchmark for the CAE trace identification approach. To validate the selection made using the tagging criterion developed with latent space parameters, it is necessary to analyze the traces in subgroups A and D and compare them

with the preliminary dataset presented in Fig. 3.37. Of the 600 events in the golden dataset for ReD, only 12 are not confirmed by the CAE tagging method and are the events labeled as D in Fig. 5.8. On the other hand, the CAE-based method correctly identified the remaining 588 waveforms, which are categorized in fraction A in Fig. 5.8. A closer examination reveals that the S2 values recorded in the 12 unconfirmed waveforms exhibit signals of less than 80 PE. Given the estimated value of g_2, this corresponds to signals of less than approximately $4e^-$.

Fig. 5.12 provides an overview of the data in subgroups A and D, displaying the detected S2 value as a function of the measured recoil energy. Additionally, events with an S2 value below 80 PE are highlighted in red. All waveforms identified as signals by the CAE-based method are marked with a cyan "×". Notably, this selection consistently identifies all waveforms with a large (>80 PE) signal, thus correctly classifying all the blue-marked events. Its performance is less effective for low signals, whereas the conventional selection manages to recognize even these lowest signals recorded in the TPC. Two encoded-decoded traces among the red-marked ones are taken as examples and shown in Fig. 5.15: the one on the left is among those also recognized as a signal by the

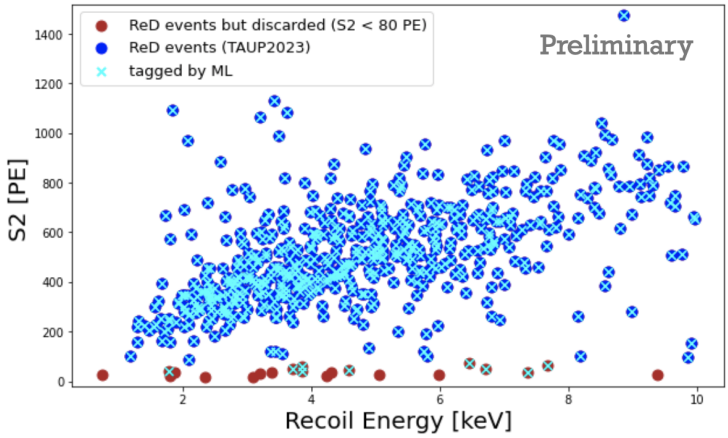

Figure 5.12: The data shown in the plot are from the preliminary dataset used by ReD to display the S2 signal in PE as a function of the recoil energy. The blue points are those preliminary presented at Conference [114], and the red ones are points discarded as probably poorly detected signals. The cyan crosses are the points marked as signals by the CAE method based on z.

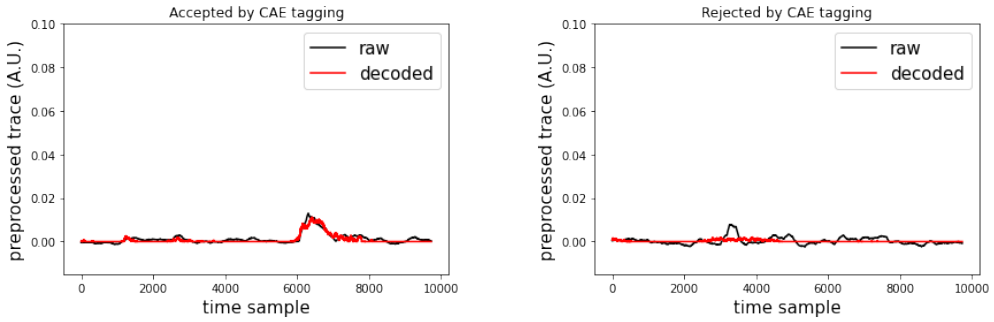

(a) (b)

Figure 5.15: Raw (black) and decoded (red) waveforms having a reconstructed S2 value below 80 PE: the waveform in **(a)** is recognized as a signal by the CAE tagging criterion, while the one shown in **(b)** falls within the garage region.

CAE-based method, while the other one on the right has been discarded.

However, the red-marked events are discarded *a posteriori* and do not appear in the preliminary dataset in the result presented in Fig. 3.37 in [114]. Indeed, as illustrated in Fig. 5.12, the S2 signals and corresponding recoil energy values of these events deviate from the trend observed in the rest of the selected dataset, suggesting they are likely the result of incorrect event selection and reconstruction in the TPC.

Although these events initially satisfied the conventional selection cuts, they were subsequently excluded. This exclusion aligns with the estimated detection efficiency of the pulse finder, which was validated exclusively through Monte Carlo simulations. Furthermore, while the CAE-based method initially appears less effective at detecting lower signals compared to the conventional approach, the exclusion of these red-marked events allows for a reassessment of the selection process, ultimately bringing its performance to a comparable level.

This finding highlights that the method developed in this thesis, by leveraging the latent space constructed by the CAE, approaches the effectiveness of the conventional method while offering distinct advantages. The key strength of this machine learning-based approach lies in its entirely data-driven nature, demonstrating its robustness and potential for reliable signal identification. Notably, the CAE autonomously extrapolates critical time series information, effectively distinguishing between signals of just a few tens of PEs and baseline

fluctuations, without requiring explicit programming. This capability underscores the power of neural networks and machine learning algorithms to adaptively capture complex patterns in data that are challenging to address with traditional methods.

5.3 Next Steps and Emerging Possibilities

The limitation of the current CAE is that it is not sensitive to signals from only a few tens of PE, but a step forward to overcome this limitation could be to study the traces recorded by individual SiPMs, rather than training the model on traces obtained by averaging waveforms from all devices. The averaged trace increases the signal-to-noise ratio, and studying individual SiPMs instead would result in forcing the investigation even under conditions where the ratio is lower. Being able to develop a tagging criterion sensitive to the single electron level (~ 20 PE) will be decisive for the future ReD+, which aims to study recoil energies of 0.4 keV.

The possibility of obtaining such sensitivity could also facilitate the study of the g_2 factor from echo signals, referred to as S3. As observed in the past in DarkSide-50 [61], delayed electroluminescence signals produced by photons of the S2 signal hitting the cathode extract one or more additional electrons that can be detected in the TPC of ReD. These electrons pass through the TPC carried by the drift field and are then extracted and accelerated into the gas. Since they are produced in the cathode, they are detected at a time interval from S2 equal to the maximum drift time. The S3 signals originate from one or two electrons, each contributing a signal of g_2 photoelectrons: the spectrum can be fitted with a sum of two Gaussian functions with central values g_2 and $2g_2$ and standard deviations σ and $\sqrt{2}\sigma$, allowing an independent measurement of the S2 gain. But on the other hand, as it is precisely because they originate from one or a few electrons, their amplitude is generally very small (< 50 PE). In the past ReD campaigns, these events were reconstructed with a relaxed threshold because of the suboptimal efficiency of the standard reconstruction algorithm in this regime [53].

These are just two examples where the application of machine learning to trace analysis could play a crucial role in characterizing the response of LAr TPCs to low-energy recoils. The data collected by ReD and by the future ReD+

would allow all these approaches to be pursued, providing a paradigm that could also be applied to future data collected with DarkSide-20k. Indeed, a much-discussed issue within the collaboration is the study of the so-called *delayed* or *spurious electrons*, an excess of events with respect to the background model observed below 4 N_{e^-} (see Fig. 5.16), whose origin might be ionization electrons trapped by impurities and released later. In the current background model, the origin of the spurious electron signals is assumed to be completely explained by the impurity mechanism in UAr, with the same level of impurities as in DarkSide-50, but further investigation is required. To study them, it is essential to be sensitive to such small signals, and this represents a promising field of application not only for autoencoders, but also for the development and combination of different architectures to obtain different views of the data.

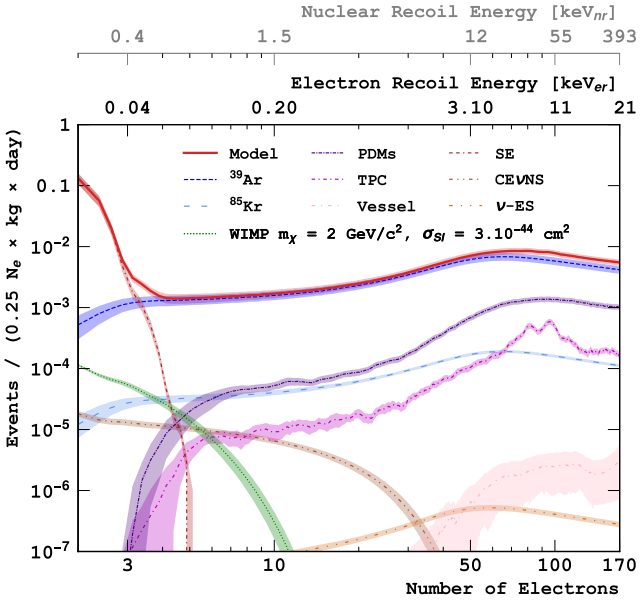

Figure 5.16: Pre-fit DS-20k N_{e^-} spectra distribution. The corresponding energy scales for ER and NR are shown at the top. The pre-fit background model (red line)is shown with its uncertainties (shaded areas). The contribution of spurious electrons (SE) dominates the background at $2 < N_{e^-} < 3$. Contributions from the other components of the background are also shown. A typical signal model is superimposed for illustration (green dotted line), assuming a 2 GeV/c^2 WIMP mass with a cross-section of 3×10^{-44} cm^2 and the QF scenario for the signal fluctuation [126].

Conclusions

The search for WIMPs continues, with the next generation of multi-ton LAr TPC experiments extending detection sensitivity to mass scales as low as a few GeV/c^2. The ReD experiment successfully collected nuclear recoils (NRs) down to the 1-2 keV range using a two-body kinematic approach. This data helps to better constrain the ionization response of argon at such low recoil energies, refining the fit parameters of the model developed by DarkSide-50. Additionally, an upgrade for the ReD experiment is in the pipeline: the ReD+ project will push these measurements even further, down to 0.4 keV, by optimizing the TPC shape and employing a deuterium-deuterium neutron generator.

In this context, the application of modern artificial intelligence techniques demonstrated the potential to extract complex features from detector data that conventional methods may overlook. This thesis focused on the analysis of waveforms recorded in the ReD TPC using deep learning, specifically a Convolutional Autoencoder (CAE). The CAE, an unsupervised neural network, has been designed to capture underlying patterns in the data and improve detection efficiency for low S2 signals from NRs, the key channel for detecting low-mass WIMPs. By compressing each waveform into a four-dimensional z parameter in a latent representation, the CAE was able to reconstruct the waveforms and reveal important latent structures. Notably, in the absence of a clear signal, the CAE consistently assigned the four z_i values to specific ranges, identifying a region in latent space, referred to as the "garage". This suggests the CAE could distinguish between signal events and baseline fluctuations in the TPC data.

A tagging criterion, referred to as the CAE-based tagging method, has been developed based on this latent space information to discriminate between signal traces and background noise. The method was validated over appropriate datasets, and the selections based on the feature extraction performed by the CAE were compared with those made by conventional techniques. While the method has not yet surpassed traditional approaches in detecting the lowest signals (tens of PEs), it nonetheless demonstrates the robustness and consistency of this unsupervised learning technique. A key strength of this study is its fully data-driven approach: no prior instructions were given to the CAE regarding the nature of the signals it would encounter. This underscores the potential of deep learning for waveform analysis and event selection in particle physics experiments.

Future work could involve using a matrix of individual waveforms seen by each SiPM during training, rather than averaged signals, to preserve single photoelectron information. This approach could extract a more informative compressed representation, enabling the detection of even smaller signals and providing spatial information by mapping the light collected by individual sensors. Once validated on ReD and ReD+ data, these data-driven techniques could be adapted for future LAr TPC experiments, enhancing signal detection and event identification in the ongoing search for WIMPs.

Acknowledgements

This Ph.D. thesis would not have been possible without the guidance, support, and encouragement of many dedicated people, and I would like to take this opportunity to thank them.

First and foremost, I would like to express my deepest gratitude to my supervisors, Dr. Pandola and Prof.ssa Puglia, for their unwavering support, invaluable guidance, and insightful feedback throughout my Ph.D. journey. Their patience and dedication have been instrumental in helping me shape and refine my working method and develop new skills. I am deeply grateful for the countless hours they spent mentoring me. I would also like to extend my gratitude to Prof. Albergo, with whom this project began, and who has continuously supported and encouraged me throughout its development.

I am also particularly grateful to Prof. Anastasi, with whom the machine learning-based method explored in this thesis was conceived and developed. Our continuous and stimulating discussions have enriched my knowledge, and the insights gained from this experience are ones I will carry forward with great value.

I owe special thanks to Dr. Gulino and Dr. Sanfilippo for their constant support, insightful advice, and genuine willingness to help. Their supportive presence and encouragement made the long hours in the lab not only manageable but enjoyable. Watching them work taught me so much about how to handle real challenges in the field. Thank you both for the patience, time, and energy you put into guiding me — it truly made a difference in my training.

I am deeply grateful to everyone in the ReD team. My heartfelt thanks go out to all the researchers and professors I have had the privilege of working with

over the years. I want to especially thank Prof. Fiorillo and Prof. Suvorov from the University of Naples for their valuable insights and the diverse perspectives they shared, Prof. Rescigno from Sapienza University of Rome for generously taking the time to discuss my work and offering invaluable advice, and Prof. Albuquerque and Prof. Moura Santos form the University of São Paulo, for the continuous encouragement and advice.

I would also like to extend my gratitude to the talented researchers of the DarkSide collaboration, with whom I had the opportunity to work and learn.

A special thank goes to my fellow students in the DarkSide project and those in the Ph.D. program in Physics here at the University of Catania, with whom I have shared this incredible experience. Your support and collaboration have been invaluable to me.

On a personal note, I would like to thank my friends and family for their unwavering belief in me. To my parents, thank you for your patience, love, and understanding. To Alessandro, your support and your love gave me the strength to persevere.

Finally, I dedicate this thesis to my sisters, Sara and Rebecca. Thank you for being my constant support.

Appendix A

The Latent Space (LS) dimension for the trained Convolutional Autoencoder (CAE) was set to 4. This dimension corresponds to the number of key features the encoder extracts from each trace, allowing the decoder to accurately reconstruct the original waveform based solely on these features. The decision to use a 4-dimensional LS was motivated by the need for a compact yet expressive feature representation, not only to facilitate interpretation and visualization but also to avoid an excessively large number of latent variables.

To validate this choice, the CAE was also trained with latent space dimensions of 2, 3, 5, and 8 for comparison. Importantly, the architecture and training dataset were kept consistent across all trials to ensure fair comparisons. In general, reducing the size of the latent space helps prevent overfitting, as fewer parameters reduce the risk of memorizing noise in the data. However, excessively small latent spaces may limit the ability of the model to encode crucial information, potentially leading to information loss.

Interestingly, all CAE trained at the different LS dimensions, the distributions for the latent parameter z_i always show the behavior with accumulation values and garages in the LS range, as it is possible to see in Fig. A.1 where the two z_i latent variable are reported, and in Fig. A.4 where the latent space variables for LS=8 are also reported.

Indeed, this behaviour seems to be characteristic of the developed autoencoder model, independently of the LS dimensionality. However, the accuracy of the encoding and decoding process substantially differs, as can be inferred by studying the losses in the different cases.

Fig. A.2 presents a comparison of training losses between models with lower and higher latent space dimensions. The model with LS = 8 consistently achieved

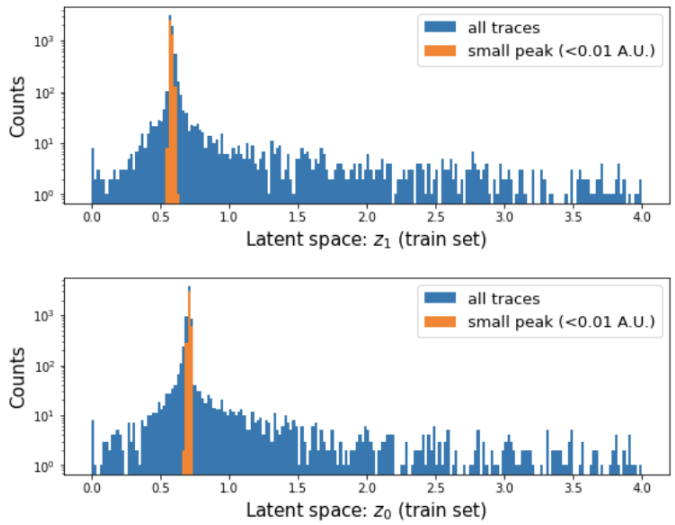

Figure A.1: Distributions of the z_i latent variables for the model trained with LS = 2. The reduced distribution for traces with small peaks (< 0.01 A.U.) are reported in orange.

lower loss values, demonstrating a superior ability to reconstruct the input waveforms compared to the CAE with LS = 2.

The losses on the test set obtained with both the models with LS equal to 2 and 8 are shown in Fig. A.3: it is possible to note how the former perform less accurately of the latter when encoding-decoding the events.

Further analysis showed that eight latent variables were excessive, as some remained near zero across many events due to over-parameterization. With an LS of 8, certain variables were frequently unused, not because of waveform characteristics, but because the CAE did not need the surplus parameters for effective reconstruction, how is possible to see form the eight distributions in Fig. A.4, where for some variables zero is largely repeated.

Fig. A.5 shows that models trained with LS = 3, 4, and 5 exhibited comparable loss values, suggesting that they all achieved a similar level of accuracy in reconstructing the waveforms (see Fig. A.6). The final choice of LS = 4 was made by balancing reconstruction fidelity with the need to avoid excessive latent parameters, ultimately confirming that an LS of 4 provided the best trade-off.

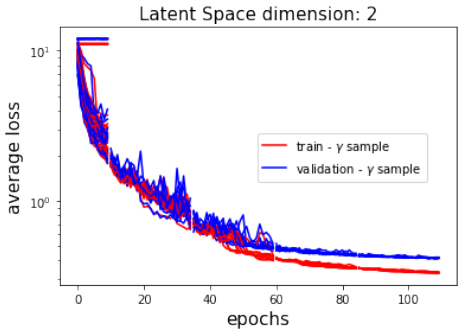

(a) LS=2

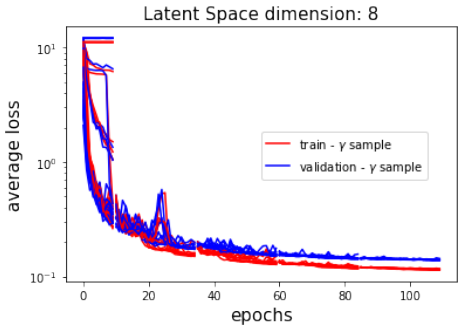

(b) LS = 8

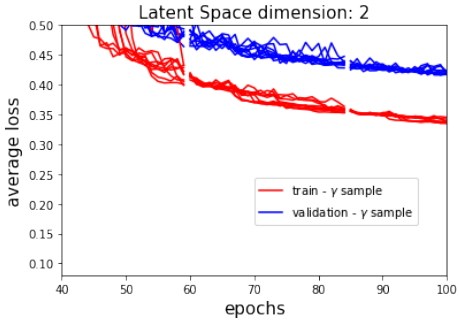

(c) LS = 2 zoom

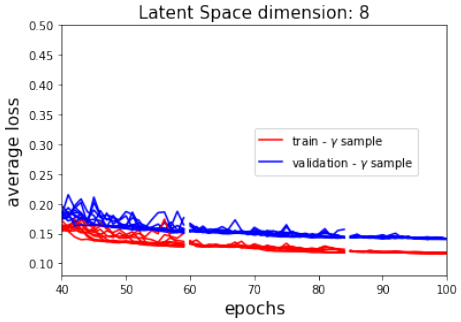

(d) LS = 8 zoom

Figure A.2: The four graphs illustrate the average loss for training and validation across epochs for two CAEs, with latent space dimensions of 2 (**(a)** and **(c)**) and 8 (**(b)** and **(d)**). The graphs in the second row provide zoomed-in views of the corresponding plots from the first row, adjusted to the same x and y scales. These zoomed views emphasize that the CAE with LS = 8 achieves a lower loss during training compared to the CAE with LS = 2 which corresponds to an higher encoding-decoding reconstruction accuracy.

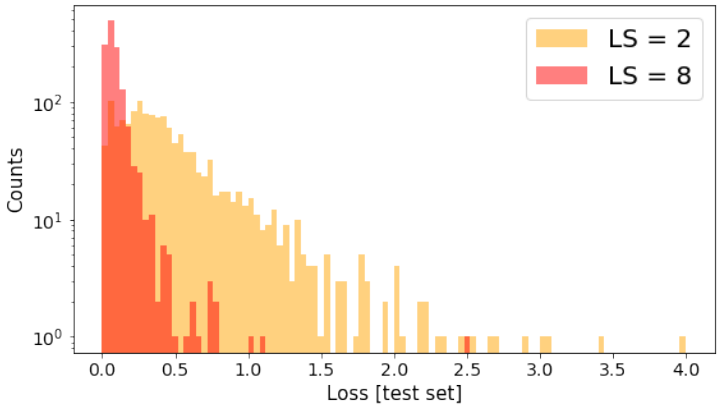

Figure A.3: Comparison of the losses obtained on the test set for the models with the smallest and largest latent space dimensions tested.

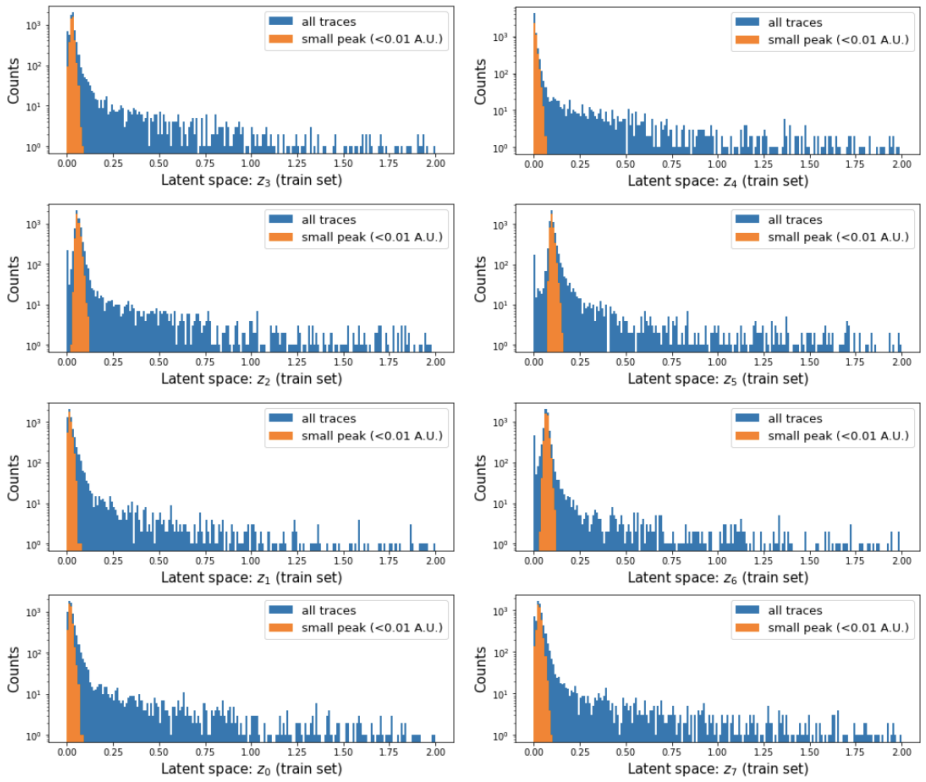

Figure A.4: Distributions of the z_i latent variables for the model trained with LS = 8. The reduced distribution for traces with small peaks (< 0.01 A.U.) are reported in orange.

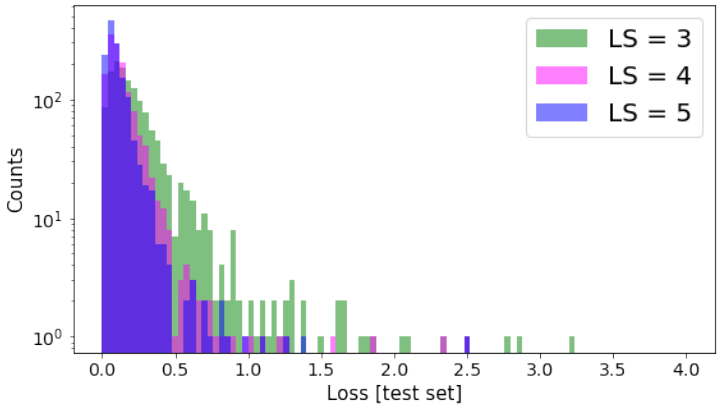

Figure A.5: Distributions of the losses on the test set obtained for models built with LS of dimensions 3, 4 and 5. It is possible to observe how for these three models the differences in the performance are small.

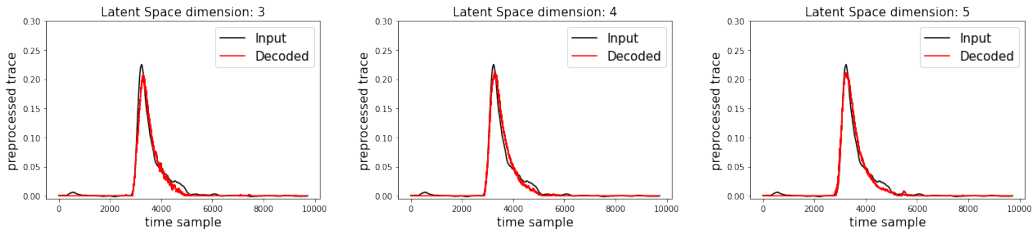

(a) LS = 3 (b) LS = 4 (c) LS = 5

Figure A.6: The three graphs depict the same event from the test set, encoded and decoded by three different CAEs with latent space dimensions of 3, 4, and 5, shown in subplots **(a)**, **(b)**, and **(c)**, respectively. The decoded traces (in red) closely match the input waveform (in black) in all cases, with minor variations.

Appendix B

An initial examination of the latent space variables z_i was conducted to assess potential correlations among them. The variables were plotted in pairs to study their relationships, as shown in the plots grouped into two main blocks, denoted as Fig. B.1 and Fig. B.2. In the scatter plots on the left, some patterns can be seen for specific subsets of events, though no clear dependency is evident. Meanwhile, the heatmaps on the right focus on the region between 0 and 1, where a distribution related to the garage projection is visible.

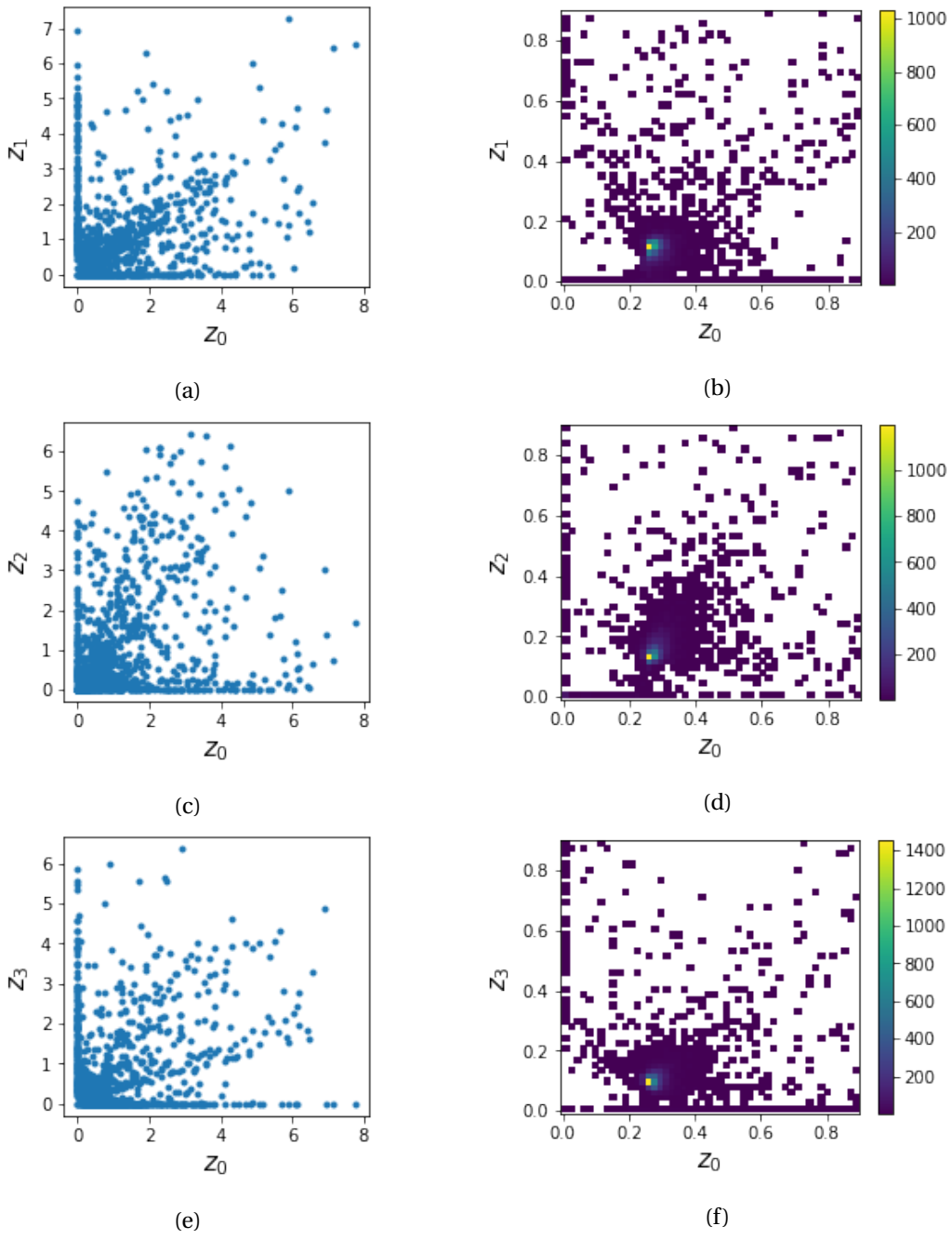

Figure B.1: On the left, the scatter plots depict the relationships between each pair of latent space variables z_i and z_j , allowing for an investigation of potential correlations. On the right, a heatmaps of the same variables are shown, zoomed into the range [0, 1], providing a density-based perspective. The heatmap reveals areas of higher concentration of data points, which are not as easily discernible in the scatter plot. As shown, none of the pairs exhibit a clear correlation. Further details are provided in the main text.

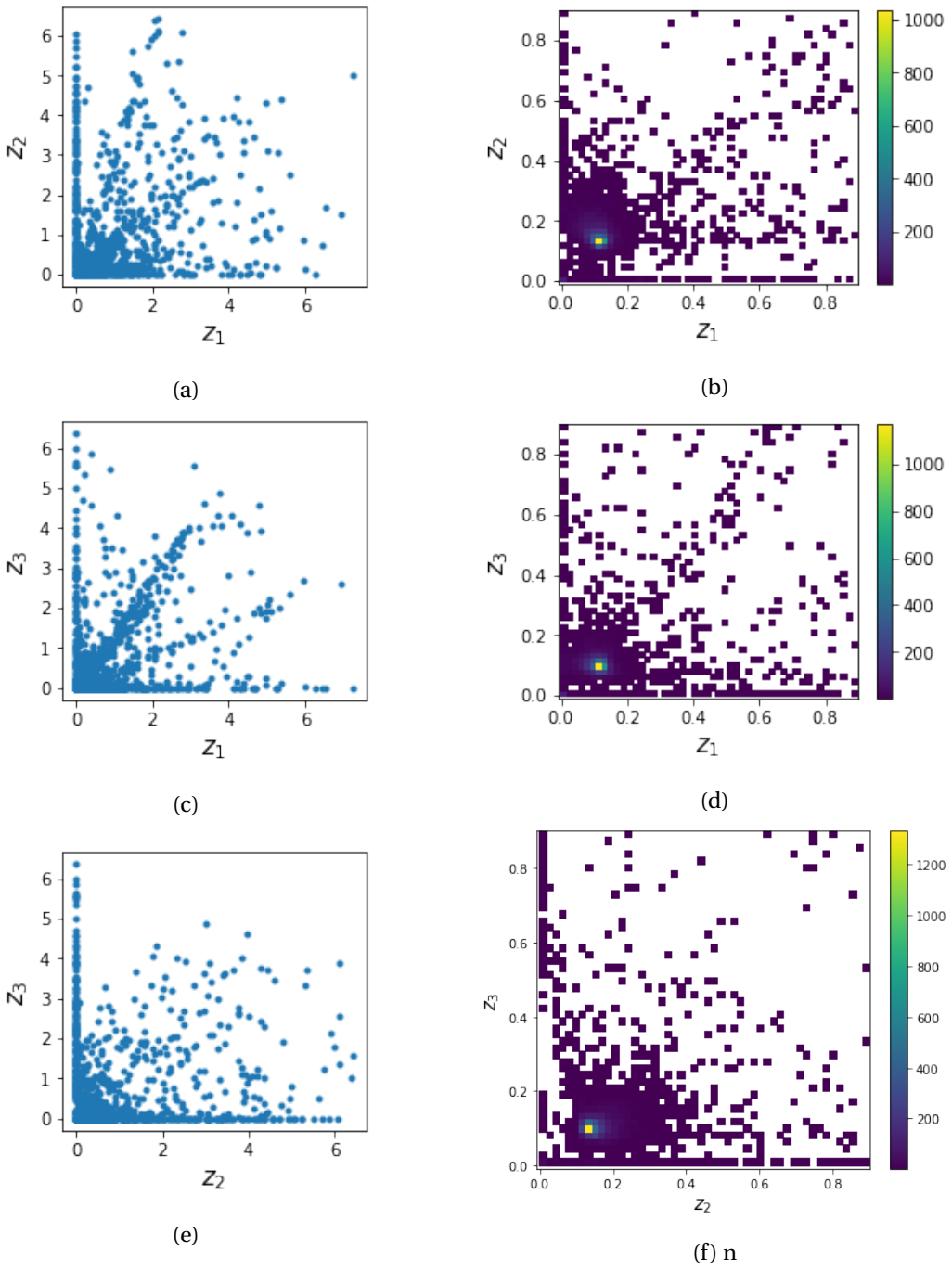

Figure B.2: On the left, the scatter plots depict the relationships between each pair of latent space variables z_i and z_j , allowing for an investigation of potential correlations. On the right, a heatmaps of the same variables are shown, zoomed into the range [0, 1], providing a density-based perspective. The heatmap reveals areas of higher concentration of data points, which are not as easily discernible in the scatter plot. As shown, none of the pairs exhibit a clear correlation. Further details are provided in the main text.

Appendix C

In Sec. 4.4, it was demonstrated that as the peak value decreases, the latent variable z_0 progressively converges towards a specific value in the latent space, with tighter accumulation around that point. This pattern is also observed for the other latent variables, and the corresponding plots illustrating these trends are provided later in this Appendix.

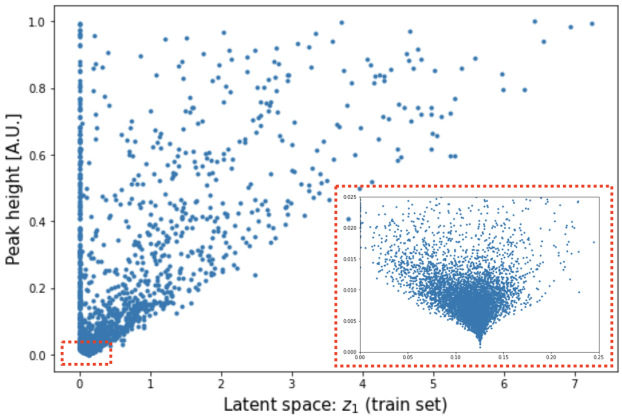

(a)

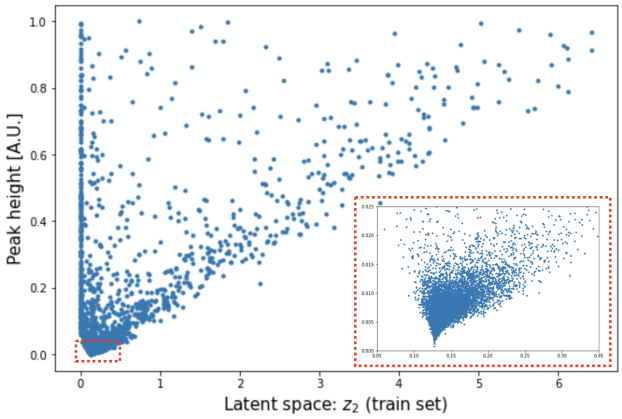

(b)

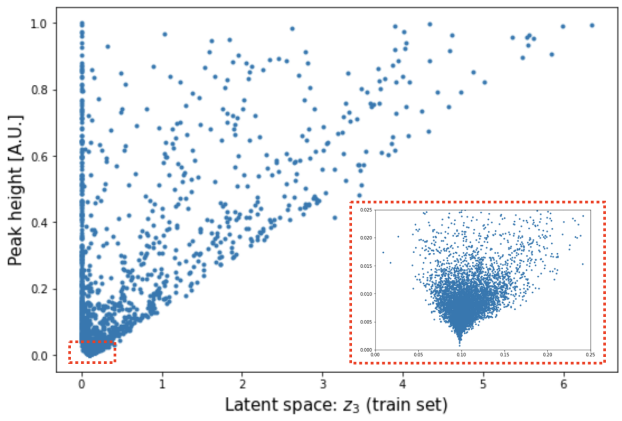

(c)

Figure C.1: Scatter plot of the latent space parameters z_1 **(a)**, z_2 **(b)** and z_3 **(c)** with respect to the height of the peak of each encoded and decoded waveforms. It is evident how the z_i values amass at around the accumulation point as the peak decreases. The inset provides a zoomed-in view of the plot for peak values lower than 0.025.

Bibliography

[1] F. Zwicky. «Die Rotverschiebung von extragalaktischen Nebeln». In: *Helv. Phys. Acta* 6 (1933), pp. 110–127.

[2] J. H. Oort. «The force exerted by the stellar system in the direction perpendicular to the galactic plane and some related problems». In: *Bull. Astron. Inst. Netherlands* 6 (1932), pp. 249–287.

[3] V. C. Rubin and W. K. Ford Jr. «ROTATION OF THE ANDROMEDA NEBULA FROM A SPECTROSCOPIC SURVEY OF EMISSION REGIONS.» In: *ApJ* 159 (Feb. 1970), p. 379.

[4] V. C. Rubin. «Dark matter in spiral galaxies». In: *Scientific American* 248 (1983), pp. 96–106.

[5] M. Spurio. *Particles and Astrophysics: A Multi-Messenger Approach*. Cham: Springer International Publishing, 2015, pp. 321–357.

[6] R. A. Sunyaev. *The thermal history of the universe and the spectrum of relic radiation*. Ed. by M. S. Longair. Vol. 63. Dordrecht: Springer Netherlands, Jan. 1974, pp. 167–173.

[7] P. A. R. Ade et al. (Plank Collaboration. «Planck 2015 results. XIII. Cosmological parameters». In: *Astron. Astrophys.* 594 (2015), A13. 63 p.

[8] R. Adam et al., (Planck Collaboration). «Planck2015 results». In: *Astron. Astrophys.* 594 (2016), A13. ISSN: 1432-0746.

[9] M. Milgrom. «A modification of the Newtonian dynamics as a possible alternative to the hidden mass hypothesis». In: *Astrophys. J.* 270 (July 1983), pp. 365–370.

[10] G. W. Angus, B. Famaey, and D. A. Buote. «X-ray Group and cluster mass profiles in MOND: Unexplained mass on the group scale». In: *Mon. Not. Roy. Astron. Soc.* 387 (2008), p. 1470.

[11] S. Bharadwaj and S. Kar. «Modeling galaxy halos using dark matter with pressure». In: *Phys. Rev. D* 68 (2 2003), p. 023516.

[12] B. P. Abbott et al., (LIGO Scientific Collaboration and Virgo Collaboration). «GW170608: Observation of a 19 Solar-mass Binary Black Hole Coalescence». In: *The Astrophysical Journal Letters* 851.2 (2017), p. L35.

[13] B. P. Abbott et al., (LIGO Scientific Collaboration and Virgo Collaboration). «GW170817: Observation of Gravitational Waves from a Binary Neutron Star Inspiral». In: *Phys. Rev. Lett.* 119 (16 2017), p. 161101.

[14] C. Alcock et al. «The MACHO Project: Microlensing Results from 5.7 Years of Large Magellanic Cloud Observations». In: *The Astrophysical Journal* 542.1 (2000), p. 281.

[15] J. García-Bellido. «Massive Primordial Black Holes as Dark Matter and their detection with Gravitational Waves». In: *Journal of Physics: Conference Series* 840.1 (2017), p. 012032.

[16] G. Bertone and Tim Tait M. P. «A new era in the search for dark matter». In: *Nature* 562.7725 (2018), pp. 51–56.

[17] X. Chen, S. Hannestad, and R. J. Scherrer. «Cosmic microwave background and large scale structure limits on the interaction between dark matter and baryons». In: *Phys. Rev. D* 65 (12 2002), p. 123515.

[18] G. Blumenthal et al. «Formation of Galaxies and Large-Scale Structure with Cold Dark Matter». In: *Nature* 313 (Jan. 1985).

[19] M. Safarzadeh and D. N. Spergel. «Ultra-light Dark Matter is Incompatible with the Milky Way's Dwarf Satellites». In: (June 2019). arXiv: 1906.11848.

[20] K. N. Abazajian et al. In: *Light Sterile Neutrinos: A White Paper* (Apr. 2012).

[21] G. G. Raffelt. «AXIONS IN ASTROPHYSICS AND COSMOLOGY». In: *arXiv: High Energy Physics - Phenomenology* (1995), pp. 159–168.

[22] R. D. Peccei and Helen R. Quinn. «Constraints imposed by CP conservation in the presence of pseudoparticles». In: *Phys. Rev. D* 16 (6 1977), pp. 1791–1797.

[23] M. Tanabashi et al. «Review of Particle Physics». In: *Phys. Rev. D* 98 (3 2018), p. 030001.

[24] N. Aghanim et al. «Plank 2018 Results». In: *A&A* 641 (2020), p. 56.

[25] H. Baer et al. «Dark matter production in the early Universe: beyond the thermal WIMP paradigm». In: *Phys. Rept.* 555 (2015), pp. 1–60.

[26] J. L. Feng and J. Kumar. «Dark-Matter Particles without Weak-Scale Masses or Weak Interactions». In: *Phys. Rev. Lett.* 101 (23 2008), p. 231301.

[27] S. Profumo. «Astrophysical Probes of Dark Matter». In: *Theoretical Advanced Study Institute in Elementary Particle Physics: Searching for New Physics at Small and Large Scales*. Colorado 4-29 June: TASI 2012, 2012, pp. 143–189.

[28] R. Bernabei et al. «Dark Matter with DAMA/LIBRA and its perspectives». In: *Journal of Physics: Conference Series* 2586.1 (2023), p. 012096.

[29] G. Bertone. *Particle dark matter: observations, models and searches*. UK: Cambridge University Press, 2010.

[30] D. Perez Adan (ATLAS and CMS cCollaborations). «Dark Matter searches at CMS and ATLAS». In: *56th Rencontres de Moriond on Electroweak Interactions and Unified Theories* (Jan. 2023).

[31] L. Pagani. «Direct dark matter detection with the DarkSide-50 experiment». PhD thesis. Genoa U., 2017. DOI: 10.2172/1354864.

[32] J. D. Lewin and P. F. Smith. «Review of mathematics, numerical factors, and corrections for dark matter experiments based on elastic nuclear recoil». In: *Astropart. Phys.* 6 (1996), pp. 87–112.

[33] L. Baudis. «WIMP Dark Matter Direct-Detection Searches in Noble Gases». In: *Phys. Dark Univ.* 4 (2014). Ed. by Frank Avignone and Wick Haxton, pp. 50–59.

[34] B. Bottino. «Dark Matter search with liquid Argon in DarkSide: results with scientific and technological prototypes». PhD thesis. University of Genova, 2019.

[35] D. S. Akerib et al. *Snowmass2021 Cosmic Frontier Dark Matter Direct Detection to the Neutrino Fog*. 2022. arXiv: 2203.08084 [hep-ex].

[36] M. Mancuso et al. (CRESST Collaboration). «Searches for Light Dark Matter with the CRESST-III Experiment». In: *J. Low Temp. Phys.* 199.1-2 (2020), pp. 547–555.

[37] A. H. Abdelhameed et al. (CRESST Collaboration). «First results from the CRESST-III low-mass dark matter program». In: *Phys. Rev. D* 100 (2019), p. 102002.

[38] R. Agnese et al. (SuperCDMS Collaboration). «Demonstration of surface electron rejection with interleaved germanium detectors for dark matter searches». In: *Appl. Phys. Lett.* 103.16 (2013), p. 164105.

[39] R. Agnese et al. (SuperCDMS Collaboration). «Search for low-mass dark matter with CDMSlite using a profile likelihood fit». In: *Phys. Rev. D* 99 (2019), p. 062001.

[40] R. Agnese et al. (SuperCDMS Collaboration). «Search for low-mass weakly interacting massive particles with Super-CDMS». In: *Phys. Rev. Lett.* 112 (2014), p. 241302.

[41] R. Agnese et al. (SuperCDMS Collaboration). «Results from the super cryogenic dark matter search experiment at Soudan». In: *Phys. Rev. Lett.* 120 (2018), p. 061802.

[42] R. K. Romani et al. «Thermal detection of single e–h pairs in a biased silicon crystal detector». In: *Appl. Phys. Lett.* 112 (2018), p. 043501.

[43] E. Aprile et al. (XENON Collaboration). «The XENON1T dark matter experiment». In: *The European Physical Journal C* 77.12 (2017). ISSN: 1434-6052.

[44] E. Aprile et al. (XENON Collaboration), XENON Collaboration. «First Dark Matter Search with Nuclear Recoils from the XENONnT Experiment». In: *Phys. Rev. Lett.* 131.4 (2023), p. 041003.

[45] The LUX-ZEPLIN (LZ) Collaboration. «The LUX-ZEPLIN (LZ) experiment». In: *Nuclear Instruments and Methods in Physics Research Section A: Accelerators, Spectrometers, Detectors and Associated Equipment* 953 (2020), p. 163047.

[46] R. Ajaj et al. (DEAP Collaboration). «Search for dark matter with a 231-day exposure of liquid argon using DEAP-3600 at SNOLAB». In: *Phys. Rev. D* 100.2 (2019), p. 022004.

[47] P. Agnes et al. (The DarkSide Collaboration). «The veto system of the DarkSide-50 experiment». In: *JINST* 11.03 (2016), P03016.

[48] P. Agnes et al. (The DarkSide Collaboration). «DarkSide-50 532-day dark matter search with low-radioactivity argon». In: *Phys. Rev. D* 98 (2018), p. 102006.

[49] J. Angle et al. (XENON10 Collaboration). «Search for Light Dark Matter in XENON10 Data». In: *Phys. Rev. Lett.* 107 (5 2011), p. 051301.

[50] P. Agnes et al. (The DarkSide Collaboration). «Search for low-mass dark matter WIMPs with 12 ton-day exposure of DarkSide-50». In: *Phys. Rev. D* 107 (2023), p. 063001.

[51] A. Hitachi et al. «Effect of ionization density on the time dependence of luminescence from liquid argon and xenon». In: *Phys. Rev. B* 27 (9 1983), pp. 5279–5285.

[52] E. Aprile et al. «Simultaneous Measurement of Ionization and Scintillation from Nuclear Recoils in Liquid Xenon for a Dark Matter Experiment». In: *Phys. Rev. Lett.* 97 (8 2006), p. 081302.

[53] P. Agnes et al. «Performance of the ReD TPC, a novel double-phase LAr detector with Silicon Photomultiplier Readout». In: *Eur. Phys. J. C* 81 (2021), p. 1014.

[54] J. Lindhard and other. «Integralequations governing radiation effects. (notes on atomic collisions, iii)». In: *Kgl. Danske Videnskab., Selskab. Mat. Fys. Medd.* 33.10 (Jan. 1963).

[55] J. Lindhard. «Onthepropertiesof a gas of charged particles». In: *Dan.Vid. Sellsk Mat.-Fys. Medd.* 28.8 (1954).

[56] R.L. Platzman. «Total ionization in gases by high-energy particles: An appraisal of our understanding». In: *The International Journal of Applied Radiation and Isotopes* 10.2 (1961), pp. 116–127.

[57] T. Doke et al. «Absolute Scintillation Yields in Liquid Argon and Xenon for Various Particles». In: *Jap. J. Appl. Phys.* 41 (2002), pp. 1538–1545.

[58] A. Hitachi et al. «Effect of ionization density on the time dependence of luminescence from liquid argon and xenon». In: *Phys. Rev.* 5 27 (1983), p. 5279.

[59] V. Chepel and H. Araújo. «Liquid noble gas detectors for low energy particle physics». In: *Journal of Instrumentation* 8.04 (2013), R04001.

[60] E. Shibamura et al. «Ratio of diffusion coefficient to mobility for electrons in liquid argon». In: *Phys. Rev. A* (1979).

[61] P. Agnes et al. (The DarkSide Collaboration). «Results from the first use of low radioactivity argon in a dark matter search». In: *Phys. Rev. D* 93 (2016), 081101(R).

[62] C.E. Aalseth et al. (The DarkSide Collaboration). «DarkSide-20k: A 20 Tonne Two-Phase LAr TPC for Direct Dark Matter Detection at LNGS». In: *Eur. Phys. J. Plus* 133 (2018), p. 131.

[63] F. Acerbi et al. (The DarkSide Collaboration). *DarkSide-20k sensitivity to light dark matter particles*. 2024. arXiv: 2407.05813 [hep-ex]. URL: https://arxiv.org/abs/2407.05813.

[64] P. Agnes et al. (The DarkSide Collaboration). «Simulation of argon response and light detection in the DarkSide-50 dual phase TPC». In: *JINST* 12 (2017), P10015.

[65] P. Agnes et al. (The DarkSide Collaboration). «First results from the DarkSide-50 dark matter experiment at Laboratori Nazionali del Gran Sasso». In: *Phys. Lett. B* 743 (2015), pp. 456–466.

[66] J. Xu et al. «A study of the trace 39Ar content in argon from deep underground sources». In: *Astroparticle Physics* 66 (2015), pp. 53–60. ISSN: 0927-6505.

[67] P. Agnes et al. (The DarkSide Collaboration). «Separating ^{39}Ar from ^{40}Ar by cryogenic distillation with Aria for dark-matter searches». In: *Eur. Phys. J. C* 81.359 (2021).

[68] E. Aaron et al. (The DarkSide Collaboration). «Measurement of isotopic separation of argon with the prototype of the cryogenic distillation plant Aria for dark matter searches». In: *Eur. Phys. J. C* 83.453 (2023).

[69] C.E. Aalseth et al. «Design and construction of a new detector to measure ultra-low radioactive-isotope contamination of argon». In: *JINST* 15 (2020), P02024.

[70] B. Abiet al. (DUNE Collaboration). «Deep Underground Neutrino Experiment (DUNE), Far Detector Technical Design Report, Volume I Introduction to DUNE». In: *JINST* 15.08 (2020), T08008.

[71] P. Agnes et al. (The DarkSide Collaboration). «Sensitivity of future liquid argon dark matter search experiments to core-collapse supernova neutrinos». In: *JCAP* 03 (2021), p. 043.

[72] E. Aprile et al. (XENON Collaboration). «Projected WIMP sensitivity of the XENONnT dark matter experiment». In: *JCAP* 11 (2020), p. 031.

[73] Andrea Zani. «The DarkSide-20k experiment». In: (2024). arXiv: 2402.07566 [physics.ins-det]. URL: https://arxiv.org/abs/2402.07566.

[74] P. Agnes et al. (The DarkSide Collaboration). «Calibration of the liquid argon ionization response to low energy electronic and nuclear recoils with DarkSide-50». In: *Phys. Rev. D* 104 (8 2021), p. 082005.

[75] J. Thomas and D. A. Imel. «Recombination of electron-ion pairs in liquid argon and liquid xenon». In: *Phys. Rev. A* 36 (2 1987), pp. 614–616.

[76] P. Sorensen and C. E. Dahl. «Nuclear recoil energy scale in liquid xenon with application to the direct detection of dark matter». In: *Phys. Rev. D* 83 (2011), p. 063501.

[77] T. Doke et al. «Let dependence of scintillation yields in liquid argon». In: *Nuclear Instruments and Methods in Physics Research Section A: Accelerators, Spectrometers, Detectors and Associated Equipment* 269.1 (1988), pp. 291–296.

[78] P. Agnes et al. (The DarkSide Collaboration). «Simulation of argon response and light detection in the DarkSide-50 dual phase TPC». In: *JINST* 12.10 (2017), P10015.

[79] P. Agnes et al. (The DarkSide Collaboration). «Low-Mass Dark Matter Search with the DarkSide-50 Experiment». In: *Phys. Rev. Lett.* 121 (8 2018), p. 081307.

[80] F. Bezrukov, F. Kahlhoefer, and M. Lindner. «Interplay between scintillation and ionization in liquid xenon Dark Matter searches». In: *Astropart. Phys.* 35 (2011), pp. 119–127.

[81] J. P. Biersack and J. F. Ziegler. «The Stopping and Range of Ions in Solids». In: *Ion Implantation Techniques*. Ed. by Heiner Ryssel and Hans Glawischnig. Berlin, Heidelberg: Springer Berlin Heidelberg, 1982, pp. 122–156.

[82] P. Agnes et al. (The DarkSide Collaboration). «CALIS: A CALibration Insertion System for the DarkSide-50 dark matter search experiment». In: *JINST* 12.12 (2017), T12004.

[83] H. Cao et al. (SCENE Collaboration). «Measurement of Scintillation and Ionization Yield and Scintillation Pulse Shape from Nuclear Recoils in Liquid Argon». In: *Phys. Rev. D* 91 (2015), p. 092007.

[84] P. Agnes et al. «Measurement of the liquid argon energy response to nuclear and electronic recoils». In: *Phys. Rev. D* 97.11 (2018), p. 112005.

[85] T. H. Joshi et al. «First measurement of the ionization yield of nuclear recoils in liquid argon». In: *Phys. Rev. Lett.* 112 (2014), p. 171303.

[86] Gert Moliere. «Theorie der Streuung schneller geladener Teilchen I. Einzelstreuung am abgeschirmten Coulomb-Feld». In: *Zeitschrift für Naturforschung A* 2.3 (1947), pp. 133 –145.

[87] W. Lenz. «Über die Anwendbarkeit der statistischen Methode auf Ionengitter». In: *Zeitschrift für Physik* 77.11 (Nov. 1932), pp. 713–721.

[88] H. Jensen. «Die Ladungsverteilung in Ionen und die Gitterkonstante des Rubidiumbromids nach der statistischen Methode». German. In: *Zeitschrift für Physik* 77.11-12 (1932), pp. 722–745.

[89] E. Aprile et al. (XENON Collaboration). «Search for Light Dark Matter Interactions Enhanced by the Migdal Effect or Bremsstrahlung in XENON1T». In: *Phys. Rev. Lett.* 123 (24 2019), p. 241803.

[90] M. Traina et al. (DAMIC Collaboration). «Results on low-mass weakly interacting massive particles from a 11 kg d target exposure of DAMIC at SNOLAB». In: *PoS* ICRC2021 (2021), p. 539.

[91] C. Amole et al. (PICO Collaboration). «Dark Matter Search Results from the PICO−60 C_3F_8 Bubble Chamber». In: *Phys. Rev. Lett.* 118 (25 2017), p. 251301.

[92] R. Agnese et al. (SuperCDMS Collaboration). «Low-mass dark matter search with CDMSlite». In: *Phys. Rev. D* 97 (2 2018), p. 022002.

[93] R. Agnese et al. (SuperCDMS Collaboration). «Search for Low-Mass Weakly Interacting Massive Particles Using Voltage-Assisted Calorimetric Ionization Detection in the SuperCDMS Experiment». In: *Phys. Rev. Lett.* 112 (2014), p. 041302.

[94] E. Behnke et al. «Final results of the PICASSO dark matter search experiment». In: *Astroparticle Physics* 90 (2017), pp. 85–92.

[95] C. E. Aalseth et al. (CoGeNT Collaboration). «Results from a Search for Light-Mass Dark Matter with a p-Type Point Contact Germanium Detector». In: *Phys. Rev. Lett.* 106 (13 2011), p. 131301.

[96] R. Bernabei et al. «Final model independent result of DAMA/LIBRA-phase1». In: *Eur. Phys. J. C* 73 (2013), p. 2648.

[97] W. Ma et al. (PandaX Collaboration). «Search for Solar B8 Neutrinos in the PandaX-4T Experiment Using Neutrino-Nucleus Coherent Scattering». In: *Phys. Rev. Lett.* 130.2 (2023), p. 021802.

[98] G. Angloher et al. «Results from 730 kg daysof the CRESST-II Dark Matter search». In: *Eur. Phys. J. C* 72 (2012), p. 1971.

[99] E. Aprile et al. (XENON Collaboration). «Search for Coherent Elastic Scattering of Solar ^{8}B Neutrinos in the XENON1T Dark Matter Experiment». In: *Phys. Rev. Lett.* 126 (2021), p. 091301.

[100] D. S. Akerib et al. (LUX Collaboration). «Improving sensitivity to low-mass dark matter in LUX using a novel electrode background mitigation technique». In: *Phys. Rev. D* 104 (2021), p. 012011.

[101] F. Ruppin et al. «Complementarity of dark matter detectors in light of the neutrino background». In: *Physical Review D* 90.8 (Oct. 2014).

[102] J. F. Dicello, W. Gross, and U. Kraljevic. «Radiation Quality of Californium-252». In: *Phys. Med. Biol.* 17.3 (1972), p. 345.

[103] P. A. Balo, J. B. Knauer, and R. C. Martin. «Production, Distribution, and Applications of Californium-252 Neutron Sources». In: *IRRMA '99: 4th Topical Meeting on Industrial Radiation*. Raleigh, NC, Oct. 1999.

[104] A. Mandarano. «New generation, SiPM-based, Liquid Argon TPCs from the kg to the multi-ton scale.» PhD thesis. Gran Sasso Science Institute, 2017.

[105] S. Sanfilippo. «Dark Matter direct detection with the DarkSide project ReD: an experiment to probe the recoil directionality in Liquid Argon». PhD thesis. Università degli Studi Roma Tre, Dipartimento di Matematica e Fisica E. Amaldi, 2020.

[106] E.V. Ryabeva et al. «Calibration of EJ-276 plastic scintillator for neutron–gamma pulse shape discrimination experiments». In: *Nuclear Instruments and Methods in Physics Research Section A: Accelerators, Spectrometers, Detectors and Associated Equipment* 1010 (2021), p. 165495.

[107] Eljen Technology. *EJ-276 datasheet*. 2020. URL: https://eljentechnology.com/products/plastic-scintillators/ej-276.

[108] S. Vinogradov et al. «Probability distribution and noise factor of solid state photomultiplier signals with cross-talk and afterpulsing». In: *2009 IEEE Nuclear Science Symposium Conference Record (NSS/MIC)*. 2009, pp. 1496–1500.

[109] S. Vinogradov. «Analytical models of probability distribution and excess noise factor of solid state photomultiplier signals with crosstalk». In: *Nuclear Instruments and Methods in Physics Research Section A: Accelerators, Spectrometers, Detectors and Associated Equipment* 695 (2012), pp. 247–251.

[110] P. Agnes et al. (The DarkSide Collaboration). «Constraints on directionality effect of nuclear recoils in a liquid argon time projection chamber». In: *Eur. Phys. J. C* 84 (2024), pp. 1–24.

[111] L. W. Kastens et al. «Calibration of a Liquid Xenon Detector with Kr-83m». In: *Phys. Rev. C* 80 (2009), p. 045809.

[112] G. Chiodini. «The PADME experiment for dark mediator searches at the Frascati BTF». In: *Journal of Instrumentation* 12.02 (2017), pp. C02037–C02037.

[113] National Instruments. *LabView*. 2017. URL: https://www.ni.com/en/shop/labview.html.

[114] I. Ahmad et al. «Characterization of low-energy argon recoils with the ReD experiment». In: *Proceedings of XVIII International Conference on Topics in Astroparticle and Underground Physics — PoS(TAUP2023)*. Vol. 441. 2024, p. 052. DOI: 10.22323/1.441.0052.

[115] Arthur L Samuel. «Some studies in machine learning using the game of checkers». In: *IBM Journal of research and development* 3.3 (1959), pp. 210–229.

[116] Pierre Baldi. «Autoencoders, Unsupervised Learning, and Deep Architectures». In: *Proceedings of ICML Workshop on Unsupervised and Transfer Learning*. Ed. by I. Guyon et al. Vol. 27. Proceedings of Machine Learning Research. Bellevue, Washington, USA: PMLR, 2012, pp. 37–49.

[117] Hongyu Shen et al. «Denoising Gravitational Waves using Deep Learning with Recurrent Denoising Autoencoders». In: (Nov. 2017). arXiv: 1711.09919 [gr-qc].

[118] F. Morawski et al. «Anomaly detection in gravitational waves data using convolutional autoencoders». In: *Machine Learning: Science and Technology* 2.4 (2021), p. 045014.

[119] Guido Van Rossum and Fred L. Drake. *Python 3 Reference Manual*. Scotts Valley, CA: CreateSpace, 2009.

[120] F. Chollet et al. *Keras*. 2015. URL: https://github.com/fchollet/keras.

[121] A. Gulli and S. Pal. *Deep learning with Keras*. Packt Publishing Ltd, 2017.

[122] M. Abadi et al. «TensorFlow: Large-Scale Machine Learning on Heterogeneous Distributed Systems». In: (Mar. 2016). arXiv: 1603.04467 [cs.DC]. URL: https://www.tensorflow.org.

[123] INFN. *INFN Cloud, resources for researchers*. 2021. URL: https://www.cloud.infn.it.

[124] Ian Goodfellow, Yoshua Bengio, and Aaron Courville. *Deep Learning*. http://www.deeplearningbook.org. MIT Press, 2016.

[125] Diederik P. Kingma and Jimmy Ba. *Adam: A Method for Stochastic Optimization*. 2017. arXiv: 1412.6980 [cs.LG]. URL: https://arxiv.org/abs/1412.6980.

[126] F. Acerbi et al. (The DarkSide Collaboration). *DarkSide-20k sensitivity to light dark matter particles*. 2024. arXiv: 2407.05813 [hep-ex]. URL: https://arxiv.org/abs/2407.05813.

[127] F. Zwicky. «On the Masses of Nebulae and of Clusters of Nebulae». In: *Astrophys. J.* 86 (1937), pp. 217–246.

[128] N. E. Mavromatos, M. Sakellariadou, and M. F. Yusaf. «Can the relativistic field theory version of modified Newtonian dynamics avoid dark matter on galactic scales?» In: *Phys. Rev. D* 79 (8 2009), p. 081301.

[129] R. Agnese et al. (SuperCDMS Collaboration). «First dark matter constraints from a SuperCDMS single-charge sensitive detector». In: *Phys. Rev. Lett.* 121 (2018), p. 051301.

[130] E. Aprile et al. (XENON Collaboration), XENONCollaboration. «Dark Matter Search Results from a One Ton-Year Exposure of XENON1T». In: *Phys. Rev. Lett.* 121.11 (2018), p. 111302.

[131] P. Agnes et al. (The DarkSide Collaboration). «Sensitivity projections for a dual-phase argon TPC optimized for light dark matter searches through the ionization channel». In: *Phys. Rev. D* 107.11 (2023), p. 112006.

[132] D. D'Angelo. «DarkSide-50 Results from first Argon run». In: *Oral contribution to 20th Particle & Nuclei International Conference, Hamburg, Germany*. 2014.

[133] M. Caravati. «The ReD experiment in DarkSide's Program: nuclear recoils for Dark Matter studies». PhD thesis. Università degli studi di Cagliari, 2019.

[134] C. M. Bishop. *Pattern Recognition and Machine Learning*. Springer, 2006.